BULGARIAN CHEMICAL COMMUNICATIONS

2026 Volume 58 / Special Issue A

Selected papers from the International Conference “Science-Industry-Society Nexus for Sustainable Regions”, organized by the Burgas State University “Prof. Dr. Assen Zlatarov”and the Thracian University-Odrin, Turkey, June 12 - 14, 2025, Burgas, Bulgaria

Journal of the Chemical Institutes
of the Bulgarian Academy of Sciences
and of the Union of Chemists in Bulgaria

PREFACE

The present special issue of Bulgarian Chemical Communications (BCC) brings together a selection of peer-reviewed papers presented at the International Conference "Science–Industry–Society Nexus for Sustainable Regions" (SISNEXUS 2025), under the thematic focus "Chemistry, Chemical Technologies, Biotechnologies, and Environmental Challenges – Sustainable Materials, Green Chemistry and Solutions for Environmental Protection."

The conference was organized by Burgas State University "Prof. D-r Assen Zlatarov" in partnership with Trakya University in Edirne, Turkey. It aimed to bring together researchers, experts, and professionals from diverse scientific and applied fields to foster interdisciplinary dialogue and promote innovative approaches to the sustainable development of regions.

This special issue reflects the scientific contributions presented during the conference and highlights current advances, emerging trends, and practical solutions addressing pressing environmental and technological challenges.

The SISNEXUS 2025 was held from June 12 to 14, 2025, in Burgas, at the College of Tourism of Burgas State University "Prof. D-r Asen Zlatarov" (https://sisnexus.uniburgas.bg/index.php).

SCIENCE-INDUSTRY-SOCIETY
FOR SUSTAINABLE REGIONS

SISNEXUS

Conference, organized by
Burgas State University "Prof. Dr. Assen Zlatarov", REPUBLIC OF BULGARIA
and
Trakya University – Edirne, REPUBLIC OF TURKEY

Overall, the collected papers demonstrate the growing importance of interdisciplinary research and collaboration in addressing complex environmental and technological issues, and they underline the key role of science and innovation in advancing sustainable regional development.

Guest Editor
Svetlana Genieva

Bulgarian Chemical Communications, Volume 58, Special Issue A (pp. 05-09) 2026 DOI: 10.34049/bcc.58.A.SN-01

Relation between terrestrial background radiation and air dose rate

S. Nedkova*, P. V. Atanasova

Department of Materials Science, Burgas State University „Prof. Dr. Assen Zlatarov“, 1 Prof. Y. Yakimov Str., Burgas 8010, Bulgaria

Received: June 25, 2025; Revised: November 07, 2025

The research is focused on the relation between terrestrial and airborne gamma radiation and their roles in the gamma radiation background development. The terrestrial gamma radiation or ambient dose equivalent rate (DER) is measured at 1m (air dose rate) and at 0.10 m (terrestrial background radiation) above the ground, in a test field located on the Black Sea coast (Port of Burgas, Bulgaria), for a period of eighteen consecutive months. The measurements were performed by “Terra” dosimeter-radiometer MKS – 05 – a portable survey meter based on energy-compensated Geiger-Mueller counter**.** The results show mean values of gamma radiation background/air dose rate at the safe values of 0.129-0.183 μSv.h^{-1} and positive correlation between terrestrial and air dose rate at one and the same monitoring point. It was proved that the height has a significant influence on the measured DER values and closer to the ground levels, they are higher. There is positive correlation between air temperature and air dose rate of gamma radiation, substantially expressed above 1m from the ground surface.

Keywords: gamma radiation, air dose rate, terrestrial gamma radiation, dosimeter-radiometer, ionizing radiation

INTRODUCTION

The radiation background is usually formed from radiological sources of natural origin - such as rocks, soil, the radioactive gas radon (Rn) emitted from the ground, the cosmic radiation and the radioactive elements born from the interaction between it and the chemical elements in nature, etc. Both terrestrial (0.10 m above the ground) and airborne (1 m above the ground) radiation are forming the gamma radiation background. Combining terrestrial and airborne gamma radiation data provides a comprehensive understanding of radiation distribution, which is crucial for environmental health practices and radiological risk assessments [1-4].

Natural radioactivity mainly originates from the cosmogenic radionuclides produced by the interaction of cosmic-ray particles in the Earth atmosphere and terrestrial radionuclides with half-lives comparable to the age of the Earth, such as ^{40}K, and the radionuclides from the ^{238}U and ^{232}Th series. The three naturally occurring terrestrial radioisotopes ^{238}U, ^{235}U, and ^{232}Th emit neutrons through a spontaneous fission process and contribute to neutron backgrounds, as well as neutrons produced from (α, n) reactions, although their contribution is almost negligible [5, 6]. The largest contribution to external source of irradiation of the human body stems from gamma-emitting radioactive elements in the ground [7]. Terrestrial gamma radiation (TGR) mainly depends on geological and geographical conditions [8]. Terrestrial gamma radiation in beach sand is primarily influenced by the presence of natural radionuclides such as ^{232}Th (thorium-232), ^{238}U (uranium-238) and potassium-40 (^{40}K) [9, 10]. The composition of the sand significantly influences TGR at any given place. At the Burgas beach, the sand composition is related to the geological composition of the coast of the Burgas lowland, which includes mostly senonian limestones, marls and volcanics, eocene, oligocene, sarmatian and pliocene sediments, overlain by quaternary and modern deposits [11]. The energy of cosmic gamma photons is larger than 1 MeV and the radiation survey meter, we used – “Terra” dosimeter-radiometer MKS – 05 is sensitive to gamma photons from 0.05 to 3 MeV and there is a theoretical possibility to detect cosmic gamma photons by using it [12].

EXPERIMENTAL

The present research reviews the ground monitoring of gamma radiation or ambient dose equivalent rate/air dose rate (DER) and terrestrial background radiation, measured in μSv.h^{-1} for a period of eighteen months, from June 2021 till November 2022. The air dose rate - gamma radiation dose absorbed by air or ambient dose equivalent rate is measured at 1 m (DER_1) and the terrestrial background radiation at 0.10 m (DER_0.10), above the ground/sand in a test field, located on the Black Sea coast (Port of Burgas, Bulgaria). The survey was focused on the Black Sea, Burgas Bay ecosystem and consists of five monitoring points – Fig. 1, including

* To whom all correspondence should be sent:
E-mail: *sabina_nedkova@abv.bg*

three points within the Burgas Port, one on the bridge platform and one on the beach coast within Burgas salt pans area.

Fig. 1. Monitoring points of the survey alongside Black Sea Burgas Bay

The measurements were performed by the "TERRA" dosimeter-radiometer MKS – 05 – a portable survey meter, based on energy-compensated Geiger-Mueller counter. The MKS-05 "TERRA" dosimeter-radiometer is designed to measure ambient dose equivalent and ambient dose equivalent rate of gamma radiation (or photon-ionizing radiation), with ±15 % accuracy in the gamma energy range from 0.05 MeV to 3 MeV. It is designed for measurement of in the range of 0.001 to 9999 mSv. To measure the gamma/photon-ionizing radiation, the dosimeter was directed with its metrological mark "+" towards the examined area at the two chosen heights -1 m and 10 cm. The final values were obtained as an arithmetic mean of the last five measurements after the LCD of the survey meter stopped blinking.

The monitoring area was determined roughly as a circle with radius of 1 m and a center - the sampling point. Within the surveyed area around the sampling point, the radiological examination included three points, for the operator to stop and measure the gamma background. The three location points were placed approximately at the vertices of an equilateral triangle, with the center - the sampling point. The area thus formed was traversed at a speed of about 5-10 cm/s). The advantage of the survey meter we used is that there is a possibility to get a fast response in the field measurements and locate hot spots or any spot where the radiation shielding is not appropriate.

The data were processed and analyzed by the SPSS statistical data processing tool.

RESULTS AND DISCUSSION

The reliability of the data gathered was analyzed and reported with Cronbach's alpha coefficient of 0.702, which indicates good internal consistency among the items: air dose date, measured at 1m and ground–based (terrestrial) air dose rate (measured at 0.10 m above the ground). The mean values of the air dose rate at the two heights were within the safe limits (0.129-0.183 $\mu Sv.h^{-1}$)[1].

Mean values

The analyses of the mean values of the ambient dose equivalent rate, at 0.10 m (DER_0.10) and at 1 m (DER_1) of height showed 7 % higher values closer to the monitoring points surface (*MV DER_0.10=0.1709, MV DER_1=0.1593)* – Fig. 2.

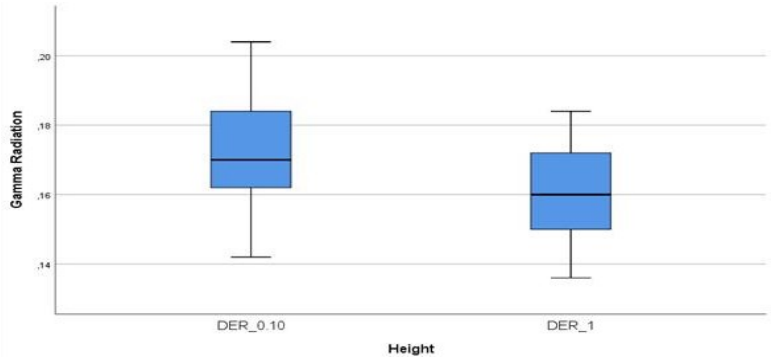

Fig. 2. Mean values of the ambient dose equivalent rate, at 0.10 m (DER_0.10) and at 1 m (DER_1)

[1] According to the Bulgarian legislation - Ordinance on basic norms for radiation protection, adopted by the Council of Ministers №229 / 25.09.2012 on the territory of the Republic of Bulgaria the natural radiation gamma background is considered safe, while in the range from 0.06 to 0.40 $\mu Sv.h^{-1}$.

Table 1. Correlation between ambient dose equivalent rate at 10 cm (DER_0.10) and at 1 m (DER_1)

DER_0.10 / DER_1	1.1	1.2	1.3	1.4	1.5
1.	**0.363**	-0.289	0.094	0.305	0.502*
2.	0.034	**0.705****	0.433	-0.295	-0.231
3.	-0.043	0.145	**0.710****	0.242	-0.026
4.	0.06	-0.361	0.109	**0.920****	0.242
5.	0.618**	0.02	0.128	0.153	**0.828****

*p<0.05, ** p<0.01.

This proves the fact that terrestrial gamma radiation dose rates are higher at the source due to direct exposure to radionuclides in the monitored areas. In contrast, airborne gamma radiation is subject to attenuation as it travels through the air, resulting in lower dose rates [14, 15]. The intensity of gamma radiation decreases as it passes through the air. This attenuation increases with the thickness of the air layer. For example, significant attenuation is observed when the air thickness exceeds 1 m, with lower energy gamma radionuclides like potassium-40 (^{40}K) being more attenuated compared to higher energy radionuclides like ^{232}Th (thorium-232), ^{238}U (uranium-238) [13].

Correlation between items

The overall correlation between the values of the items assessed by Pearson correlation analysis (Table 1) shows that: air dose rate DER_1 (measured 1 m above the ground/sand) on Monitoring point 1 (1), Monitoring point 2 (2), Monitoring point 3 (3), Monitoring point 4 (4), Monitoring point 5 (5) is always positively correlated with the ground based/terrestrial dose rate DER_0.10 (measured at 0.10 m above the ground/sand) (1.1) at monitoring point 1, (2.1) at monitoring point 2, (3.1) at monitoring point 3, (4.1) at monitoring point 4 and (5.1) at monitoring point 5.

The correlation is substantial at monitoring points 2, 3, 4 and 5 ($p<0.01$), and most significant ($r > 0.75$) at monitoring points 4 and 5.

ANOVA test

A clear correlation is seen between ambient dose equivalent rate (DER) average values at 0.10 m and at 1 m (Table 1). The analysis of one-way ANOVA test ($p = 0.047$) obtained from the statistical analysis with SPSS confirmed our observation. The parameter p is less than 0.050 and it can be concluded that the height has a significant influence on DER values. Higher values are closer to the monitoring points surface. Since the p-value of 0.047 is close to the cutoff threshold, it can be interpreted as modest, and further investigation or larger sample sizes might be beneficial to confirm this relationship.

The correlation between height and DER value, shows an average statistical significance and a positive correlation ($r = 0.333$).

Monthly fluctuation

Monthly fluctuation of ambient dose equivalent rate, at 0.10 m (DER_0.10=Gamma Burgas _10) and at 1 m (DER_1=Gamma Burgas), was developed for depiction of values relation with any natural variability and certain environmental influences as temperature and its seasonal fluctuations. As seen in Fig. 3, both values are following the same trajectory trend which has its highs during the summer months, clearly expressed in June 2021 and its lows in winter months, clearly expressed in December 2021, January and February 2022.

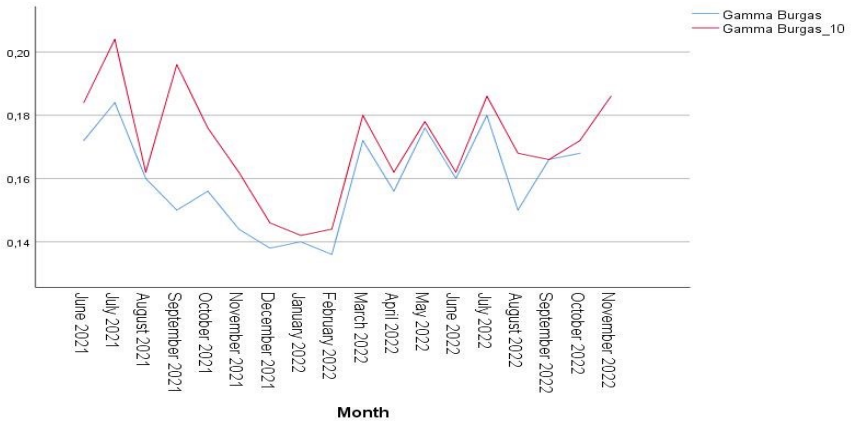

Fig. 3. Monthly fluctuation of ambient dose equivalent rate, at 0.10 m (DER_0.10=Gamma Burgas _10) and at 1 m (DER_1=Gamma Burgas)

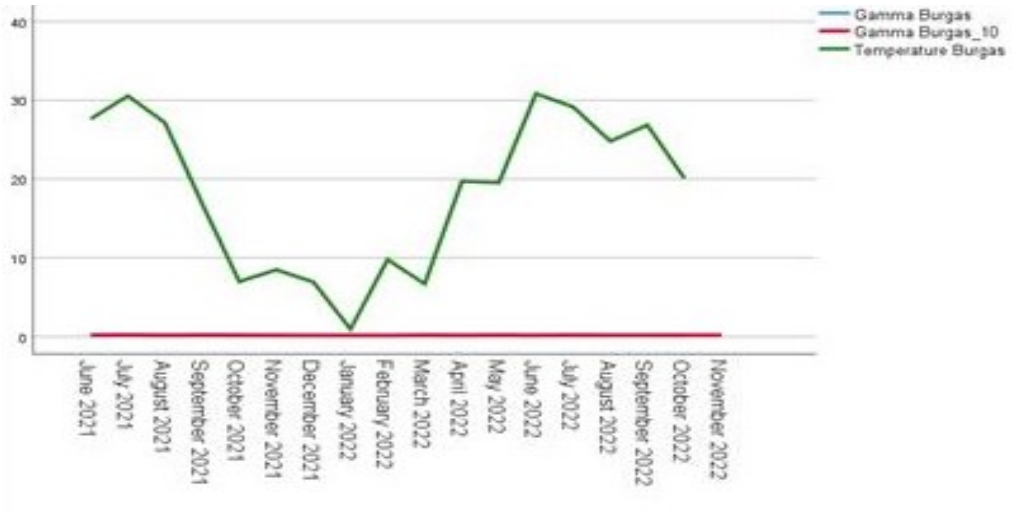

Fig. 4. Monthly fluctuation of ambient dose equivalent rate, at 0.10 m (DER_0.10=Gamma Burgas _10) and at 1 m (DER_1=Gamma Burgas) and the average temperature for the period June 2021-November 2022

Table 2. Correlation between mean values of air dose rate and ground-based dose rate

	DER_1 Gamma Burgas	DER_0.10 Gamma Burgas _10	Temperature Burgas
DER_1	1	0.771**	0.641**
DER_0.10	0.771**	1	0.488*
Temperature Burgas	0.641**	0.488*	1

*p<0.05, ** p<0.01.

Comparing the average temperature (specified in units of degrees Celsius (°C) measured with a humidity & temperature meter), of the five monitoring points and the values of the gamma radiation at DER_1 and DER_0.10 it is seen, that the temperature highs and lows are following the same trend as that of the measured gamma radiation – Fig. 4. The direct relation between these two variables could be seen also in Table 2. Both relations are positive (r=0.641, r=0.488) and substantial (p<0.01 and p<0.05). The relation between the air temperature and the gamma radiation at 1 m height is significant, which could be directly related to the sunlight and its role in heating the air and at the same time its connection with photons and gamma radiation. The values prove that temperature plays a crucial role in the observed gamma radiation level.

CONCLUSIONS

The relation between terrestrial and airborne gamma radiation helps in assessing environmental radiation background and contributes in understanding the roles of different sources in the gamma radiation background development.

Based on the above listed results, it could be concluded that:

The height has a significant influence on the measured ambient dose equivalent rate (DER) values. Since the values of the radiation measured at the two heights are different and all the monitoring points in the test field were exposed to the same cosmic radiation, there is a possibility to assess a relative contribution of terrestrial gamma radiation at the different monitoring points, due to direct exposure to radionuclides in the monitored areas.

The values prove that temperature plays a crucial role in the observed gamma radiation level. The relation between the air temperature and the gamma radiation at 1 m height is significant, which could be directly related to the sunlight and its role in heating the air.

Acknowledgement: *The study was performed with the support of the project "Cross-border regions cooperate for BLUE GROWTH COLLABs", CB005.3.12.001, funded by the Interreg Program – IPA for cross-border cooperation Bulgaria - Turkey 2014-2020 (Interreg IPA Cross- border Cooperation Bulgaria - Turkey Program).*

REFERENCES

1. M.S.M Sanusi, A.T Ramli, H.T Gabdo, N.N Garba, A Heryanshah, H Wagiran, M.N Said, *Journal of Environmental Radioactivity*, **135**, 67 (2014).
2. G. Cinelli, F. Tondeur, B. Dehandschutter, F. Menneson, J. Rincones, *Journal of Environmental Radioactivity*, **248**, 106885 (2022).

3. P. Martin, S. Tims, A. McGill, B. Ryan, K. Pfitzner, *Environmental Monitoring and Assessment,* **115**, 531 (2006).
4. C. L. Folly, G. Konstantinoudis, A. Mazzei-Abba, C. Kreis, B. Bucher, R. Furrer, B. D. Spycher, *Journal of Environmental Radioactivity*, **233**, 106571(2021).
5. S. Avdic, I. Gazdic , M. Music, B. Pehlivanovic, *Nuclear Technology & Radiation Protection*, **31**, 121 (2016).
6. M. F. Becchetti, M. Flaska, S.D. Clarke, S.A. Pozzi., *Nuclear Instruments and Methods in Physics Research, Section A*, **777**, 1 (2015).
7. UN Scientific Committee on the Effects of Atomic Radiation, UNSCAR I, (2008).
8. H. Florou, P. Kritidis, *Radiation Protection Dosimetry*, **45**, 277 (1992).
9. G. S. Gusain, B. S. Rautela, S. K. Sahoo, T. Ishikawa, G. Prasad, Y. Omori, A. Sorimachi, S. Tokonami, R. C. Ramola, G. S. Gusain, *Radiation Protection Dosimetry*, **152** (1-3), 42, (2012).
10. E. S. Joel, M. Omeje, O. C. Olawole, *Sci. Rep*., **11**, 17555 (2021).
11. Marine spatial plan of the Republic of Bulgaria 2021-2035
12. Operating manual, MKS-05 "TERRA" dosimeter-radiometer
13. A. Mishra, R. Khanal*, Kuwait Journal of Science,* **50** (3 B), (2023).
14. J. Wilford, B. Minty, *Developments in Soil Science,* **31** (C), 207 (2006).

Bulgarian Chemical Communications, Volume 58, Special Issue A (pp. 10-15) 2026 DOI: 10.34049/bcc.58.A.SN-02

In silico assessment of skin sensitization potential of polyphenolic metabolites from *Sideritis syriaca* using QSAR toolbox

G. Rusev*, V. Dzhogov, L. Gonsalvesh

[1]*Department of Chemistry, Burgas State University "Prof. Assen Zlatarov", 1 Prof. Yakimov Str., 8010 Burgas, Bulgaria*

Received: August 10, 2025; Revised: November 24, 2026

Accurate prediction of skin sensitization potential and potency is essential for the safety of consumers and workers across multiple industries, including cosmetics, pharmaceuticals, and nutraceuticals. Although animal testing has traditionally served as the gold standard for hazard assessment, the development and adoption of non-animal and *in silico* approaches are rapidly advancing in response to ethical and regulatory demands. In this study, the skin sensitization risk of ten predominant polyphenolic compounds isolated from *Sideritis syriaca* was evaluated using the QSAR toolbox (version 4.7.1). Available *in vivo* data were limited, with only one compound having published results. Protein-binding alerts, as identified by the OASIS profiler, were detected in two of the parent compounds. Further simulation of abiotic and metabolic transformation pathways generated 89 predicted metabolites, uncovering mechanistic alerts including Michael addition, nucleophilic addition, Schiff base formation, acylation, and radical-mediated reactions. Among the compounds studied, verbascoside exhibited the highest predicted reactivity. While most parent compounds displayed a low sensitization hazard, simulation of their metabolites indicated potential for downstream risk. These findings underscore the utility of *in silico* tools for robust and early safety evaluation of plant-derived secondary metabolites and support the ongoing transition toward animal-free toxicological assessments.

Keywords: Skin sensitization, *in silico*, metabolic simulation, polyphenols, QSAR toolbox

INTRODUCTION

Skin sensitization testing is a regulatory cornerstone for the safety assessment of chemical ingredients, particularly in the cosmetics industry, prior to their market release. Historically, skin sensitization hazard identification relied predominantly on animal-based models. The guinea pig maximization test, established by Magnusson and Kligman [1], was one of the earliest standardized assays for evaluating a chemical's potential to induce human skin sensitization. This was subsequently superseded by the murine local lymph node assay (LLNA), recognized for its higher sensitivity, improved quantification of allergic potency, and suitability for dose–response assessment [2]. The landscape of skin sensitization testing has, however, evolved dramatically in response to regulatory, ethical, and scientific developments. The implementation of the European Union Cosmetics Directive (Regulation (EC) No 1223/2009), notably Article 18, and the REACH regulation (EC No 1907/2006), strictly prohibit animal testing for cosmetic ingredients and finished products, setting a precedent for similar restrictions worldwide. In parallel, increased societal concern for animal welfare and strengthened international consensus have catalyzed the development and validation of alternative test methods, in alignment with the principles of the 3Rs (Replacement, Reduction, Refinement).

Concurrently, our understanding of the immunological mechanisms underlying skin sensitization has deepened. Skin sensitization is now recognized as an adaptive immune reaction, tightly orchestrated through a cascade of molecular and cellular events occurring across two primary phases: induction and elicitation. Advances in toxicological research have culminated in the adverse outcome pathway (AOP) framework for skin sensitization [3], codified in the OECD Test Guideline No. 497. Briefly, this AOP encompasses four well-defined key events: (*i*) covalent binding of electrophilic chemicals (haptens) to skin proteins, (*ii*) keratinocyte activation and release of pro-inflammatory signals, (*iii*) activation and maturation of dendritic cells and their migration to lymph nodes, and (*iv*) proliferation of antigen-specific T-cells, ultimately leading to allergic contact dermatitis upon re-exposure. Given the complexity of these biochemical interactions and their relevance to public health, the accurate assessment of skin sensitization potential has become critically important, especially as a wider array of natural

* To whom all correspondence should be sent:
E-mail: *georgi-rusev@uniburgas.bg*

substances—including botanicals, nutraceuticals, and phytopharmaceuticals—enters consumer product markets [4].

Computational (*in silico*) approaches such as quantitative structure–activity relationship (QSAR) modeling and expert rule-based systems have emerged as essential tools for predicting sensitization hazards, capable of integrating vast datasets, minimizing animal use, and supporting regulatory compliance [5]. These models, often calibrated to LLNA and human data, are especially valuable for screening large chemical libraries and structurally diverse secondary metabolites, including those from medicinal plants such as *Sideritis syriaca*. A skin sensitizer, as defined by the Globally Harmonized System (GHS) and REACH, is any substance that induces an allergic response following repeated dermal exposure. The present study aims to predict the skin sensitization potential of the ten selected secondary metabolites from *Sideritis syriaca* by applying the OECD QSAR toolbox (v.4.7.1), evaluating both the parent compounds and their putative metabolites generated *via* simulation of abiotic and skin metabolic pathways. This approach provides a comprehensive, animal-free evaluation framework that aligns with current scientific and regulatory standards.

METHODOLOGY

Using QSAR toolbox (version 4.7.1), the ten plant secondary metabolites, named as parent compounds (Supplementary Table), with the highest concentrations (ranging from 11 to 95 $mg \cdot g^{-1}$ extract), identified *via* HPLC-MS/MS analysis of methanolic extracts from both cultivated and wild *Sideritis syriaca*, were selected for evaluation. HPLC-MS/MS is a powerful analytical technique widely used for the separation, identification, and quantification of polyphenols in complex matrices such as plant extracts, foods, and biological samples. The method combines the high-resolution separation capability of high-performance liquid chromatography (HPLC) with the specificity and sensitivity of tandem mass spectrometry (MS/MS), enabling the detection and structural elucidation of a broad range of polyphenolic compounds, including phenolic acids, flavonoids, and their derivatives [6]. MS/MS fragmentation patterns are crucial for identifying polyphenol classes, as each class displays a characteristic cleavage behavior that reflects their core structure and substituents. For flavonoids, common fragmentation pathways include Retro-Diels-Alder (RDA) reactions in the C-ring, which generate diagnostic ions, and alpha-cleavage or loss of sugar moieties for glycosides, producing aglycone fragments. Phenolic acids typically show losses of CO_2, CO, and H_2O, with methoxy groups cleaving at lower energies, aiding in their differentiation. Glycosylated polyphenols exhibit neutral losses corresponding to the sugar unit (e.g., 162 Da for hexoses, 120 Da for pentoses), and the fragmentation pattern can distinguish between O-glycosides and C-glycosides, as C-glycosides often show more complex sugar fragmentation and water loss. These reproducible fragmentation trees enable confident identification and classification of polyphenols in complex samples [7].

The compounds comprised three phenolic acids (syringic, salicylic, gentisic), three cinnamic acid derivatives (caffeic, ferulic, chlorogenic) [8], the phenylethanoid glycoside verbascoside, the flavone apigenin, and two flavanols – kaempferol and isorhamnetin [9]. Where available, *in vivo* skin sensitization data (LLNA and GPMT) were retrieved and analyzed. Further profiling of the selected parent structures was conducted using the OASIS protein-binding profiler. Additionally, two simulation modules were applied to predict the formation and reactivity of potential metabolites: the abiotic autoxidation simulator and the skin sensitization metabolism simulator [3, 10].

Autoxidation (AO) refers to the spontaneous oxidation of organic molecules triggered by exposure to air [11, 12]. This process involves a free-radical chain reaction between the compound and molecular oxygen, leading to the production of various oxidation products. Among these, organic hydroperoxides are considered especially significant due to their potential to cause adverse effects such as contact allergy. To investigate and predict AO pathways, an AO model was designed. A training set comprising 140 chemicals—including terpenes, simple aliphatic and polyethyleneglycol ethers, aldehydes, and aminophenols—with published data on AO pathways was assembled. To ensure data consistency, experimental conditions were standardized: exposure to air or oxygen at room temperature and atmospheric pressure, in bulk or with different solvents, and under nearly neutral (pH 7–7.5) or slightly alkaline (pH 8–9) conditions. The duration of AU ranged from a few hours to several months. The AU simulator is based on a collection of molecular transformations extracted from these documented AO pathways.

The skin metabolism simulator (SMS) is designed to replicate how chemicals are metabolized within the skin compartment. Due to the scarcity of experimental data on skin metabolism and the prevailing assumption that skin enzymes process xenobiotics in ways similar to the liver, the simulator

is modeled as a streamlined version of a mammalian liver metabolism simulator. The SMS employs a structured sequence of primary transformations, categorized into two types:

- Rate-determining transformations: These include Phase I and Phase II metabolic reactions such as C-hydroxylation, ester hydrolysis, oxidation, glutathione conjugation, glucuronidation, and sulfonation.
- Non-rate-determining transformations: These involve molecular changes of highly reactive intermediates that occur following the primary metabolic steps.

Simulation process begins by comparing the parent compound to a set of reaction fragments, focusing on the transformation with the highest likelihood of occurring. This yields a group of first-level metabolites. Each new metabolite formed is evaluated using the same sequence of hierarchical transformations, generating a second tier of metabolites. The simulation continues iteratively, processing each metabolite, until it meets specific propagation constraints—for example, when the likelihood of forming additional metabolites becomes low or when a Phase II reaction has taken place.

RESULTS AND DISCUSSION

Protein-binding alerts associated with skin sensitization were identified in only two of the ten evaluated parent compounds – verbascoside and chlorogenic acid. Both compounds possess aromatic rings linked to side chains with conjugated double bonds (alternating single and double bonds), often adjacent to electron-withdrawing groups like carbonyls (C=O). This arrangement increases the electrophilicity (electron deficiency) of certain carbon atoms, making them reactive toward nucleophilic groups (e.g., amino acids in skin proteins). The presence of a carbonyl group (C=O) at the β-position (two atoms away from a reactive center) polarizes the double bond, further enhancing its reactivity. This is a hallmark of structures prone to Michael-type addition (Fig. 1).

This reaction involves the addition of a nucleophile (such as the amino group of a skin protein) to an α, β-unsaturated carbonyl compound. The conjugated system with a polarized double bond acts as an electrophilic trap for nucleophiles, facilitating covalent protein binding – a recognized mechanism in skin sensitization.

Upon application of the abiotic autoxidation simulator, 26 metabolites were generated from six parent structures. These metabolites exhibited protein-binding alerts across four mechanistic domains: Michael addition, Acylation, Radical-based reactions and Schiff base formation. Autoxidation typically generates reactive oxygen species (ROS) and may modify certain chemicals to more reactive forms. The detailed results show that more metabolites have been generated for isorhamnetin and kaempferol (10 for each compound). Three of them, which are similar for both chemicals, have no structural alerts.

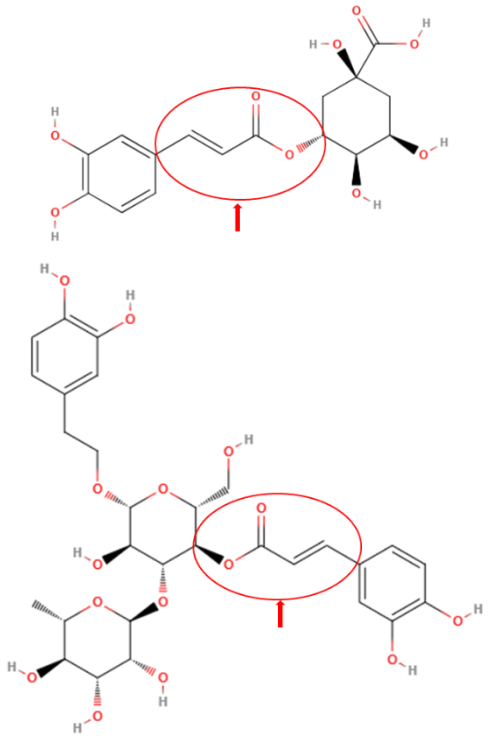

Fig. 1. Reactive centers for two of the parent structures – chlorogenic acid (up) and verbascoside (down).

Both molecules possess several free hydroxyl groups on their aromatic rings, especially at positions that are highly susceptible to oxidation (e.g., 3, 5, 7, and 4′ for kaempferol; 3, 5, 7, and 4′ for isorhamnetin, with the 3′ position methylated in isorhamnetin – Fig. 2).

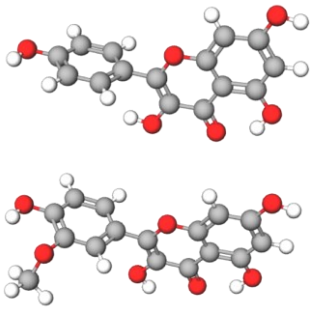

Fig. 2. 3D molecular models of kaempferol (up) and isorhamnetin (down). C atoms are gray, H atoms are white and O atoms are red.

These hydroxyl groups facilitate the formation of phenoxyl radicals, which can undergo further transformation, leading to a cascade of chemical reactions and metabolite diversity.

The conjugated double bonds in the flavanol structure allow for electron delocalization, making the molecules more reactive toward oxygen and free radicals. This delocalization promotes the formation of quinones, ring-opened products, and other oxidized derivatives [13, 14]. The presence of multiple hydroxyl groups, especially at the 3-position, gives these compounds a high hydrogen-donor capacity, which is crucial for initiating autoxidation and subsequent metabolite formation (Fig. 3).

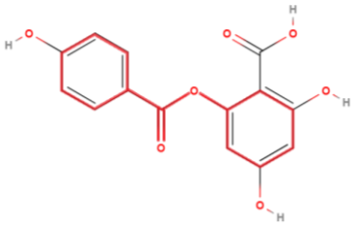

Fig. 3. One of the isorhamnetin-generated metabolites with possible active sites (centers).

For the caffeic and chlorogenic acids two metabolites have been generated. The two chemicals are highly prone to autoxidation due to the catechol structure, leading to rapid formation of o-quinones, dimers, and polymeric products [15]. The primary pathway involves hydrogen atom transfer and radical adduct formation, resulting in cyclic metabolites and oxidized dimers. With two generated metabolites for each compound after simulated abiotic autoxidation apigenin and verbascoside show moderate diversity.

When using an autoxidation metabolic simulator on phenolic acids such as syringic, salicylic, gentisic and ferulic acids, several factors could explain the absence of predicted metabolites – lack of highly reactive functional groups and methoxy group stabilization [16]. These phenolic acids possess relatively simple structures without highly reactive sites (such as ortho-dihydroxy or α, β-unsaturated carbonyl groups) that are more prone to autoxidation. For example, syringic acid has methoxy substituents that stabilize the aromatic ring, while salicylic and gentisic acids have hydroxyl groups that do not favor easy radical formation or further transformation under mild oxidative conditions. In syringic acid, the methoxy groups at the 3- and 5- positions increase the bond dissociation enthalpy of the phenolic O–H bond, making radical formation less favorable and thus reducing the likelihood of autoxidative transformation. These phenolic acids are known for their antioxidant properties, meaning that they can efficiently neutralize free radicals rather than propagate radical chain reactions [17, 18]. This property can limit their own autoxidation and the subsequent formation of detectable metabolites. In some cases, phenolic acids can form dimers or quinones upon oxidation, but these reactions may require specific conditions (e.g., high pH, presence of metal ions, or enzymatic catalysis) that are not replicated in the simulator's standard autoxidation model. Studies have shown that benzoic acid derivatives (which include syringic, salicylic, and gentisic acids) are less prone to autoxidation compared to cinnamic acid derivatives, often taking part in side reactions rather than producing distinct oxidation products under standard conditions [19,20]. The antioxidant and radical-scavenging nature of ferulic acid also limits further oxidation under mild conditions. It possesses a methoxy group and a conjugated side chain, which can participate in radical reactions, but under standard autoxidation, the main products are often dimers or oligomers rather than distinct small-molecule metabolites.

The skin sensitization metabolism simulator yielded 63 metabolites derived from nine of the ten parent compounds [21–23]. The only one compound with no metabolites generated is salicylic acid. Its structure lacks electrophilic centers or functional groups that could readily undergo autoxidation to form reactive metabolites under physiological conditions. In autoxidation, salicylic acid can act as a free radical scavenger rather than a substrate that forms reactive intermediates. The main reaction with ROS (such as hydroxyl radicals) leads to hydroxylation, producing minor metabolites like 2,3- and 2,5-dihydroxybenzoic acid, but not highly reactive or protein-binding metabolites. These metabolites are not considered electrophilic enough to form stable protein adducts, which are crucial for skin sensitization. Salicylic acid does not generate metabolites with structural alerts for skin sensitization because its metabolic products (mainly through hydroxylation and conjugation) are not electrophilic and do not form covalent bonds with proteins. The other two cinnamic acid derivatives (caffeic actd and ferulic acid) generated 1 and 4 metabolites, respectively. For two of the ferulic acid metabolites there is no alert. The rest 3 show mechanistic alert Michael addition on quinoid type compounds and Schiff base formation with carbonyl compounds (Fig. 4).

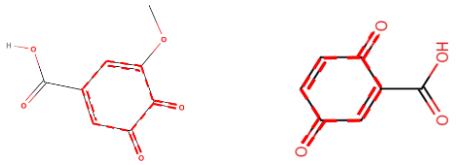

Fig. 4. Structural formulas of two of the generated metabolites for syringic and gentisic acids (red dashed lines show possible reactive sites)

Ortho-quinones and para-quinones can react with proteins through 1,4-addition, in which the amino group (NH_2) of lysine or the thiol group (SH) of cysteine adds across the quinone ring system [24]. These quinones are typically generated by oxidation of para- and ortho-dihydroxy aromatic compounds (pro-Michael acceptors) which, through well-established metabolic or abiotic transformations, become Michael acceptors—for example, the oxidation of hydroquinone to benzoquinone. This Michael-type addition allows covalent bond formation at an electrophilic center without the need for a leaving group [25]. The reactive groups of the Michael acceptor can be present either in open-chain form or as part of a ring structure, such as a quinone (Fig. 4).

Similarly, ortho- and para-aminophenols, after undergoing metabolic or abiotic transformation, can form quinone imines which also react with proteins *via* Michael-type addition. Nitrophenols, following metabolic or abiotic processes such as keto-aci tautomerism, can form nitroquinones that react with proteins in the same manner. For instance, 2,4-dinitrophenol acts as a cellular metabolic toxin, and exposure may provoke allergic reactions including hives, blisters, or unexplained rashes [26]. Additionally, aromatic primary or secondary amines situated ortho to a nitro group may induce sensitization through the formation of aci-tautomers. However, for Michael adducts to form by 1,4-addition, at least one position on the aromatic ring must remain unsubstituted.

A comprehensive assessment of the *in vivo* and *in vitro* data available for all compounds generated by the two simulation models (AO and SMS) demonstrated that such information exists for only a limited subset of the 89 predicted metabolites. For the three cinnamic acid derivatives investigated (caffeic, ferulic, and chlorogenic acids), *in vivo* and *in vitro* data were identified solely for two metabolites of ferulic acid generated by AO and SMS, namely formaldehyde and formic acid. Evidence of potential skin sensitization, including positive test outcomes, was observed only for formaldehyde, whereas the *in vivo* and *in vitro* data for formic acid were negative. For the three phenolic acids examined – syringic, salicylic, and gentisic acids – experimental data were available exclusively for two metabolites of syringic acid, again identified as formaldehyde and formic acid [27]. A systematic review of *in* vivo and *in vitro* data for metabolites generated from the phenylalanine glycoside verbascoside by the SMS simulator revealed that *in vivo* information is available for only one out of the 28 predicted metabolites – hydroxytyrosol, which has been characterized as a possible skin sensitizer [28]. *In vitro* data exist solely for D-(+)-glucose, which has been found to yield negative results. No experimental data were found for the flavone apigenin. For the two flavanols, isorhamnetin and kaempferol, data are available for two distinct compounds: *in vivo* data for vanillic acid indicate no evidence of skin sensitization [29], while *in vitro* data for para-salicylic acid are also negative [30].

CONCLUSIONS

In silico methods using the QSAR toolbox can effectively predict the skin sensitization potential of polyphenolic compounds and their metabolites, supporting animal-free toxicological assessment approaches. Among the ten polyphenolic parent compounds examined, most showed low skin sensitization hazard; however, two parent compounds – verbascoside and chlorogenic acid – displayed protein-binding alerts indicative of potential sensitization mechanisms such as Michael addition. Simulation of abiotic autoxidation and skin metabolism pathways generated 89 predicted metabolites, many with mechanistic alerts including Michael addition, Schiff base formation, acylation, and radical-mediated reactions, revealing a higher risk of sensitization from metabolites than from parent compounds alone. Verbascoside exhibited the highest predicted reactivity and number of reactive metabolites, highlighting molecular complexity as a factor that increases potential sensitization risk. Certain compounds like syringic, salicylic, gentisic, and ferulic acids were less prone to autoxidation and did not generate metabolites with sensitization alerts due to structural features that confer antioxidant stability. The findings emphasize the critical role of metabolic transformation in modulating skin sensitization risk and the utility of combining abiotic and metabolic simulation to comprehensively evaluate hazards of natural product secondary metabolites. The overall results support the use of computational models aligned with regulatory frameworks such as the OECD adverse outcome pathway for skin sensitization as robust tools for early safety evaluation, aiding industry compliance with animal testing bans and promoting ethical research. The paucity of available experimental data

underscores the necessity for robust physicochemical and mathematical models to enable accurate forecasting and prediction of the potential metabolic activities of the compounds under investigation.

REFERENCES

1. B. Magnusson, A. M. Kligman, *J. Invest. Dermatol.,* **52**, 268 (1969).
2. D. A. Basketter, P. Evans, R. J. Fielder, G. F. Gerberick, R. J. Dearman, I. Kimber, *Food Chem. Toxicol.,* **40**, 593 (2002).
3. G. Patlewicz, C. Kuseva, A. Kesova, I. Popova, T. Zhechev, T. Pavlov, D. W. Roberts, O. Mekenyan, *Regul. Toxicol. Pharmacol.,* **69**, 529 (2014).
4. A. Goossens, *Cosmetics,* **3**, 1 (2016).
5. V. Rogiers, M. Pauwels, *Curr. Probl. Dermatol.,* **36**, 129 (2008).
6. A. M. Mustafa, S. Angeloni, D. Abouelenein, L. Acquaticci, J. Xiao, G. Sagratini, F. Maggi, S. Vittori, G. Caprioli, *Food Chem,.* **367**, 130743 (2022).
7. Á. Fernández-Ochoa, M. de la Luz Cádiz-Gurrea, A. Segura Carretero, editor H. Koolen. Springer US, New York, NY, 2022, p. 31.
8. D. Li, Y. xin Rui, S. duo Guo, F. Luan, R. Liu, N. Zeng, *Life Sci.* **284**, 119921 (2021).
9. M. D. Navarro-Hortal, A. Varela-López, J. M. Romero-Márquez, L. Rivas-García, L. Speranza, M. Battino, J. L. Quiles, *Food Chem. Toxicol.* **146** (2020).
10. J. C. Madden, S. Webb, S. J. Enoch, H. E. Colley, C. Murdoch, R. Shipley, P. Sharma, C. Yang, M. T. D. Cronin, C*omput. Toxicol.,* **3**, 44 (2017).
11. E. M. Marinova, N. V. Yanishlieva, *Food Chem.,* **81**, 189 (2003).
12. M. Leopoldini, T. Marino, N. Russo, M. Toscano, *J. Phys. Chem. A* **108**, 4916 (2004).
13. N. Ruseva, A. Bakalova, E. Cherneva, *J. Chem. Technol. Metall.,* **60**, 881 (2025).
14. P. Chaudhary, P. Janmeda, A. O. Docea, B. Yeskaliyeva, A. Faizal, A. Razis, B. Modu, D. Calina, J. Shari, *Front. Chem.* **1** (2023).
15. M. Y. Moridani, H. Scobie, A. Jamshidzadeh, P. Salehi, P. J. O'Brien, *Drug Metab. Dispos*. **29**, 1432 (2001).
16. S. Hong, M. Yoon, *J. Cosmet. Med.,* **6**, 89 (2022).
17. M. Platzer, S. Kiese, T. Tybussek, T. Herfellner, *Front. Nutr.* **9,** 4 (2022).
18. A. Zeb, *J. Food Biochem.,* **1** (2020).
19. K. Barasker, M. Sciences, 12, 173 (2024).
20. Y. Zheng, Y. Zhou, R. Guo, Z. Fu, D. Chen, *LWT - Food Sci. Technol.,* **120**, 108932 (2020).
21. S. D. Dimitrov, L. K. Low, G. Y. Patlewicz, P. S. Kern, M. H. I. Comber, R. D. Phillips, P. T. Bailey, O. G. Mekenyan, *Int. J Toxicol.,* **189** (2005).
22. I. Bialas, S. Zelent-Kraciuk, K. Jurowski, *Toxics* , **11**, 392 (2023)
23. C. Johnson, E. Ahlberg, L. T. Anger, L. Beilke, R. Benigni, J. Bercu, S. Bobst, D. Bower, A. Brigo, S. Campbell, M. T. D. Cronin, I. Crooks, K. P. Cross, T. Doktorova, T. Exner, D. Faulkner, I. M. Fearon, M. Fehr, S. C. Gad, V. Gervais, A. Giddings, S. Glowienke, B. Hardy, C. Hasselgren, J. Hillegass, R. Jolly, E. Krupp, L. Lomnitski, J. Magby, J. Mestres, L. Milchak, S. Miller, W. Muster, L. Neilson, R. Parakhia, A. Parenty, P. Parris, A. Paulino, A. Theresa, D. W. Roberts, H. Schlecker, R. Stidl, D. Suarez-Rodrigez, D. T. Szabo, R. R. Tice, D. Urbisch, A. Vuorinen, B. Wall, T. Weiler, A. T. White, J. Whritenour, J. Wichard, D. Woolley, C. Zwickl, G. J. Myatt, *Regul. Toxicol. Pharmacol.,* **116**, 104688 (2020).
24. N. Shu, L. G. Lorentzen, M. J. Davies, *Free Radic. Biol. Med.,* **137**, 169 (2019).
25. X. Wang, B. Thomas, R. Sachdeva, L. Arterburn, L. Frye, P. G. Hatcher, D. G. Cornwell, J. Ma, *Proc. Natl. Acad. Sci. USA.***103,** 3604 (2006).
26. W. Ye, U. I. Seneviratne, M. Chao, K. C. Ravindra, G. N. Wogan, S. R. Tannenbaum, P. L. Skipper, 2627 (2012).
27. P. S. Kern, G. F. Gerberick, C. A. Ryan, I. Kimber, A. Aptula, D. A. Basketter, *Dermat. Contact, Atopic, Occup. Drug,* **21**, 8 (2010).
28. European Chemical Agency (2022). Formaldehyde. Retrieved from [https://echa.europa.eu/bg/registration-dossier/-/registered-dossier/15858/7/5/2]
29. European Chemical Agency (2022). Vanillic acid. Retrieved from [https://echa.europa.eu/es/registration-dossier/-/registered-dossier/26471/7/5/2/?documentUUID=a0340efe-42ec-4196-b8dc-43f03ce311d0]
30. Natsch, C. A. Ryan, L. Foertsch, R. Emter, J. Jaworska, F. Gerberick, P. Kern, *J. Appl. Toxicol*., **33**, 1337 (2013).

Bulgarian Chemical Communications, Volume 58, Issue A (pp. 16-21) 2026 *DOI: 10.34049/bcc.58.A.SN-03*

Extraction of microplastics from marine sediment in Burgas Bay, Black Sea

S. Turmanova[1], Y. Hristov[1], D. Kiryakova[1]*, E. Ivanova[2], P. Atanasova[1], G. Kolchakova[1], A. Ilieva[3], E. Mollova[2], A. Dimitrov[2], N. Todorov[2], G. Grigorova[4]

[1]Department of Materials Science, [2]Department of Ecology and Environmental Protection, [3]Department of Chemical Technologies, [4]Department of Biotechnology, Burgas State University „Prof. Dr. Assen Zlatarov", 1 Prof. Y. Yakimov Str., Burgas 8010, Bulgaria

Received: June 17, 2025; Revised: November 24, 2025

The present study aims a comparative analysis of the effectiveness of three salt solutions for the extraction of microplastic pollution in marine sediment samples from the Burgas Bay, Black Sea. For this purpose, pre-purified sediments were artificially contaminated with known amounts of five different types of microplastics (high density polyethylene, polyamide, polyethylene terephthalate, polymethyl methacrylate, and polyvinyl chloride). Based on the density differences between sediment and microplastics, the extraction was carried out using salt solutions of sodium chloride (1.20 g/cm³), magnesium chloride (1.26 g/cm³), and calcium chloride (1.30 g/cm³). To identify and quantify micropolymer particles in the sediments, the samples were analyzed by μ-FT-IR and processed with the Purency Microplastics Finder software.

Keywords: extraction, microplastics, marine sediment, Burgas Bay, Black Sea, μ-FT-IR

INTRODUCTION

The problem of microplastics (MPs) contamination of soils, atmospheric air, drinking and seawater, sediment, biota, and food on a regional and global scale has been widely reported in the literature, and their presence in these environments increases the risk to various organisms and human health. The presence of MPs in water, sediment, and biota is used as an indicator for assessing the quality of the marine environment and its components, according to the EU Marine Strategy Framework Directive and the Oslo Paris Convention. It is believed that, in the aquatic environment, MPs tend to deposit and accumulate in sediments, and Simon-Sánchez *et al.* [1] suggest that the seabed is a major sink of MPs pollutants.

To assess the degree of MPs contamination in sediment samples and to ensure the comparability, repeatability, and reproducibility of the obtained data, it is necessary to create a standardized methodology that follows uniform protocols for sampling and methods for preparation, extraction, and analysis of MPs. However, such unified protocols and standard methods have not been developed to date, which makes it impossible to draw valid conclusions about the amount and nature of MPs contamination in sediments.

To date, various methods have been proposed for the extraction of polymer particles, ranging from methods based on density separation, methods based on density separation in combination with other techniques, extraction with solvent or petroleum, as well as complex methods based on oleophilic, electrophilic, or magnetic properties [2–6]. All of them differ in the chemicals used, operating time and efficiency, and the latter methods have limited application due to the expensive equipment required.

The technique that relies on the variations in densities between microplastics and the sediment matrix is the most commonly employed method and serves as the primary approach for isolating MPs in the majority of studies conducted thus far. The separation between sediments and MPs is achieved by preparing a salt solution with a fixed density, mixing them in an appropriate ratio, and allowing the mixture to stand for a certain period. In this case, the heavier particles of the sediments settle (their average density is 2.65 g/cm^3 [7]), while the lighter particles of synthetic polymers (their maximum density is 1.58 g/cm^3 [6]) float to the surface of the solution. The MPs can then be separated (filtered) and analyzed. In this process, the choice of the density of the extraction solution in relation to that of the polymer type is crucial [8].

Although density separation approaches are considered easy to apply, to achieve a good degree of extraction of MPs, it is necessary to use salt solutions with appropriate densities depending on the type of polymers [8]. Furthermore, the extraction of MPs from real samples can be affected by a number of factors such as matrix complexity, sample

* To whom all correspondence should be sent:
E-mail: *dskiryakova@abv.bg*

volume and/or mass, different types and chemical compositions of polymer particles, sometimes with overlapping densities, a wide range of sizes and shapes, different degrees of aging, surface charge, hydrophobicity, presence of additives, contaminants, and residues of organic matter.

The aim of this study was to evaluate the efficiency of extracting MPs from marine sediment in Burgas Bay, Black Sea, by a method based on density differences using three different salt solutions – sodium chloride (NaCl), calcium chloride ($CaCl_2$) and magnesium chloride ($MgCl_2$). To identify and classify the quantitative presence of MPs contamination in the sediment samples, the samples were analyzed by μ-FT-IR.

EXPERIMENTAL

Preparation of marine sediments and their contamination with microplastics

Marine sediments from the Burgas Bay, Black Sea, were preliminarily purified by thermal treatment at 850°C for 60 min. The samples were subsequently contaminated with particles of high-density polyethylene (HDPE), polyamide (PA), polyethylene terephthalate (PET), polymethyl methacrylate (PMMA), and polyvinyl chloride (PVC) in sizes 100 – 200 μm.

Extraction of micropolymers

The extraction of the MPs from the matrix was carried out by a method based on differences in density. Three salts with different densities of their saturated solutions were used: NaCl (ρ = 1.20 g/cm^3), $MgCl_2$ (ρ = 1.26 g/cm^3), and $CaCl_2$ (ρ = 1.30 g/cm^3). Saturated solutions were prepared and filtered. The extraction was carried out by the flotation method, in which the sediments were mixed with the selected salt solution and barbotated for one h at room temperature. The samples were left for 24 h until the sediment completely settled. This was followed by decantation of the solutions and additional treatment with 30% H_2O_2 on stirring at 400 rpm.

Filtration and drying

The floating fraction of the purified sediment samples contaminated with micropolymer particles was filtered using a vacuum pump and filtration system through an Anodisk (Al_2O_3) filter with a pore size of 0.2 μm. The filters were then washed with distilled H_2O and dried at 40°C. For comparison, a control sample of purified sediment and ultrapure water was made.

Identification of microplastics

The filters were analyzed by μ-FT-IR imaging microscope (LUMOS II, Bruker), a focal plane detector with dimensions of 32×32 and a spatial resolution of 5 μm was used. The scan was performed in the range of 4000 to 1000 cm^{-1} with a resolution of 5 cm^{-1}. The results of μ-FT-IR were processed with Purency Microplastics Finder software, which provides statistical information on the number, size, and type of all microplastic particles trapped on the filter – Fig. 1.

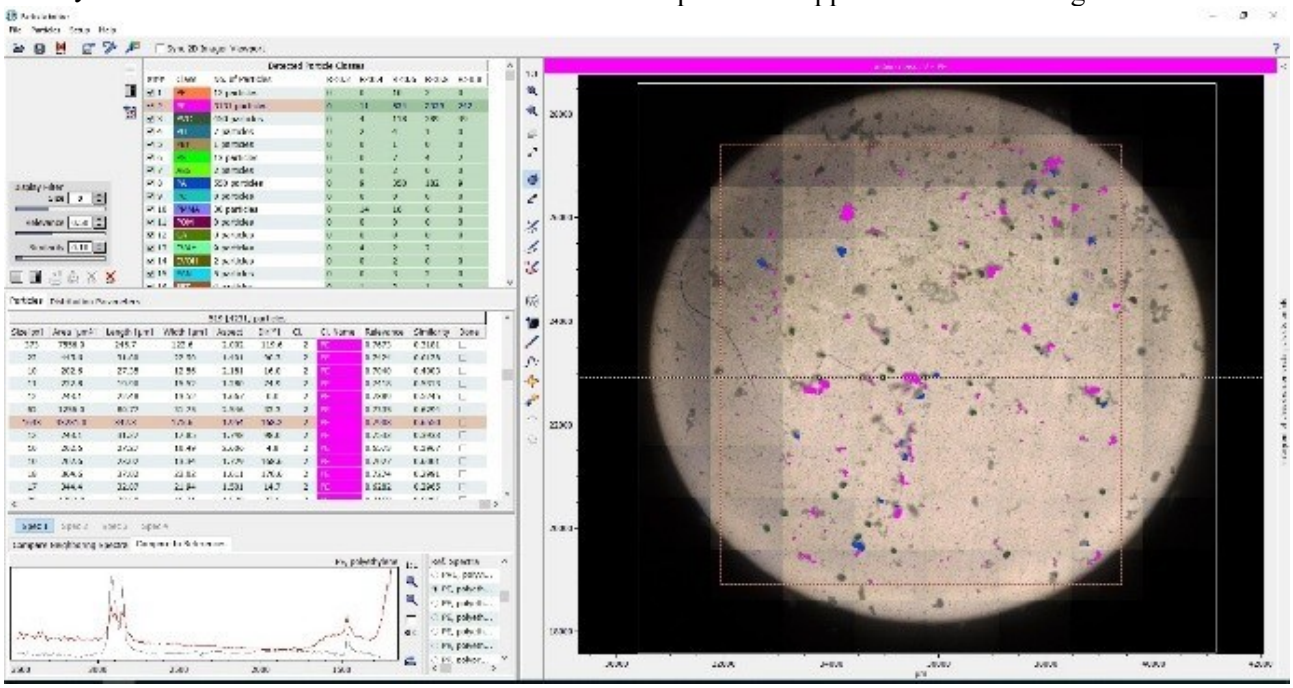

Fig. 1. Visualization of the μ-FT-IR results

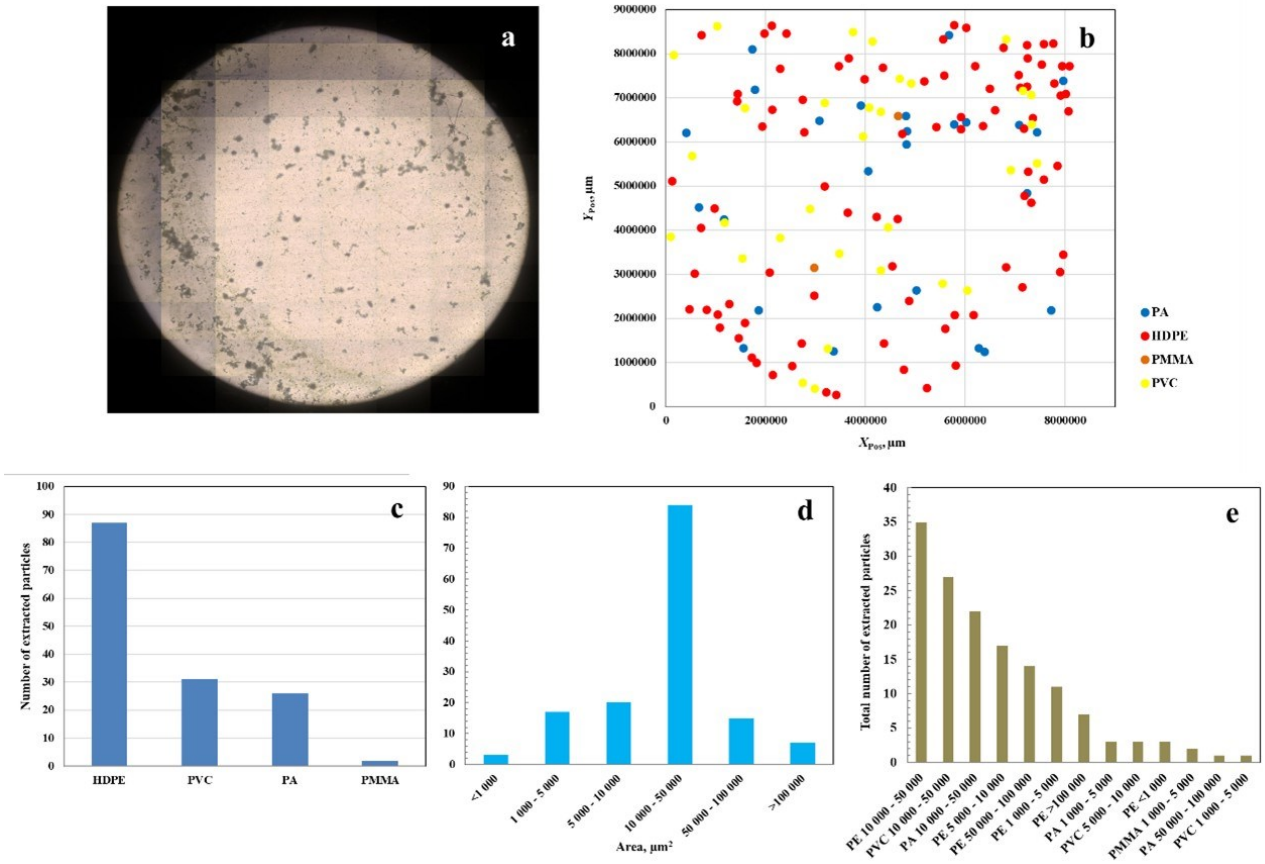

Fig. 2. Characteristics of the microplastic particles after extraction with NaCl: (a) microscopic image of the filter; (b) spatial distribution by polymer class; (c) distribution by polymer type; (d) distribution by area; (e) combined distribution by area and polymer type

The filters with the extracted MPs from the $CaCl_2$ extraction solution were further treated with ethyl alcohol due to the formation of a film on them, which makes it difficult to analyze with µ-FT-IR. The control sample, containing only purified sediment and ultrapure water, did not contain microplastics, confirming the effectiveness of the methodology in terms of avoiding external contamination.

RESULTS AND DISCUSSION

In this study, a detailed analysis of microplastic particles (HDPE, PVC, PA, PET and PMMA) extracted from pre-purified sediment using three salt solutions of different density (NaCl, $MgCl_2$, and $CaCl_2$) was performed. The µFT-IR data were analyzed in terms of the distribution of the total number of extracted particles from the respective extraction solution by the parameters: area, including polymer type and their combination (distribution of the total number of extracted particles by polymer type and area).

Analysis of microplastic particles extracted from NaCl solution

Figures 2 *a* and *b* present a microscopic image of the filter and the corresponding two-dimensional spatial distribution of the particles identified in the XY plane (in µm). Each point corresponds to the coordinates of a micropolymer particle on the filter, and the coloring shows the distribution of micropolymers by type. The type of all microplastic particles extracted from the sediment, based on the differences in their density and the NaCl solution, was determined with a µ-FT-IR imaging microscope and processed with Purency Microplastics Finder software. Possible areas with an increased concentration of the studied micropolymers were observed – Fig. 2 *b*. Spatially distributed throughout the filter are HDPE particles, followed by PVC and PA (evenly distributed, but fewer particles) and two single points of PMMA micropolymer particles.

After extraction of micropolymers from marine sediments from the Burgas Bay, Black Sea with NaCl solution, it was found that predominantly HDPE particles were extracted (87 pieces) – Fig. 2 *c*. This represents over half of all particles – 57%. PVC and PA particles were also successfully extracted, but in significantly smaller quantities – 31 and 26 pieces, respectively. PMMA – only 2 particles, and not a single extracted PET particle. The probable reason for the inability to effectively separate all types of plastic particles from NaCl

solution is its low density [9]. The insufficient density of the solution allows the extraction of polymers with low density (below 1.2 g/cm^3) [10], and denser polymers, in our case PET, are not extracted and/or are extracted poorly. This is in full accordance with the studies reported in the scientific literature, which determine NaCl as less effective compared to other salts [11–13].

The largest number of particles (about 85) falls in the range of 10 000 – 50 000 µm^2 – Fig. 2 *d*. There is a moderate amount of micropolymer particles from HDPE, PA, PMMA and PVC in the intervals of 1 000 – 10 000 and 50 000 – 100 000 µm^2. The smallest are particles with an area of <1 000 µm^2 and >100 000 µm^2. This means that the NaCl extraction process captures mostly medium-sized particles, which may be a limitation of the method. The absence of small-sized particles (below 1 000 µm^2) may lead to an incorrect determination of the total amount of microplastics in the sample, i.e., the method shows difficulty in extracting/identifying these particles and is probably not sensitive to them.

The combined plot of the total number of extracted NaCl particles by polymer type and area (Fig. 2 *e*) shows that HDPE particles with an area of 10 000 – 50 000 µm^2 (35 particles) predominate. The other significant groups are: PVC particles with an area of 10 000 – 50 000 µm^2 (27 particles) and PA with an area in the range of 10 000 – 50 000 µm^2 (22 particles). The smaller sizes, 1 000 – 5 000 µm^2 (PVC and PMMA), and the larger PA (50 000 – 100 000 µm^2) show a low presence of extracted particles, below 3 particles.

Analysis of microplastic particles extracted from $MgCl_2$ solution

Fig. 3 *b* shows the distribution of particles classified by chemical composition in the coordinate system (X_{Pos} – Y_{Pos}, µm). Analysis of the distribution of the polymers used in this study reveals areas of accumulation of microparticles with increased concentration (see Fig. 3 *a*) when a $MgCl_2$ solution is used to separate them from sediment samples.

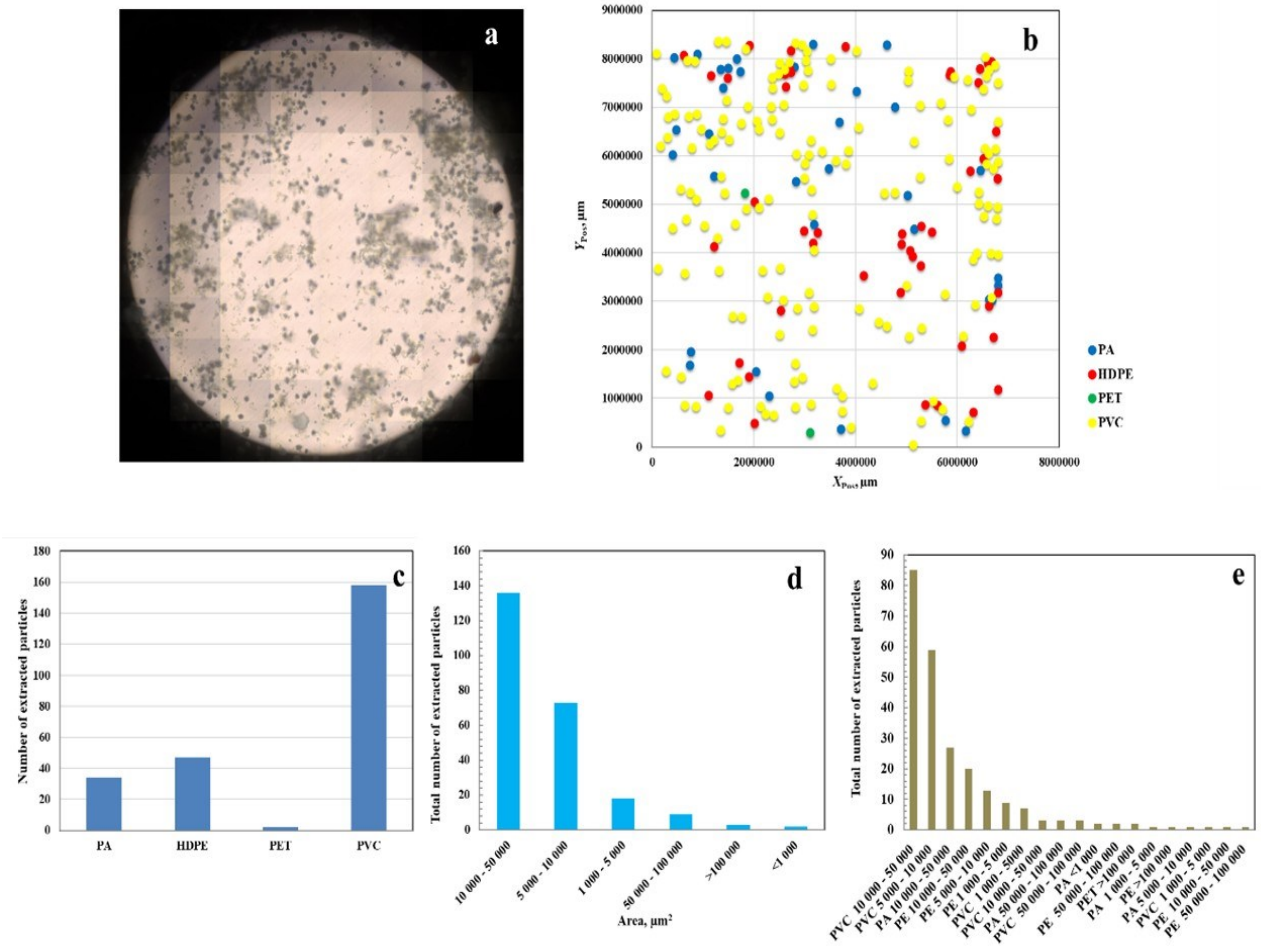

Fig. 3. Characteristics of the microplastic particles after extraction with $MgCl_2$: (a) microscopic image of the filter; (b) spatial distribution by polymer class; (c) distribution by polymer type; (d) distribution by area; (e) combined distribution by area and polymer type

When using a $MgCl_2$ solution to extract the added HDPE, PA, PET, PMMA and PVC particles to pre-purified sediment, 241 microplastic particles were identified. After classifying them by polymer type, it was found that the largest number of extracted PVC particles were: 158 particles, followed by HDPE - 47, PA - 34, PET only 2 particles and PMMA - 0 particles – Fig. 3 *c*. The dominance of PVC particles, which are denser than the others, suggests the effectiveness of the $MgCl_2$ solution. Since the density of the NaCl solution is lower than that of $MgCl_2$ [14], the latter proves to be suitable for density separation of microplastic particles from samples with a composition of HDPE, PA, PET and PVC, and could be a good alternative to more expensive and/or hazardous salts.

The following Fig. 3 *d* shows the distribution of the total number of extracted particles from the $MgCl_2$ solution by area. As can be seen, the majority of the total number of microplastic particles falls in the area range of 10 000 – 50 000 μm^2 (136 particles). The remaining particles can be grouped into the following categories: 5 000 – 10 000 μm^2 (73 particles), 1 000 – 5 000 μm^2 (18 particles), 50 000 – 100 000 μm^2 (9 particles), and >100 000 μm^2 (3 particles).

The combined plot of the distribution of the total number of extracted $MgCl_2$ particles by polymer type and area (Fig. 3 *e*) shows that PVC particles with an area of 10 000 – 50 000 μm^2 (85 particles) predominate. The other significant groups are: PVC particles with an area of 5 000 – 10 000 μm^2 (59 particles), PA with an area in the range of 10 000 – 50 000 μm^2 (27 particles) and HDPE, 10 000 – 50 000 μm^2 (20 particles).

Analysis of microplastic particles extracted from $CaCl_2$ solution

116 particles extracted from $CaCl_2$ solution were studied. The spatial distribution of the identified particles on the filter is shown in Fig. 4 *b*, and the image of the filter itself in Fig. 4 *a*. It can be seen that the distribution of the five types of polymers from the sediment samples contaminated with them is relatively more uniform and with fewer areas with accumulations of microparticles.

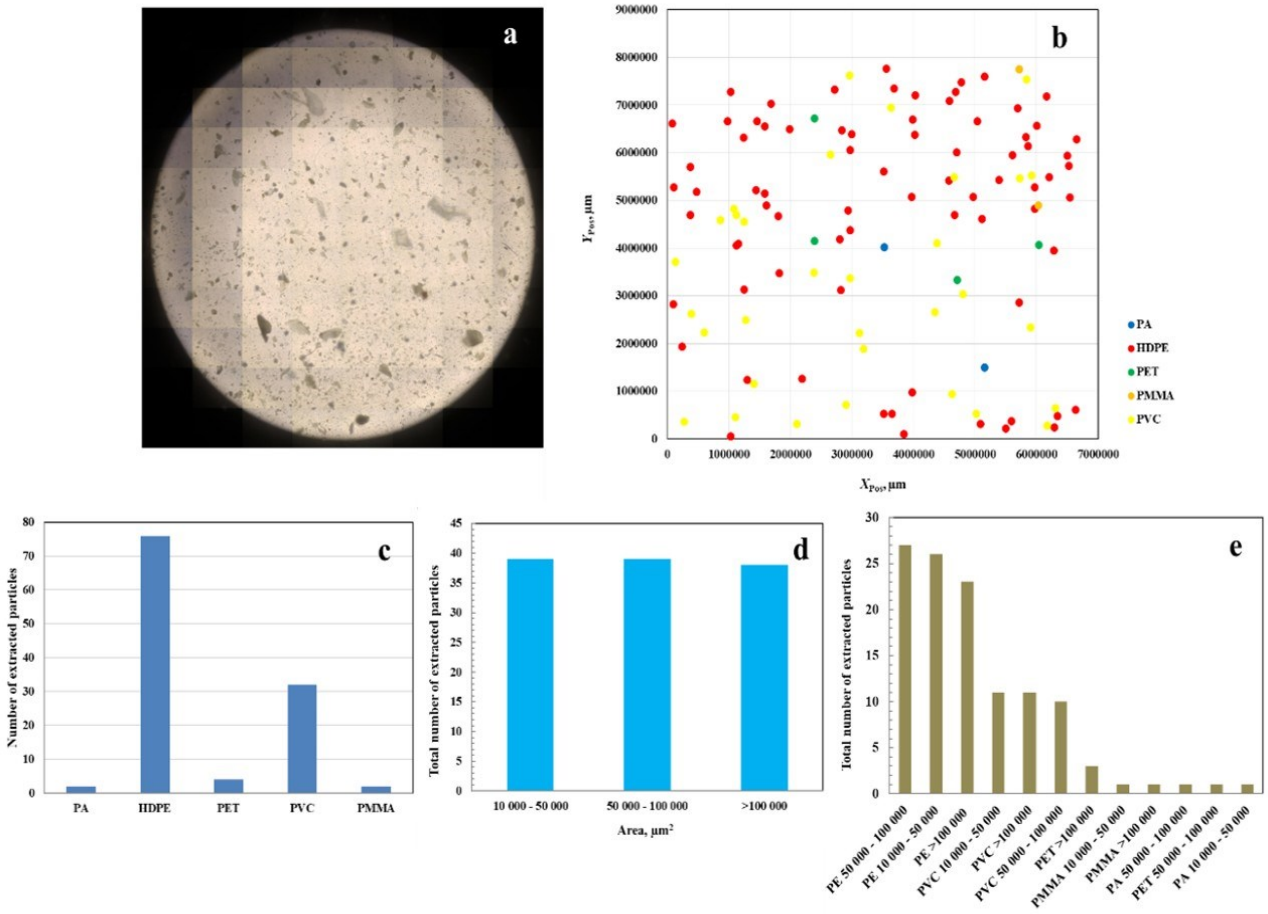

Fig. 4. Characteristics of the microplastic particles after extraction with $CaCl_2$: (a) microscopic image of the filter; (b) spatial distribution by polymer class; (c) distribution by polymer type; (d) distribution by area; (e) combined distribution by area and polymer type

Based on the summarized analysis of the particles, they are classified by polymer class (PA, HDPE, PET, PMMA, PVC), as well as by area. In the sediment sample extracted with $CaCl_2$, HDPE predominates with 76 particles (a little over 60%). This is followed by PVC with 32 particles (about 26), PET - 4 particles and with the lowest amount are PA and PMMA - only 2 particles of each were identified – Fig. 4 *c*.

From the dependence shown in Fig. 4 *d* it can be seen that the calcium chloride solution extracts micropolymer particles in three ranges of surface area: 10 000 – 50 000 μm^2, 50 000 – 100 000 μm^2 and >100 000 μm^2, with the number of particles being approximately the same. This is probably due to the additional treatment of the filter with ethyl alcohol, due to the formation of a film on it. Although the use of $CaCl_2$ for density separation has been reported [15, 16], since the density of the solution is 1.3 g/cm^3 [5], i.e. not much higher than that when using NaCl and/or $MgCl_2$, we believe that the extraction with $CaCl_2$ has limitations in this particular case.

The dependence in Fig. 4 *e* shows that the size distribution is relatively uniform, suggesting equal extraction efficiency and similar particle sizes. It was found that micropolymer particles of HDPE predominated in all sizes: 10 000 – 50 000 μm^2 (26 pieces), 50 000 – 100 000 μm^2 (27 pieces), and > 100 000 μm^2 (23 pieces). PVC particles were distributed in the above-mentioned area ranges as follows: 11, 10 and 11 pieces. The remaining polymers (PET, PMMA, PA) were present with 1 to 3 particles in each group.

CONCLUSIONS

The present study clearly demonstrates the influence of the extraction solution on the amount and type of extracted particles. The results obtained show that, due to its higher density, $MgCl_2$ is the most effective extraction solution for both a larger number and a variety of microplastic particles with different densities, including denser ones such as PVC and PET in a wide range of sizes, including fractions with an area below 10 000 μm^2. On the other hand, NaCl shows limited sensitivity to smaller particles and is ineffective for denser polymers (no PET particles were extracted). $CaCl_2$ demonstrates a uniform particle size distribution but significantly limited particle extraction in number, which suggests some selectivity in order to draw definitive conclusions about its effectiveness. Particles of polyethylene, polyvinyl chloride and polyamide are extracted to the greatest extent, with prevailing particles with an area in the range of 10 000 – 50 000 μm^2. The presence of particles with an area below 1 000 μm^2 is weakly expressed in extraction with all the mentioned salt solutions, suggesting a possible underestimation of the total level of microplastic pollution, especially when using NaCl and $CaCl_2$. The obtained data highlight the need to use combined or improved extraction methods that ensure the capture of a wide range of sizes and types of microplastics. The use of $MgCl_2$ shows potential as a more reliable approach for quantitative and qualitative analysis of microplastic pollution in marine sediment.

Acknowledgement: *This research was funded by the Bulgarian National Science Fund under the contract KP-06-H89/4 „Investigation of the content of micropolymers in sediment and biota from a marine ecosystem”.*

REFERENCES

1. L. Simon-Sánchez, M. Grelaud, M. Franci, P. Ziveri, Environ. *Pollut*., **292**, 118275 (2022).
2. A. Bellasi, G. Binda, A. Pozzi, G. Boldrocchi, R. Bettinetti, *Chemosphere*, **278**, 130357 (2021).
3. D. He, X. Zhang, J Hu, *J. Hazard. Mater*., **409**, 124640 (2021).
4. D. Debraj, M. Lavanya, *Sci. Total Environ*., **893**, 164878 (2023).
5. M. Rani, S. Ducoli, L.E. Depero, M. Prica, A. Tubić, Z. Ademovic, L. Morrison, S. Federici, *Molecules*, **28**, 5710 (2023).
6. S. Canensi, G. Barucca, C. Corinaldesi, *Front. Mar. Sci*., **9**, 975875 (2022).
7. M. Bergmann, L. Gutow, M. Klages, Marine anthropogenic litter, Springer Nature, 2015, p. 447.
8. J. Li, H. Liu, J.P. Chen, *Water Res*., **137**, 362 (2018).
9. M.A. Cashman, K.T. Ho, T.B. Boving, S. Russo, S. Robinson, R.M. Burgess, *Mar. Pollut. Bull*., **159**, 111507 (2020).
10. M. Constant, G. Billon, N. Breton, C. Alary, J. Hazard. Mater., 420, 126571 (2021).
11. X. Han, X. Lu, R.D. Vogt, *Environ. Pollut.,* **254**, 113009 (2019).
12. W. Li, R. Wufuer, J. Duo, S. Wang, Y. Luo, D. Zhang, X. Pan, *Sci. Total Environ*., **749**, 141420 (2020).
13. X. Zhang, K. Yu, H. Zhang, Y. Liu, J. He, X. Liu, J. Jiang, *Chemosphere*, **256**, 127039 (2020).
14. L. Cutroneo, A. Reboa, I. Geneselli, M. Capello, *Mar. Pollut. Bull*., **166**, 112216 (2021).
15. M.E.L. Felismino, P.A. Helm, C.M. Rochman, *J. Great Lakes Res*., **47**, 180 (2021).
16. A. Stolte, S. Forster, G. Gerdts, H. Schubert, *Mar. Pollut. Bull*., **99**, 216 (2015).

Bulgarian Chemical Communications, Volume 58, Special Issue A (pp. 22-25) 2026 DOI: 10.34049/bcc.58.A.SN-04

Chemical and biophysiological processes accompanying patients with obstructive sleep apnea syndrome (OSAS) in group therapies at St. Anna Hospice

S. Petkova-Georgieva*

Burgas State University "Prof. Dr. Assen Zlatarov", Burgas, 8000, Bulgaria

Received: August 20, 2025; Revised: November 07, 2026

The study included 200 patients with obstructive sleep apnea syndrome (OSAS) (164 men and 36 women), who were undergoing a three-month group therapy program through cardiac rehabilitation (CR) at a specialized medical facility – St. Anna Hospice. Daily performed blood tests showed that the improvement in the patients' condition (over 40%) is due to a decrease in the level of total cholesterol through the activation of chemical and biophysiological processes during group rehabilitation. The planned volume of laboratory testing included analysis of the blood lipid spectrum, liver transaminases, CPK, glycemia, potassium, creatinine, and, according to indications, uric acid level, and glycosylated hemoglobin.

Keywords: sleep, apnea, cholesterol $C_{27}H_{46}O$

INTRODUCTION

The activation of chemical and biophysiological processes in the blood of patients with obstructive sleep apnea syndrome (OSAS) [4] by including them in group therapies with cardiology programs leads to over 40% improvement in their condition. The present study was conducted among 200 patients who were treated at a specialized medical facility, St. Anna Hospice. The laboratory testing included analysis of the blood lipid spectrum, liver transaminases, CPK, glycemia, potassium, creatinine, and, according to indications, uric acid level, and glycosylated hemoglobin.

METHODOLOGY, EXPERIMENTAL, CASE, FINDINGS

People having sleep apnea briefly stop breathing during sleep. Their brain tries to protect them by waking them up frequently, but this in turn interferes with restful, healthy sleep. The condition is chronic, over time it can cause serious, life-threatening complications related to the cardiovascular system and is a reason for a person to seek medical attention. In about 40% of the patient cases studied at St. Anna Hospice, sleep apnea was accompanied by arterial hypertension. There are two main types of the disease – obstructive and central. In both conditions, improvement was observed as a result of group therapies to lower cholesterol levels.

Obstructive sleep apnea is the more common form that successfully responds to group therapy to lower cholesterol. The treatment is combined with sports group training. Special devices are also used that are worn during sleep and with which patients are able to achieve optimal benefits for a wide range of diseases, including those of the cardiovascular system [2].

Sleep apnea can affect people of any age and is one of the modern diseases. The disease itself causes complications similar to those of obesity and diabetes. Therefore, group sports therapies for patients at St. Anna Hospice were primarily focused on lowering the cholesterol level in order to alleviate the symptoms of obstructive sleep apnea. Before the age of 50, the disease is more common in men. After this age, its prevalence in both sexes becomes equal.

The symptoms include:

• *Feeling tired or exhausted upon waking*. Even after 8 hours of sleep, patients with sleep apnea usually feel extremely tired;

• *Daytime sleepiness*. In more severe cases, this can cause drowsiness while driving, working, or other activities;

• *Snoring.* This is a common feature of sleep apnea (but it is not something that happens in all cases). A person can have sleep apnea without ever snoring;

• *Multiple awakenings* during the night or multiple urinations for men, which they usually mistake for a prostate problem;

• *Headache* immediately after waking up;

• *Sweating* in the neck area.

* To whom all correspondence should be sent:
E-mail: *s.p.petkova@gmail.com*

Among the most dangerous consequences of sleep apnea are heart damage and heart failure. Apnea is often the cause of arrhythmias and atrial fibrillation, which can lead to sudden cardiac arrest. Although not as dramatic as a condition, daytime sleepiness can also be potentially very dangerous, especially if a person's profession involves driving or operating dangerous machinery. Therefore, sports group therapy has benefits for both lowering cholesterol and maintaining patients' alertness.

To assess the effect of group therapy on patients at the St. Anna Hospice, an assessment of their quality of life after lowering cholesterol was applied using the QALY methodology [1].

All patients were previously consulted by a psychologist upon inclusion. During the observation, repeated consultations with a psychologist, psychocorrection using cognitive-behavioral and relaxation techniques, consultations with a psychotherapist, and individual psychotherapy according to indications were conducted. The initial psychodiagnostic examination was performed on 200 patients of the St. Anna Hospice 1 month after therapy, and then annually, according to the following methods:

1. SF-36 - quality of life assessment;
2. TOBOL methodology;
3. Zung depression scale;
4. IAT - integrative anxiety test;
5. E. Khaim's method for assessing disease coping strategies.

The TOBOL methodology is built in the form of a questionnaire that diagnoses the type of attitude towards the disease, based on information on how the patient relates to a number of life problems and situations that are potentially most important to him and are directly or indirectly related to his disease. The relationships of patients are examined through 12 subsystems, forming a common system of personal relationships [3]. These subsystems structure the content of the methodology under 12 topics: attitude towards the disease, towards its treatment, towards doctors and medical staff, towards relatives and loved ones, environment, work (study), loneliness, future, as well as self-assessment of self-esteem, mood, sleep and appetite.

To determine the value of a year of life in different health states, the utility (or strength of preference) of the treatment method for the patient is established. One year of life with its absolute quality has a QALY value of 1, and one year of life with lower quality has a QALY value of less than 1. One of the most common methods for assessing quality of life is the SF-36 questionnaire (The Short Form-36), which rates various aspects of a patient's life functioning on a scale of 1 to 100: physical (general assessment of physical functioning, role functioning that is determined by physical condition, pain intensity, general health status) and psychological (vital activity, social functioning, role functioning, which is determined by the emotional state, mental health). According to the study Percutaneous (PET) coronary angioplasty compared with exercise training in patients with stable coronary artery disease, the use of physical exercise in patients with OSAS is associated with a reduced risk of death, cardiac arrhythmias and is significantly more effective.

RESULTS AND DISCUSSION

The planned volume of laboratory testing included analysis of the blood lipid spectrum, liver transaminases, CPK, glycemia, potassium, creatinine, and, according to indications, uric acid level, and glycosylated hemoglobin. Signs of left ventricular myocardial hypertrophy were found in 154 (77%) patients, the mean myocardial mass index was 120.1 ± 15.3 g/m, diastolic dysfunction - in 80 (40%), reduced systolic myocardial function <50% according to Simpson - in 28 (14%), and areas of impaired local contractility were registered in 74 (37%) of the studied patients. None of the patients had an improvement in OSAS below 40%. All patients were previously consulted by a psychologist upon inclusion. During the observation, repeated consultations with a psychologist, psychocorrection using cognitive-behavioral and relaxation techniques, consultations with a psychotherapist, and individual psychotherapy according to indications were conducted.

The studied activations of chemical and biochemical processes in the patients' blood tests clearly showed that one of the causes of OSAS is the high cholesterol content in the body. The human body can synthesize up to 80% of the cholesterol it needs (Fig. 1).

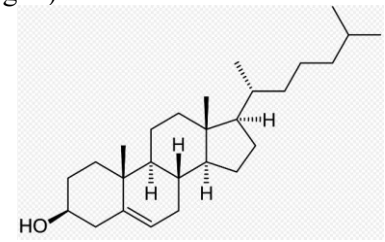

Figure 1. Cholesterol's structure. $C_{27}H_{46}O$

Normal synthesis is about 10 mg of cholesterol per day per 1 kg of body weight. Newly

synthesized cholesterol, as well as that taken in with food, enters the liver. There, cholesterol binds to special transport proteins in low-density lipoprotein complexes (low density lipoproteins – cholesterol, LDL-C, called "bad cholesterol"). LDL-C carries cholesterol to all cells and tissues of the human body.

Criteria for inclusion of patients in the study:

1. The patient's signed informed consent.
2. Patients with obstructive sleep apnea syndrome (OSAS) (164 men and 36 women) and high cholesterol $C_{27}H_{46}O$.

Criteria for excluding patients from the study:

1. Concomitant pathology that affects the patient's immediate prognosis;
2. Concomitant diseases that would prevent physical activity (consequences of stroke, diseases of the musculoskeletal system);
3. Surgical revascularization that was done as an emergency.

The clinical characteristics of the patients when included in the study are presented in Table 1. The majority of patients (164 persons - 82%) suffered from anginal stenosis of functional class III and IV (FC) at the time of sport group therapy. 36% of the patients (72 persons) were regularly seen by a doctor, the average frequency of visits to a cardiologist was 4.1 ± 1.7 (from 1 to 8) times per year; the majority (55%) of all doctor visits were made 3-6 months before hospitalization at St. Anna Hospice and were determined by the preoperative examination and the preparation of the necessary documents.

In the US and most developed countries, a degree of intervention effectiveness has been developed:

- treatment that costs <20 000 $/QALY, is cost-effective;
- medical expenses from $ 20 000/QALY to $ 40 000/QALY are considered as acceptable;
- medical expenses from $ 40 000/QALY to $ 60 000/QALY are on the border;
- treatment that costs > 60 000 $/QALY are considered as expensive;
- over 100 000 USD/QALY are considered as an unacceptable.

The present study was cost-effective because the costs of the group therapy for patients with OSAS were less than $20,000.

Over a period of 4 years of specialized sports group therapies for patients with OSAS, their blood tests showed a reduction in cholesterol $C_{27}H_{46}O$ by over 88%. As a result, in all 200 cases, complete remission of OSAS was achieved.

To reduce direct and indirect costs for contact patients with OSAS, it was necessary to be careful and precise in choosing an effective treatment approach. It is recommended to individually prescribe appropriate treatment for each patient, which should be combined with group sports activities to reduce cholesterol levels.

The clinical characteristics of the patients included in the study are presented in Table 1.

Table 1. Clinical characteristics of patients included in the study, n = 200 patients.

Clinical features	Indicator values
Age of patients	
< 45 years	10 (5%)
45 ÷59 years	110 (55%)
≥ 60 years	80 (40%)
Duration of OSAS during group therapies, years (M ± s)	4.5±3.7
OSAS - obstructive sleep apnea syndrome, patients	200 (100%)
Angina pectoris, patients including	196 (98%)
II FC	32 (16%)
III FC	98 (49%)
IV FC	66 (33%)
Painless myocardial ischemia, patients	12 (6%)
Myocardial infarction with history, patients	128 (64%)
Heart failure, patients including	168 (84%)
II FC	26 (13%)
III FC	120 (60%)
IV FC	22 (11%)
History of myocardial revascularization (PCI), patients	24 (12.0%)
Arterial hypertension, patients	184 (92%)
Stroke with history, patients	10 (5%)
Active smokers, patients	70 (35%)
Former smokers, patients	56 (28%)
Diabetes mellitus, type 2, patients	52 (26%)
Overweight (25>BMI<30 kg/m^2), patients	200 (100%)
Obesity (BMI> 30 kg/m^2), patients	190 (95%)
Heredity for CVD, patients	30 (65%)

Legend: OSAS - obstructive sleep apnea syndrome; FC - functional class; PCI - percutaneous coronary intervention; BMI - body mass index; CVD - cardiovascular diseases

The whole process is even more effective when each patient is educated about how they should change their daily routine to add years of quality life. When patients are hospitalized in a hospice (like the study group at St. Anne's Hospice), the

desired outcome can be achieved much more effectively, because patients receive 24/7 medical care [5]. The public health challenge is related to ensuring access to sleep medicine care. The field is suffering from a small number of specialists, incomparable to the large number of patients with sleep disorders.

CONCLUSIONS

After examining the data obtained, it can be concluded that the misperception of sleep is likely influenced by various psychological, cognitive and physiological factors. For example, dynamic physiological processes [7], alpha-delta sleep [6] (but not all studies have found a connection with alpha-delta sleep [8]), cyclic sleep pattern [9], REM or slow-wave sleep content [10], high cholesterol levels [2], and personality traits [11] are associated with sleep misperception.

Blood tests of the chemical and biophysiological processes that are activated as a result of rehabilitation group therapies in patients with OSAS show that by lowering the level of the so-called bad cholesterol, the human body manages to improve its quality of life (QALY) by over 40%, despite this disease. This is a significant achievement for the medical team of St. Anna Hospice, which is motivated to improve results in the future. This publication publicizes the research on the chemical and biophysiological processes accompanying patients with obstructive sleep apnea syndrome (OSAS) during group therapies at the St. Anna Hospice.

REFERENCES

1. E. Altena, C. Baglioni, C.A. Espie, J. Ellis, D. Gavriloff, B. Holzinger et al., *J. Sleep. Res*., **XXIX** (4), 1 (2020).
2. S. Bogoslovov, *Annual of Assen Zlatarov University, Burgas, Bulgaria***, LIII** (2), 67 (2024).
3. S. Bogoslovov, Improving the management of geriatric care in hospice by using the capabilities of artificial intelligence, monograph, Assen Zlatarov University press, Burgas, Bulgaria, 2024. ISBN 978-619-7559-63-7
4. S. Bogoslovov, *Pedagogy*, **XCVIII,** 36 (2026).
5. R.D. Chervin, D.L. Murman, B.A. Malow et al., *Ann. Intern. Med.* **CXXX** (6), 496 (2023).
6. Il. Darien, International classification of sleep disorders, American Academy of Sleep Medicine, 3rd edn., 2014.
7. A. Mamede, I. Merkelbach, G. Noordzij, S. Denktas, *Front Psychol.,* **XIII**, 1 (2022).
8. R. Mirchandaney, R. Barete, L.D. Asarnow, *Curr. Psychiatr. Rep*., **XXIV** (2), 121 (2022).
9. J.B. Pietzsch, A. Garner, L.E. Cipriano, et al., *Sleep,* **XXXIV** (6), 695 (2021).
10. M. Sforza, A. Galbiati, M. Zucconi, F. Casoni, M. Hensley, L. Ferini-Strambi, et al., *J. Affect. Disord*. **CCLXXXIX**, 117 (2021).
11. R.J. Walter, S.I. Hagedorn, C.J. Lettieri, *Sleep Med*., **XXXVIII**, 73 (2023).

Bulgarian Chemical Communications, Volume 58, Special Issue A (pp. 26-30) 2026 DOI: 10.34049/bcc.58.A.SN-05

Direct synthesis of graphene by using combined electrolysis and ultrasonic methods

D. Georgiev, I. Markovska, F. Yovkova*, S. Kozarev

Burgas State University "Prof. Dr. Assen Zlatarov", 1 Prof. Yakimov Blvd., Burgas, 8010, Bulgaria

Received: July 02, 2025; Revised: November 26, 2025

Graphene is a novel nanomaterial that possesses many amazing characteristics. It is considered as a next-generation conductive material with the potential to be used for obtaining of electrodes for supercapacitors. In the present paper, monolayer graphene was synthesized through simultaneous application of electrolysis and ultrasound. High-purity finely dispersed graphite was used as a precursor. Graphene was obtained *via* a combination of chemical and physical treatment, with sulfuric acid serving as the electrolyte. The acid loosens the weak van der Waals bonds, and together with the acoustic action of ultrasound, contributes to the cleavage of the individual graphene layers.

Keywords: Graphene, Ultrasound, Electrolysis

INTRODUCTION

Graphene is a two-dimensional atomic-scale material made of a single layer of carbon atoms. The latter have a high level of cohesion through hybridization bonds sp^2 and are arranged in a uniform surface, slightly undulating, with appearance similar to a honeycomb lattice because of its hexagonal configuration [1]. Graphene is an allotropic form of carbon, as graphite or diamond. One millimeter of graphite contains three million layers of graphene [1]. This is the first stand-alone material with a 2D structure, which has unique properties. These properties make it extremely interesting both for basic science and in applied aspect. Until recently, it was thought that planar graphene could not exist in the free state because it was unstable with respect to the formation of curved structures such as soot, fullerenes, and nanotubes [2-4].

Graphene possesses many amazing characteristics. Its electron mobility is 100 times faster than that of silicon. Graphene conducts heat 2 times better than diamond; at the same time its electrical conductivity is 13 times better compared to copper. This material absorbs only 2.3% of reflected light; it is impervious so that even the smallest atom (helium) can't pass through a defect-free monolayer graphene sheet [5].

Graphene is obtained from graphite by separating the planar networks that form the hexagonal crystal lattice of graphite. Actually, graphite consists of many flat layers of graphene sheets (Fig. 1 a, b).

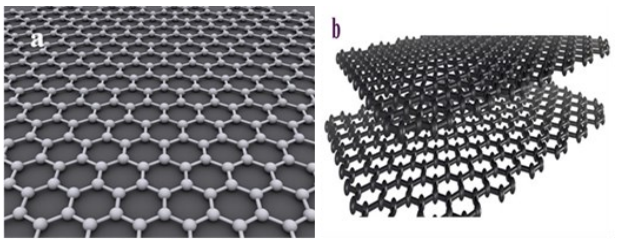

Fig. 1. Single-layer (a) and double-layer (b) structure of graphene.

There are various methods to synthesize graphene and its derivatives. Effective ways for detachment of graphene planes are by high-voltage discharge, or by electron beam or laser sputtering in helium medium [6, 7].

The main methods of graphene preparation are: mechanical exfoliation, chemical exfoliation, CVD (chemical vapor deposition), epitaxial growth, pyrolysis, etc. [8-12]. Hummers' method [13] was developed in 1958 as a faster and more efficient method of preparation of graphitic oxide. In recent years many teams are looking into ways of using graphitic oxide as a precursor to mass production of graphene.

The main difficulties in graphene preparation are related to the fact that it is quite difficult to obtain a significant amount of high-quality sample. The method of Novoselov (micromechanical exfoliation of graphite layers) gives neither high-quality product, nor high yield. It is necessary to overcome the energy of van der Waals interactions between the layers without disrupting the first, second and the other layers below, which is very difficult.

Graphene offers many opportunities for electronics [14-19]. At present, graphene is extensively studied with a view to its use in the

* To whom all correspondence should be sent:
E-mail: *fila_03@abv.bg*

production of supercapacitors able to be quickly charged and store higher amounts of electric energy [14, 15]. Lithium-ion batteries improved with graphene can be used in electricity-driven vehicles, as well as in smartphones, laptops and tablets with significantly smaller weight [16]. Intense efforts are devoted to the development of graphene sensors (gas, bio and light) [19]. In this respect, the present paper reports for preparation of graphene from high-purity finely dispersed graphite by simultaneously applying electrolysis and ultrasound. Graphene was obtained *via* a combination of chemical and physical treatments, with sulfuric acid serving as the electrolyte. The acid weakens the van der Waals interactions, and together with the ultrasonic acoustic effects, facilitates the exfoliation of individual graphene layers.

EXPERIMENTAL

Materials

High-purity (99.9%) finely dispersed graphite (GO) was used as a precursor for graphene synthesis. The particle size of the graphite powder was below 200 μm. The electrical resistance of pristine graphite was 11×10^{-8} Ω m. Sulfuric acid (H_2SO_4), potassium hydroxide (KOH) and deionized water were also used (Fig. 2).

Fig. 2. Initial graphite powder

Methods

The obtained graphene was mainly characterized using Raman spectroscopy and Fourier transform infrared (FT-IR) spectroscopy.

- *Raman spectroscopy.* The Raman spectra were obtained using LabRAM HR Visible Raman spectrometer. For excitation the 633 nm line of a He-Ne laser was used. To decrease the possible local overheating, the used laser power on the sample surface was reduced to 360 μW. An objective X50 was used both to focus the incident laser light and to collect the scattered light in backscattering geometry. The diameter of the laser spot on the sample surface was about 3 μm. At least three spectra at different arbitrary chosen spots from each sample were collected. The investigated spectral range was 900 cm^{-1} ÷3500 cm^{-1}. The most intense lines in the spectra (namely, D, G, D' and 2D) were fitted with Lorentzians and the line parameters (as well the intensity line ratios) were calculated.

The method used in the present work involves simultaneous application of ultrasound and electrolysis. Finely ground graphite (> 99%) which burns without residue was used as a precursor for the synthesis of graphene. In a beaker, 200 ml deionized water were placed, then 8 ml of 4N H_2SO_4 and 5 g of pure finely dispersed graphite G0 were added and the mixture was well homogenized. The beaker with the sample was placed in an ultrasonic bath filled about 2/3 with deionized water (Fig. 3).

Fig. 3. Experimental setup for combined ultrasonic treatment and electrolysis.

The experiment was carried out in the ultrasonic bath at room temperature for 4 h. In our case, the sulfuric acid plays the role of a liquid medium for propagation of the acoustic waves while, according to the literature review, the media used for this purpose by other authors were ethyl alcohol, acetone, heptane and other liquids.

Table 1 shows the compositions synthesized and the experimental conditions.

Table 1. Compositions synthesized and experimental conditions

Sample №	G_0, g	4N H_2SO_4, ml	H_2O, ml	Electrolysis, min	Ultrasound, min	Current magnitude, A	Voltage, V
GE1	5	8	200	5	30	1	5.6
GE2	5	8	200	10	30	1	5.6
GE3	5	8	200	15	30	1	5.6
GE4	5	8	200	5	30	3.1	10.6
GE5	5	8	200	30	30	3.1	10.6

Electrolysis and ultrasound were simultaneously applied. Fig. 3 shows a picture of the experimental installation with combined application of ultrasound and electrolysis.

Graphite electrodes were placed in a beaker (Fig. 4). For samples GE1, GE2 and GE3, the electrodes were plate-shaped while for samples GE4 and GE5 they were cylindrical. The distance between the electrodes was 10 mm.

Fig. 4. Photograph of the experimental layout for carrying out the electrolysis

The electrolysis and the ultrasonic treatment took place simultaneously. The experiments were carried out at a temperature of 17 – 30°C and ultrasound frequency of 40 kHz. The samples were then filtered and the solid residue was dried at 110°C for 5 h.

The electrolyte used was an aqueous solution of H_2SO_4. Sulfuric acid dissociates according to the equation: $H_2SO_4 \rightarrow 2H^+ + SO_4^{2-}$. By the application of electric field in the electrolyte, the positive ion H^+ was deposited on the cathode while the negative one SO_4^{2-} – on the anode. The following primary processes took place on the cathode and on the anode:

- on the cathode: $2H^+ + 2e^- = H_2\uparrow$
- on the anode: $SO_4^{2-} - 2e^- = SO_4$

The neutral radical SO_4 is extremely active and cannot exist in free state. It reacts with water and a secondary reaction occurs on the anode:

$$2SO_4 + 2H_2O = 2\,H_2SO_4 + O_2\uparrow$$

As a result, one molecule of sulfuric acid has returned to the solution and one molecule of water has released oxygen on the anode and hydrogen on the cathode.

RESULTS AND DISCUSSION

Characteristics of graphene

- *Raman spectroscopy*

Raman spectroscopy was used to obtain structural information of the prepared graphene. Fig. 5 shows the Raman spectrum of sample GE1 where the major peaks of graphene can be observed. The carbon material displays distinctive Raman peaks known as D-, G- and 2D-peaks at approximately 1350, 1580 and 2700 cm^{-1}, respectively [20]. In our case (Fig. 5) these lines are at 1337, 1578 and 2669 cm^{-1}, respectively. The intensity ratio of 2D-peak to G-peak (I_{2D} /I_G) can be used to evaluate the quality of graphene. A large I_{2D} /I_G and insignificant D-peak indicate the high quality of graphene [21].

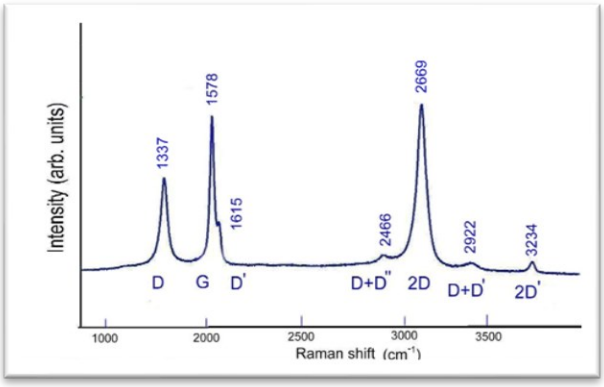

Fig. 5. Raman spectrum of sample GE1

As shown in Fig. 5, the spectrum of sample GE1 has all characteristic peaks of graphene, such as D, G, 2D and D+G bands. Only lines, typical for the graphene-like samples, are visible. The sample GE1 has I_{2D}/I_G ratio > 1 and the smallest width of the lines, so it can be characterized as a sample of high-quality graphene. For comparison, in Fig. 6 the Raman spectra of pure graphene according to Calizo *et al.* [22] (a) and Wang *et al.* [23] (b) are given.

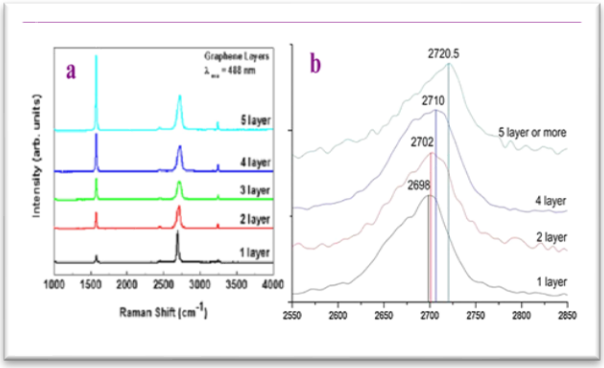

Fig. 6. Raman spectra of graphene according to: a) Calizo *et al.* [22] and b) Wang *et al.* [23]

It is known that the frequency shift and the shape change of the Raman peak at the 2D band can be used to distinguish the number of layers in graphene samples [23, 24]. Comparing our result from Fig. 5 with the literature data presented in Fig. 6 it can be seen that the spectra obtained by us correspond to monolayer graphene. In our samples, therefore, using the change in the shape and frequency of the 2D band peak located at 2669 cm^{-1} shown in Fig. 5, we can identify sheets consisting of a single layer

and two layers of graphene, according to Calizo *et al.* [22] and Wang *et al.* [23].

- *Infrared spectroscopy (FT-IR)*

Fourier transform infrared (FT-IR) spectra provide information about the functional groups in a sample. FT-IR spectra of samples GE3, GE4 and GE5 are shown in Fig. 7.

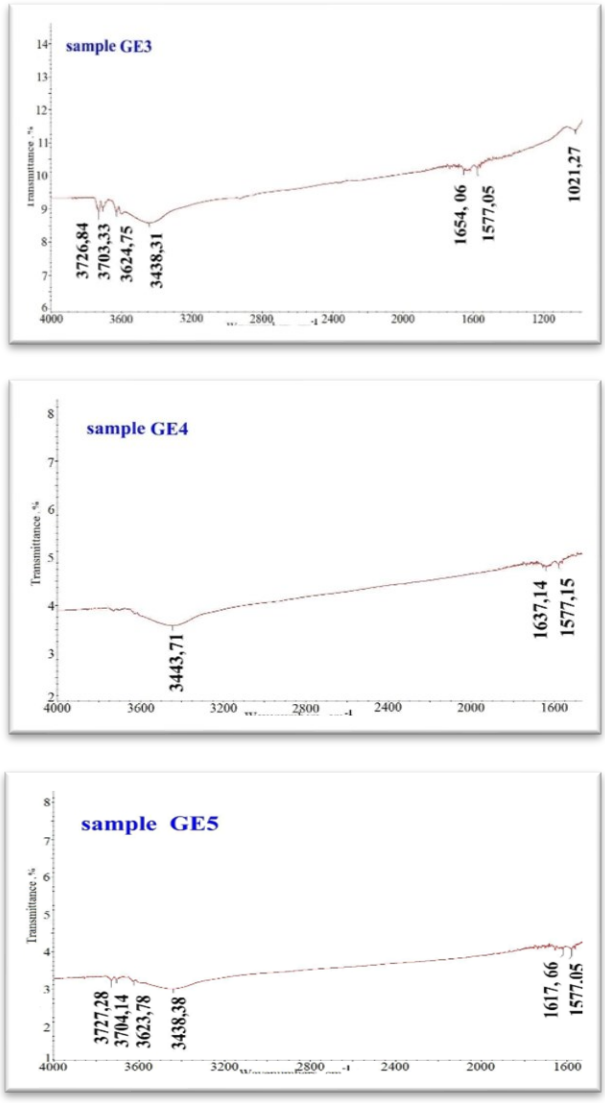

Fig. 7. IR spectra of samples GE3, GE4 and GE5

The FT-IR spectrum of sample GE3 displays absorption bands at 3726.84 cm^{-1}, 3703.33 cm^{-1}, 3624.75 cm^{-1}, 3438.31 cm^{-1}, 1654. 06 cm^{-1}, 1577.05 cm^{-1} and 1021.27 cm^{-1}. The FT-IR spectrum of sample GE4 displays absorption bands at 3443.71 cm^{-1}, 1637.14 cm^{-1} and 1577.15 cm^{-1}. The FT-IR spectrum of sample GE5 displays absorption bands at 3727.28 cm^{-1}, 3704.14 cm^{-1}, 3623.78 cm^{-1}, 3438.38 cm^{-1}, 1617, 66 cm^{-1}, 1577.05 cm^{-1}.

The results obtained from the FT-IR spectra shown in Fig. 7 indicate the presence of large peaks for all samples around 3400 – 3440 cm^{-1} corresponding to O–H vibrations.

The FT-IR spectra of samples GE3 and GE5 display absorption bands in the range of 3800 to 3600 cm^{-1} due to O-H stretching and hydrogen-bonded OH.

The absorption bands with maxima at 1654.06 cm^{-1}, 1637.14 cm^{-1} and 1617.66 cm^{-1} are characteristic of the O–H stretching of adsorbed water, as well as for skeletal vibrations from the rest which did not react graphitic domain. The vibrations can be attributed to the C=C bond**.** The peak around 1550 cm^{-1} is characteristic of the graphene double bond (ν C = C) [25]. In our case it is observed at 1577.05 cm^{-1} (for GE3), 1577.15 cm^{-1} (for GE4) and 1577.05 cm^{-1} (for GE5). The new observed band at 1021.27 cm^{-1} can be assigned to the symmetric and asymmetric stretching modes of $–SO_3H$ functional groups and demonstrates the presence of sulfonic acid groups in sample GE3, as a result of pre-treatment of the graphite precursor with sulfuric acid [25–28].

The simplest spectrum observed was that for sample GE4. For sample GE4, the electrolysis was carried out for 5 min, for GE3 – for 15 min and for GE5 – for 30 min (Table 1). The results presented in Fig. 7 indicate that the duration of electrolysis has a major effect on bond formation. For the sample with the shortest duration of electrolysis (GE4), the smallest amounts of side bonds, as well as interaction with radicals from the dissolution of the "solvent" H_2SO_4. were observed.

CONCLUSIONS

Profound studies were carried out on the synthesis of a new nanomaterial – graphene by using combined electrolysis and ultrasonic methods. Our particular contribution can be described as follows:

- A combination of chemical and physical impacts on graphite as a precursor (> 99%) was applied for the preparation of graphene.
- Raman spectra proved that monolayer graphene was synthesized.
- The results obtained from the IR spectra indicated that the duration of electrolysis has a major effect on bond formation. For the sample with the shortest duration of electrolysis (GE4), the smallest amounts of side bonds were observed.
- The present work shows that high-quality graphene samples can be obtained by an inexpensive and easily scalable electrochemical process.

REFERENCES

1. https://www.graphenano.com/en/what-is-graphene/
2. A. Geim, K. Novoselov, *Nature Mater.*, **6**, 183 (2007).

3. V. Mohan, K. Lau, D. Hui, D. Bhattacharyya, *Composites Part B,* **142**, 200 (2018).
4. A. Neto, F. Guinea, N. Peres, *Phys World*, **19** (11), 33 (2006).
5. https://www.nanowerk.com/what_is_graphene.php
6. A. Gusev, Nanomaterials, Nanostructures, Nanotechnologies, Fismmatt, Moscow, 2007, p. 416.
7. A. Gusev, A. Rempel, Nanocrystalline Materials, Cambridge, 2004, p. 351.
8. D. Sreedhar, S. Devireddy, V. Veeredhi, *Materials Today*, **5**, 3403 (2018).
9. J. Zhang, T. Tian, Y. Chen, Y. Niu, J. Tang, A. L. Qin, *Chemical Physics Letters,* **591**, 78 (2014).
10. S. Park, J. An, J. Potts, A. Velamakanni, S. Murali, *Carbon,* **49**, 3019 (2011).
11. I. Moon, J. Lee, R. Ruoff, H. Lee, *Nature Communications,* **73** (1), (2010). https://doi.org/10.1038/ncomms1067.
12. K. Narasimharao, G. Venkata Ramana, D. Sreedhar, V. Vasudevaro, *J. Material Sci. Eng*., **5**, 284 (2016). doi:10.4172/2169-0022.1000284.
13. W. Hummers Jr., R. Offeman, *Journal of the American Chemical Society,* **80** (6), 1339 (1958).
14. A. Yu, I. Roes, A. Davies, Z. Chen, *Appl. Phys. Lett.,* **96**, 253105 (2010) https://doi.org/10.1063/1.3455879.
15. C. Liu, Z. Yu, D. Neff, A. Zhamn, *Nano Lett*., **10** (12) 4863 (2010).
16. J. Li, Y. Zhang, T. Gao, J. Han, X. Wang, B. Hultman, P. Xu, Z. Zhang, G. Wu, B. Song, *Journal of Power Sources*, **378**, 105 (2018).
17. H. Kim, Y. Chung, E. Lee, S. Lee, K. Cho, *Adv. Mater*., **26** (20), 3213 (2014). https://doi.org/10.1002/adma.201305940.
18. H. Wang, A. Hsu, T. Palasios, *IEEE Microwave Magazine,* **13** (4), 114 (2012).
19. B. Zhan, C. Li, J. Yang, G. Jenkins, W. Huang, X. Dong, *Small*, **10** (20), 4042 (2014).
20. X. Lee, B. Hiew, K. Lai, S. Gan, S. Thangalazhy-Gopakumar, S. Rigbyet, *Journal of the Taiwan Institute of Chemical Engineers***, 98**, 163 (2019).
21. W. Li, C. Tan, M. Lowe, H. Abruna, D. Ralph, *ACS Nano*, **5** (3), 2264 (2011).
22. I. Calizo, I. Bejenari, M. Rahman, G. Liu, A. Balandin, *J. Appl. Physics*, **106**, (2009). DOI: 10.1063/1.3197065.
23. W. Wang, Y. Wang, Y. Gao, Y. Zhao, *J. of Supercritical Fluids*, **85**, 95(2014).
24. A. Gupta, G. Chen, P. Joshi, S. Tadigadara, P. Eklund, *Nano Letters*, **6**, 2667 (2006).
25. B. Ossonon, D. Belanger, *RSC Adv*. **7**, 27224 (2017).
26. D. Jiang, Q. Yao, M. McKinney, C. Wilkie, *Polym. Degrad. Stab*., **63**, 423 (1999).
27. J. Lu, Y. Li, S. Li, S. Jiang, *Sci. Rep.* **6**, 21530 (2016).
28. D. Johnston, D. Shriver, *Inorg. Chem*. **32**, 1045 (1993).

Bulgarian Chemical Communications, Volume 58, Special Issue A (pp. 31-34) 2026 DOI: 10.34049/bcc.58.A.SN-06

Phase analysis and color characteristics of Co-, Cu-, and Ni-doped ceramic pigments

M. Georgieva*, F. Yovkova, A. Georgieva, I. Markovska, M. Minova

Burgas State University "Prof. Dr. Assen Zlatarov", 1 Prof. Yakimov Blvd., Burgas, 8010, Bulgaria

Received: July 02 2025; Revised: November 18, 2025

Applying a solid-phase synthesis method, ceramic materials of the Al_2O_3 – SiO_2 system were obtained by using pure raw materials. Cobalt, copper, and nickel were added as coloring ions, in an amount of 20%. Qualitative and quantitative analysis of the synthesized pigments was performed using X-ray diffraction. In the Al_2O_3 – SiO_2 system, the most important compound formed is mullite ($3Al_2O_3 \cdot 2SiO_2$). However, the results of the conducted studies show that with such a large amount of chromophore (20%), mullite is formed only with the addition of cobalt oxide. When adding nickel oxide, a tendency is observed to form predominantly nickel-aluminum spinel, and with the chromophore copper, the introduced CuO does not bind to Al_2O_3 but part of it passes into Cu_2O, so that in the system Al_2O_3 – SiO_2 – CuO the two copper oxides– CuO and Cu_2O are formed.

Keywords: ceramic pigments, solid-state sintering, CIELab system

INTRODUCTION

The most common carriers of color in pigments are the chromophores. These are atoms or atomic groups that have the ability to impart a certain color to the substances in which they are found. One of the most complete classifications is based on the crystal structure of the main phase. According to this classification of pigments, they can be spinel, willemite, garnet, zircon, etc. In the chemical technology of spinel pigments, various methods are currently used to obtain the final product. The main ones are ceramic and sol-gel methods. Sol-gel methods are associated with the presence of a stage of co-precipitation of divalent and trivalent metal ions with the formation of poorly soluble precipitates and the need to grind the agglomerate to a finely dispersed state. The color of pigments depends not only on the chemical nature of the introduced chromophore ion but also on the coordination in which it is located, as well as on the level of symmetry of the coordination polyhedron. The most stable and bright colors are those of the spinel series which have a cubic structure [1–3]. They are obtained mainly by solid-phase synthesis at high temperatures from chemically pure reagents or waste. Many scientists from all over the world are conducting research on the synthesis and study of various types of spinel pigments [4–8]. The developed compositions and technological regimes for obtaining cobalt- and nickel-containing spinel-type pigments using a solid-phase method ensure the production of pigments in a finely dispersed state with a particle size ≤50 μm [9]. In this connection, it is of interest to carry out the synthesis in a way that would allow the production of pigments with good color characteristics in a finely dispersed state. Therefore, the study of the processes of solid-phase synthesis of ceramic pigments, the conditions of their formation a spinel structure, and their influence on color is of great scientific and practical importance.

The purpose of the present work is the production of ceramic materials of the system Al_2O_3 - SiO_2 by the method of solid-phase synthesis.

EXPERIMENTAL

Methods

- *X-ray diffraction* – The phase composition was determined using a Philips X-ray diffractometer, with a PW1830 generator and a PW 1050 goniometer. The device was equipped with an X-ray tube with a copper anode, operating at a voltage of 40 kV and a current of 40 mA. The diffraction patterns were interpreted with the HighScore Plus program, using the ICSD (Inorganic Crystal Structure Database).
- *Color measurement* – The color of the pigments is determined spectrally by the Lovibond Tintometer RT 100 Color.

Materials

As initial raw materials, pure Al_2O_3 and $SiO_2 \cdot nH_2O$ with 20% chromophore introduced as Co_2O_3, NiO, and CuO were used. The most important operation, on which the reliability of the

* To whom all correspondence should be sent:
E-mail: *margaritageorgieva727@gmail.com*

technology and the stability in the quality of the finished pigment depend, is the preparation of the batch. In the case of poorly prepared batches, the coloring effect of the baked pigment may be reduced even when using chemically pure raw materials and optimal compositions.

The raw materials used for the synthesis of pigments by the solid-phase sintering method are dry and non-hygroscopic, which is why the dry method for preparing the batch was chosen. A crucial aspect in pigment synthesis is the precise dosing of the different components and adherence to the specified formulation.

The quantities of materials according to the recipe for 100 g of the batch are weighed on scales with an accuracy of 0.1 g, then mixed and homogenized in a planetary mill Pulverisette–6 of the company "Fritch" (Germany) in dry conditions.

The firing of the batches was carried out in a high-temperature furnace NaberTherm with a heating rate of 300 ÷ 400°C/h in air atmosphere in corundum crucibles with isothermal retention at the final temperature of 1 h. The pigments were fired at final temperatures of 1400°C.

Table 1 gives the compositions of the prepared pigments.

Table 1. Compositions of the pigments

Sample №	Composition		Chromophore
P1-20	Al_2O_3	$SiO_2{\cdot}nH_2O$	Co
P2-20	Al_2O_3	$SiO_2{\cdot}nH_2O$	Cu
P3-20	Al_2O_3	$SiO_2{\cdot}nH_2O$	Ni

Figure 1 shows the scheme by which the pigments are made.

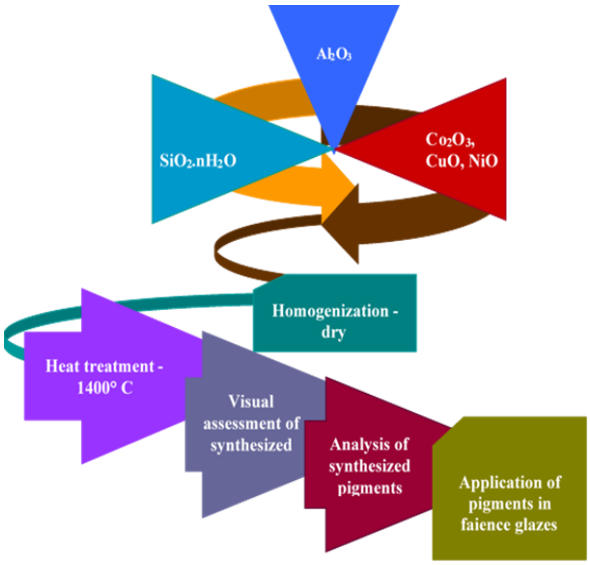

Figure 1. Scheme of pigment preparation

Photographs of the prepared batches are shown in Figure 2.

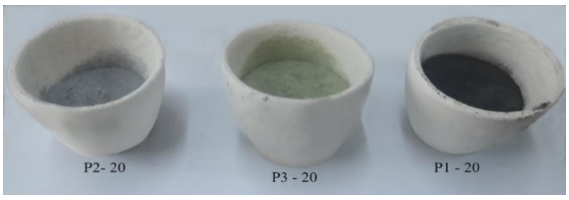

Figure 2. Photos of mixtures

RESULTS AND DISCUSSION

After firing and free cooling to room temperature of the synthesized pigments, a photograph was taken (Figure 3).

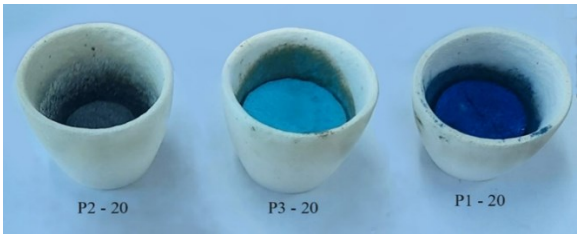

Figure 3. Photos of pigments

Color measurement

The color of the pigments was determined with a Lovibond Tintometer RT 100 Color in a spectral way, where:

- L* – brightness, L* = 0 – black color, L* = 100 – white color;
- a* – green color (–) / red color (+);
- b* – blue color (–) / yellow color (+).

The results of the measurements are presented in Table 2.

Table 2. Color coordinates of samples with compositions P1-20 ÷ P3-20

Sample №	T, °C	Color	L*	a*	b*
P1-20	1400		35.1	–0.5	–35.2
P2-20	1400		42.2	9.2	16.4
P3-20	1400		65.5	–24.7	–18.5

For composition P1-20 of the system Al_2O_3 – SiO_2 – CoO, the color characteristics are: green color a* = –0.5, blue color b* = –35.2. In the system Al_2O_3 – SiO_2 – CuO, brown-colored pigments were obtained, with an amount of red color a* = 9.2, and yellow color b* = 16.4. In the system Al_2O_3 – SiO_2 – NiO, pigments with a beautiful blue-green color were obtained, whose spectral indicators are: green color a* = –24.7 and blue color b* = –18.5.

X-ray analysis

- *Qualitative analysis.* Using X-ray diffraction (XRD), qualitative and quantitative

analysis of the finished pigments was performed. Figures 4, 5, and 6 present the results of the qualitative analysis of the pigments synthesized at 1400°C for 1 h, with cobalt, copper, and nickel chromophores.

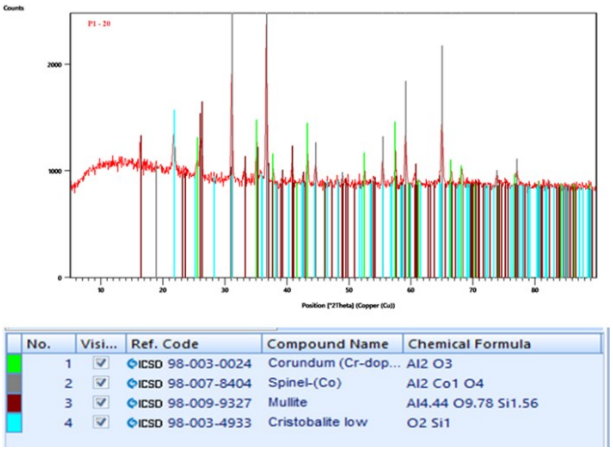

Figure 4. X-ray diffraction pattern for composition P1-20 (with chromophore cobalt)

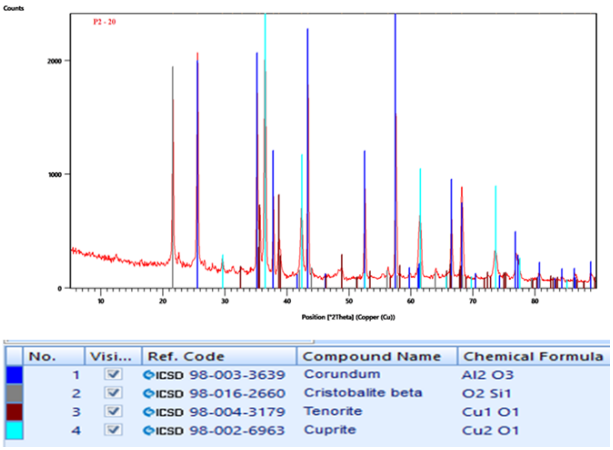

Figure 5. X-ray diffraction pattern for composition P2-20 (with chromophore copper)

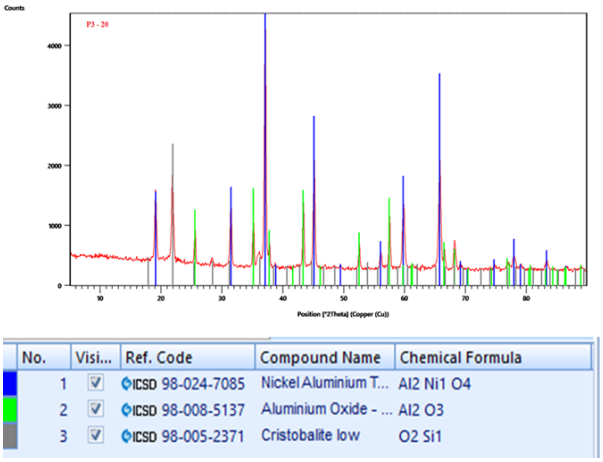

Figure 6. X-ray diffraction pattern for composition P3-20 (with chromophore nickel)

Due to the large amount of chromophore, in addition to mullite (Fig. 4), a very large amount of spinel (Al_2CoO_4), residual cristobalite – the high-temperature modification of SiO_2, and corundum (Al_2O_3) is formed. That is, at 20% of chromophore, mullite-spinel pigments are obtained.

In Fig. 5, no mullite formation is observed. The main phases are – corundum, cristobalite, and 2 copper oxides – tenorite and cuprite. That is, in the case of chromophore copper, the introduced CuO does not bind to Al_2O_3, and in the system, Al_2O_3 – SiO_2 – CuO, the two copper oxides – CuO and Cu_2O – are formed.

In Fig. 6 again no mullite phase is observed. Due to the large amount of the chromophore, it has bonded preferentially to aluminum oxide and the formed spinel. The main phases formed are corundum, nickel-aluminum tetroxide (nickel-aluminum spinel), and cristobalite.

- *Quantitative analysis.* The percent content of the main phases in the pigments with compositions P1-20 ÷ P3-20 is given in Figures 7 ÷ 9.

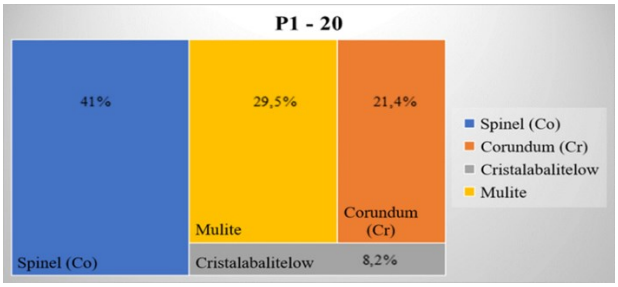

Figure 7. Quantities of the main phases in composition P1-20

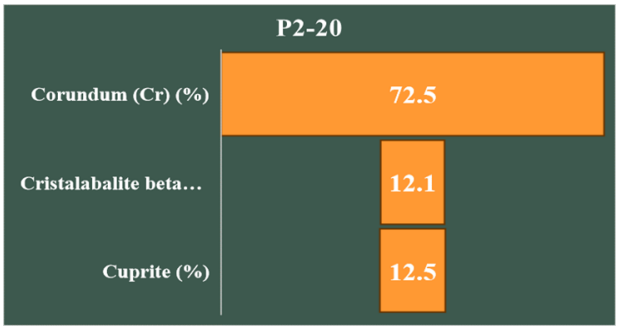

Figure 8. Quantities of the main phases in composition P2-20

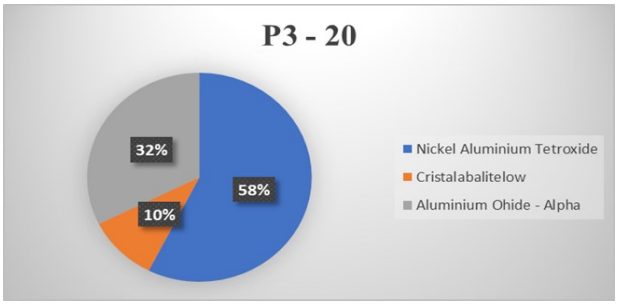

Figure 9. Quantities of the main phases in composition P3-20

CONCLUSIONS

Ceramic materials from the Al_2O_3 – SiO_2 system were obtained by a solid-phase synthesis method. Pure starting materials and chromophores in an amount of 20% were used. The optimal conditions for their preparation were determined.

The main phases and their amounts in the individual compositions were established by X-ray qualitative and quantitative analysis. Mullite is observed only in compositions P1-20. This is because the amount of the chromophore is large and spinels are predominantly formed. In compositions P1-20, aluminum-cobalt spinel (Al_2CoO_4) is found, and in compositions P3-20, nickel-aluminum spinel (Al_2NiO_4). Corundum and cristobalite are also observed in all compositions.

The influence of coloring ions and their quantity on the formation of the main mineral by solid-phase synthesis from chemically pure raw materials was studied, and it was found that pigments with saturated colors are obtained, with the best color characteristics being the pigments with composition P1-20 (a* = –0.5, and b* = –35.2) of the system Al_2O_3 – SiO_2 – CoO.

Acknowledgement: *The financial support of this work by the Bulgarian Ministry of Education and Science, National Research Fund under contract number KP-06-N87/14 is gratefully acknowledged.*

REFERENCES

1. S. Tumanov, V. Potrakov, *Glass and Ceramics*, **6**, 2 (1965).
2. N. Radishevskaya, N. Kasatsky, A. Chapskaya, O. Lepakova, V. Kitler, Yu. Naiborodnenko, V. Vereshchagin, *Glass and Ceramics*, **2**, 20 (2006).
3. A. Chapskaya, N. Radishevskaya, N. Kasatsky, O. Lepakova, Yu. Naiborodnenko, Abstracts of the Fifth Seminar of the Siberian Branch of the Russian Academy of Sciences – Ural Branch of RAS "Thermodynamics and Materials Science", September 26–28, 2005, Novosibirsk, 2005, p. 220.
4. Y. El Jabbar, H. Lakhlifi, R. El Ouatib, L. Er-Rakho, S. Guillemet-Fritsch, B. Durand, *Solid State Communications* **334–335**, 114394 (2021).
5. Y. Su, C. Chen, J. Wang, A. Han, M. Ye, *Ceramics International,* **50** (11), 18169 (2024).
6. A. Fernández-Osorio, E. Pineda-Villanueva, J. Chávez-Fernández, *Materials Research Bulletin,* **47** (2), 445 (2012).
7. P. Pimentel, S. Silva, G. Dantas, F. Aquino, R. Matos, *Ceramics International,* **51** (11), 13871 (2025).
8. N. Radishevskaya, A. Nazarova, O. Lvov, V. Kitler, R. Minin, *Ceramics International,* **50** (17), 29966 (2024).
9. A. Chapskaya, N. Radishevskaya, N. Kasatsky, O. Lepakova, Yu. Naiborodnenko, V. Vereshchagin, *Glass and Ceramics*, **12**, 27 (2005).

Bulgarian Chemical Communications, Volume 58, Special Issue A (pp. 35-43) 2026 DOI: 10.34049/bcc.58.A.SN-07

Application of adsorption isotherms for Cd(II) uptake by vine rod-derived biochar: a comparative study

V. Georgieva *, S. Syuleyman, L. Gonsalvesh, S. Mileva, D. Asamova, S. Genieva

Department of Chemistry, Burgas State University "Prof. Dr. Assen Zlatarov", 1 Prof. Yakimov Str., 8010 Burgas, Bulgaria

Received: August 12, 2025; Revised: January 06, 2026

This study examines the thermodynamic aspects of Cd(II) ion adsorption from aqueous solutions onto biochar derived from vine rods (BC-VR). Linear two- and three-parameter isotherm models were applied to characterize the adsorption process. Key physicochemical parameters were determined, and the models that best fit the experimental data were identified. The optimal isotherm model was chosen based on the coefficient of determination (R^2) and statistical error analysis. Model validation confirmed that the selected isotherm equations provide a reliable description of the distribution of Cd(II) ions between the liquid and biochar phases under the tested conditions, contributing to a deeper understanding of the adsorption mechanism and its thermodynamic behavior.

Keywords: Cd(II) adsorption, Thermodynamics, Linear isotherm modelling, Error analysis

INTRODUCTION

Cadmium was discovered in 1817 by the German chemist *Friedrich Strohmeyer* during the analysis of zinc-carbonate ores isolated as a by-product [1]. The newly found element "cadmium" is named from the Latin word *Cadmia* and the Greek word *καδμεία*, which were used to describe the common zinc ore, calamine [2]. During the 19th and 20th centuries, researchers focused on the properties and applications of cadmium. Cadmium is considered a transition metal, and its chemical properties resemble those of zinc and mercury. Although cadmium is relatively rare in its elemental form, it is frequently found as an impurity in zinc, lead, and copper ores [3]. Its natural origin is associated with geological processes, volcanic activity, forest fires, and its inherent presence in various environmental components. The cadmium content in the Earth's mantle is approximately 0.1 mg/kg, and it occurs in minerals such as CdS (greenockite, hawleyite), CdSe (cadmoselite), and others, or as an impurity in zinc and lead ores [4,5]. Cadmium concentrations vary significantly depending on the type of rock in the Earth's crust, with higher concentrations in sedimentary rocks (0.01-2.6 mg/kg) compared to magmatic (0.07-0.25 mg/kg) and metamorphic rocks (0.11-1.0 mg/kg) [1]. During weathering and erosion of rocks and minerals, cadmium is gradually released into the soil and water, contributing to its presence in the environment. Volcanic activity is also a significant factor: volcanic eruptions can release cadmium-containing ash and gases into the atmosphere. Although the amount of cadmium released during volcanic activity is relatively small compared to other sources, it can still contribute to local soil and water contamination upon deposition. Forest fires also release cadmium, as organic substances from vegetation and soil are emitted into the atmosphere and land. While the immediate effect of forest fires on cadmium mobility may be limited, this process could pose future problems as the released cadmium may accumulate in ecosystems.

Natural sources of cadmium include not only rocks and minerals but also sediments, soils, air, and natural waters, where its concentrations vary considerably. In soils, cadmium content typically ranges from 0.1 to 1 mg/g, but certain regions and geographical areas have significantly higher levels. Certain regions in Europe, including Ireland, Poland, Goslar (Germany), and Southern Sardinia, have been identified as areas with elevated cadmium levels [6–8]. Although cadmium readily accumulates in the soil, its bioresistance causes it to be released slowly and inefficiently. Due to its high mobility in the environment, significant amounts of cadmium enter freshwater basins, where sedimentation occurs and cadmium is integrated into groundwater. Between 140 and 1,500 tons of cadmium into the atmosphere annually, with weathering of rocks playing a substantial role in its mobilization [9]. Approximately 50% of the cadmium is transferred into water bodies, with the remaining portion being released into the atmosphere through volcanic eruptions and forest fires.

* To whom all correspondence should be sent:
E-mail: *velyana_topalska@btu.bg*

There are also anthropogenic sources of cadmium, such as mining processes, metal refining, battery production, and the use of paints and pigments, which release significant amounts of cadmium into the environment [1]. Global annual cadmium production has steadily increased, from 18,100 tons in 1994 to a peak of 25,000 tons in 2017, with a slight decrease to 23,000 tons in 2023 [10]. Canada is the leading producer of cadmium, with major consumers including Japan, Mexico, the USA, and Peru [11, 12]. Zinc, lead, and copper mining releases significant amounts of cadmium, which affects soil and water quality. In China, cadmium concentrations in wastewater from areas where lead-zinc ores are mined or processed have been recorded at 2-4 times the permissible limits for drinking water (5 μg/dm^3 [11]) [3]. The burning of fossil fuels in power plants and industrial facilities is another anthropogenic source of cadmium through dust and gas emissions, which can travel long distances and contaminate soils and waters.

Cadmium possesses unique toxicological properties, making it a serious environmental issue. It is highly persistent in the environment, can accumulate in soils, sediments, and organisms, and can bioaccumulate through the food chain. Cadmium does not play a biological role in organisms, which is why it causes severe toxic effects. Its impact on the body includes damage to the cardiovascular, urinary, gastrointestinal, neurological, and respiratory systems. This heavy metal directly affects cellular division, potentially causing cell death. It has been found to induce genetic mutations and chromosomal abnormalities by inhibiting DNA replication. Its toxicity is linked to the suppression of cellular respiration and the activity of key antioxidant enzymes [2, 13]. Humans are protected from chronic exposure to low cadmium concentrations by the presence of metallothioneins – a group of small, widely distributed proteins rich in cysteine, which regulate zinc metabolism. Metallothioneins play a crucial role in protecting against ion toxicity from several heavy metals, DNA damage, and oxidative stress. The biological half-life of cadmium in the bloodstream is estimated to range from 75 to 128 days, reflecting its accumulation in organs rather than the rate of body clearance [2, 5]. According to the World Health Organization, the temporary acceptable weekly intake of this heavy metal is 2.5 μg/kg body weight [14], with concentrations above this limit considered hazardous to health.

To reduce Cd(II) pollution, it is essential to implement strict control measures on sources of contamination and proper waste management, including wastewater treatment. Given the widespread contamination with cadmium and its low recommended levels in drinking water, there is significant interest in developing effective methods for removing this metal from contaminated waters. Various technologies have been developed for treating industrial wastewater containing heavy metals, including adsorption, chemical precipitation, ion exchange, and membrane filtration. Among these, adsorption has become a proven and effective method for removing heavy metals from water and soil [15]. In the search for renewable energy sources, biomass has emerged as a promising source of chemical feedstocks. Biochar, a porous carbonaceous material obtained by pyrolyzing carbon-rich biomass in an oxygen-limited environment, is considered a promising, cost-effective, and efficient adsorbent for heavy metal removal from water. This is due to the presence of polar functional groups, such as carboxyl, hydroxyl, and amino groups, which facilitate the adsorption of heavy metals. Biochar from vine rods, a carbon-rich, porous material typically produced by thermally decomposing biomass in an oxygen-deprived environment, is regarded as a promising alternative adsorbent for various pollutants.

Accurate modeling of adsorption isotherms is crucial for the effective understanding and optimization of heavy metal removal processes. Although classical two-parameter models such as Langmuir and Freundlich provide valuable baseline information, three-parameter isotherm models offer greater flexibility and can more accurately capture the complexity of adsorption phenomena by accounting for additional physicochemical interactions. The present study investigates the applicability and performance of linear two and three-parameter isotherm models in describing the adsorption of Cd(II) ions onto biochar derived from vine rods. By conducting a comparative analysis, this study seeks to advance the understanding of the physicochemical properties of the examined adsorbent and elucidate the adsorption mechanism, ultimately supporting the design of more efficient biochar-based remediation approaches.

EXPERIMENTAL

Adsorbent preparation

Vine rods were sourced from the processing of *Vitis* plants in proximity to the town of Pomorie, Bulgaria. The initial treatment of this agro-waste material involved rinsing with distilled water, followed by air drying, grinding, and sieving through a 2 mm mesh to standardize particle size. The resulting material underwent slow pyrolysis in a

VEB Elektro Bad Frankenhausen LM 312.11 electric muffle furnace (Germany), conducted in a nitrogen atmosphere (99.9% purity). The temperature was increased gradually at a rate of 10 K/min to 773 K, with each 373 K increment maintained for 1 hour. After pyrolysis, the biochar was sieved, and the fraction with particle sizes ranging from 63 to 250 μm was selected for tests in the adsorption experiments.

Adsorbent characterization

The specific surface area of the obtained biochar was determined using the procedure described in the reference [16]. Surface functional groups of the tested biochar were identified in the range of 4000–400 cm^{-1} using a Nicolet iS 50 FTIR spectrometer (Thermo Scientific) to assess the possible interactions with the applied adsorbate.

Adsorbate

The stock solution containing 1000 mg/L of Cd(II) was prepared by dissolving 2.744 g of $Cd(NO_3)_2 \cdot 4H_2O$ (Merck) in ultrapure water. Working solutions of Cd(II) with concentrations ranging from 5 to 200 mg/L were subsequently prepared by serial dilution of the stock solution with ultrapure water.

Adsorption experiments

Adsorption experiments were conducted by varying the pH in the range of 2.5 to 8.5 for a contact time of 24 h, using a fixed adsorbent dose of 0.3 g, an initial concentration of 5 mg/L, and a constant temperature of 298 K. The desired pH values were adjusted by adding appropriate amounts of 0.1 M HCl or 0.1 M NaOH to the respective solutions. A volume of 100 mL of the test solution and 0.3 g of the adsorbent were placed in 200 mL iodine flasks and incubated in a Memmert WB22 (Germany) water bath equipped with a shaking system. The temperature was maintained with a precision of ±0.5°C.

Thermodynamic studies were carried out at the optimized pH value at three different temperatures (293, 298 and 303 K) and six initial concentrations ranging from 5 to 200 mg/L for 24 hours, using a fixed adsorbent dose of 0.3 g. Samples taken before and after the adsorption process were analyzed according to the standard BDS EN ISO 17294-2:2016 using an ICP-MS mass spectrometer, model iCAP Q (Thermo Scientific).

The percent removal of Cd(II) ions by BC-VR ($R_{Cd(II)}$, %) and the equilibrium adsorption capacity (Q_{eq}, mg/g), representing the amount of ions adsorbed per unit mass of adsorbent, were calculated using the following equations:

$$R_{Cd(II)},\% = \frac{C_o - C_{eq}}{C_o} \times 100 \quad (1)$$

$$Q_{eq} = \frac{C_0 - C_t}{m} \times V, \quad (2)$$

where C_o is the initial concentration of Cd(II) ions and C_{eq} - the concentration at equilibrium, mg/L, V is the solution volume, L, and m is the weight of the adsorbent, g.

Adsorption isotherms

Equilibrium adsorption data are typically interpreted using isotherm models, which provide a reliable means for understanding the underlying adsorption mechanisms, estimating the maximum adsorption capacity, and assessing the characteristics of the adsorbent. In this study, the adsorption behavior was examined by applying nine different isotherm models (Table 1).

The experimental results were processed using Microsoft Excel (Office 2019, USA), and the model parameters were obtained through linear regression analysis. Although the coefficient of determination (R^2) serves as the primary indicator for model fitting, it does not alone ensure model validity. Therefore, additional statistical criteria namely, the chi-square (χ^2) test and Marquardt's percentage standard deviation (*MPSD*) – were also employed, following the formulas provided in reference [19]. The Akaike Information Criterion (*AIC*) is a widely used metric for model evaluation and selection, combining goodness of fit and model complexity (number of parameters, p). It is calculated as follows [19]:

$$AIC = n \ln\left(\frac{SSE}{n}\right) + 2(p+1) + \frac{2(p+1)(p+2)}{n-p-2}, \quad (12)$$

where n is the number of experimental data, *SSE* – sum of the squares of errors [19, 26]. A lower *AIC* value indicates a better balance between data fit and simplicity. By penalizing excessive complexity, *AIC* helps prevent overfitting and supports the selection of models with good predictive performance.

Table 1. The applied isotherm models

Isotherm model	Linear form	Slope, Intercept	Eqs.	Ref.
Freundlich (Fr)	$\ln Q_{eq} = \ln K_F + \frac{1}{n_F} \ln C_{eq}$	Slope $1/n$, Int. $\ln K_F$	(3)	[17]
Langmuir (L)	$\frac{C_{eq}}{Q_{eq}} = \frac{1}{K_L Q_{max}} + \frac{1}{Q_{max}} C_{eq}$	Slope $1/Q_{max}$, Int. $1/K_L Q_{max}$	(4)	[18, 19]
Dubinin Radushkevich (D-R)	$\ln Q_{eq} = \ln Q_{DR} - K\varepsilon^2$, $RT \ln\left(1+\frac{1}{C_{eq}}\right) = \varepsilon$	Slope K_{DR}, Int. $\ln Q_{DR}$	(5)	[17, 20]
Temkin (Tem)	$Q_{eq} = B \ln A_T + B \ln C_{eq}$, $\frac{RT}{b_T} = B$	Slope B, Int. $B \ln A_T$	(6)	[18]
Scatchard (Sc)	$\frac{Q_{eq}}{C_{eq}} = K_{Sc}\left(\vartheta_{Sc}^0 - Q_{eq}\right)$	Slope K_{Sc}, Int. $K_{Sc}\vartheta_{Sc}^0$	(7)	[21]
Redlich-Peterson (R-P)	$\ln\left(K_{RP}\frac{C_{eq}}{Q_{eq}} - 1\right) = \ln \alpha_{RP} + \beta_{RP} \ln C_{eq}$	Slope β_{RP}, Int. $\ln \alpha_{RP}$	(8)	[22]
Toth (Th)	$\frac{C_{eq}}{Q_{eq}} = \frac{1}{(Q_{Th})^{Th} K_{Th}} + \frac{C_{eq}}{(Q_{Th})^{Th}}$	Slope $(Q_{Th})^{-Th}$, Int. $\left((Q_{Th})^{Th} K_{Th}\right)^{-1}$	(9)	[23]
Radke-Prausnitz (R-Pr)	$\frac{C_{eq}}{Q_{eq}} = \frac{1}{K_{RPr} k_{rpr}} + \frac{C_{eq}^P}{k_{rpr}}$	Slope $\left(k_{rpr}\right)^{-1}$, Int. $\left(K_{RPr} k_{rpr}\right)^{-1}$	(10)	[20]
Sips (S)	$\ln\left(\frac{Q_{eq}}{Q_m - Q_{eq}}\right) = \frac{1}{n} \ln C_{eq} + \ln\left(b_s\right)^{1/n}$	Slope $\frac{1}{n}$, Int. $\ln\left(b_s\right)^{1/n}$	(11)	[24, 25]

RESULTS AND DISCUSSION

To determine the specific surface area of the studied material, the procedure described in reference [16] was employed. The iodine adsorption number, which reflects the material's ability to adsorb iodine from solution, serves as an indirect measure of surface area and is commonly used to assess the porosity of activated carbons. In this context, the derived iodine number falls within the range of 360–435 mg/g, suggesting that the material predominantly possesses microporous characteristics. These values indicate that the sample has promising potential for applications in adsorption processes, particularly for the removal of small-sized contaminants.

The FTIR spectra of the sample before and after Cd(II) adsorption are shown in Figure 1 to facilitate the identification of functional groups involved in surface interactions during the adsorption process.

The FTIR spectra of the biochar derived from vine roots, recorded before and after Cd(II) adsorption, exhibit no notable changes in the positions or intensities of the main absorption bands, indicating preservation of the material's surface functional groups during the adsorption process.

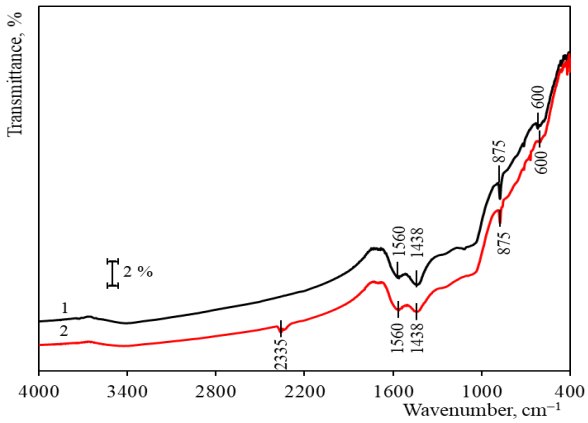

Fig. 1. FTIR spectra of BC-VR: 1 – before, 2 – after Cd(II) adsorption

The bands observed at 1560 cm^{-1} and 1428 cm^{-1} are assigned to the stretching vibrations of C=C bonds in alkenes and/or C–C bonds within aromatic ring structures. Out-of-plane deformation vibrations of =C–H groups are evidenced by the absorption bands at 875 cm^{-1} and 600 cm^{-1}, characteristic of aromatic moieties. A distinct band appearing at 2335 cm^{-1} in the spectrum of the sample after adsorption is attributed to the presence of physisorbed CO or CO_2 gases on the biochar surface [27], possibly due to exposure to atmospheric air or gas evolution

during adsorption. A comparative analysis of the FTIR spectra of biochar derived from vine rods and walnut shell biochar (WSBA, from our previous study [26]) reveals several common spectral features, suggesting structural similarities between the two materials. Both samples exhibit absorption bands around 1560 cm^{-1} and 1438–1428 cm^{-1}, which are attributed to the stretching vibrations of C=C bonds in aromatic rings, indicative of conjugated π-electron systems characteristic of partially carbonized structures. Additionally, both materials show bands near 875 cm^{-1}, associated with out-of-plane deformation vibrations of =C–H bonds in aromatic moieties. The vine rod biochar also exhibits a band at 600 cm^{-1}, which may correspond to additional deformation modes or arise from mineral components. Overall, the spectral profiles of both biochars suggest a predominantly aromatic structure with minimal contributions from oxygen-containing functional groups. The absence of significant spectral changes after Cd(II) adsorption onto vine rod biochar – analogous to the functional simplicity of WSBA – suggests that the adsorption process is likely governed by π–π interactions, surface area, and van der Waals forces, rather than by specific reactive surface functionalities.

The influence of temperature and solution pH on the removal efficiency of Cd(II) ions is presented in Fig. 2.

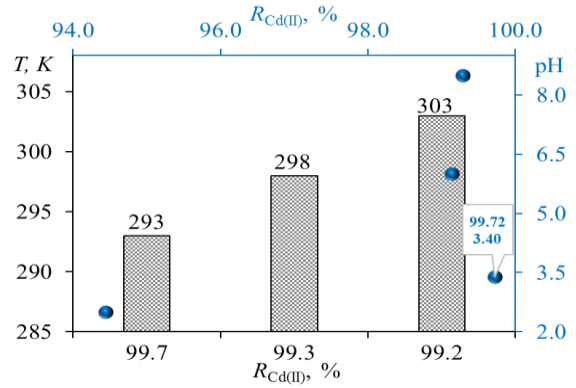

Fig. 2. pH and temperature effects onto adsorption process with BC-VR at initial Cd(II) concentration of 5 mg/L

The adsorption experiments conducted at 293, 298, and 303 K demonstrate that the removal efficiency remained consistently high, exceeding 99% under all investigated conditions. These results suggest that within the studied temperature range, thermal effects exert only a minor influence on the adsorption process, indicating that the interaction between Cd(II) ions and the bioadsorbent surface is not strongly temperature dependent. In contrast, the solution pH had a more pronounced effect on Cd(II) uptake. At highly acidic conditions (pH 2.5), the removal efficiency was significantly reduced (94.4%), which can be attributed to the competition between hydrogen ions and Cd(II) species for the active adsorption sites. As the pH increased to 3.40, the removal efficiency reached 99.72%, reflecting the reduced competition from protons and the enhanced availability of negatively charged functional groups on the adsorbent surface. Due to this maximum value of 99.72%, the pH of 3.4 was adopted as the optimal condition for the studied adsorption process. At pH values of 6.0 and 8.5, the removal efficiency remained very high and nearly constant (99.1–99.3%), suggesting that the bioadsorbent is highly effective over a broad pH range.

Overall, the results indicate that while the adsorption of Cd(II) onto BC-VR is only weakly affected by temperature, solution pH plays a decisive role in the process. The sharp increase in efficiency between pH 2.5 and 3.4 highlights the importance of electrostatic interactions and the ionization state of surface functional groups, whereas the stability of the efficiency at near-neutral and slightly alkaline conditions confirms the strong affinity of the adsorbent for Cd(II) ions.

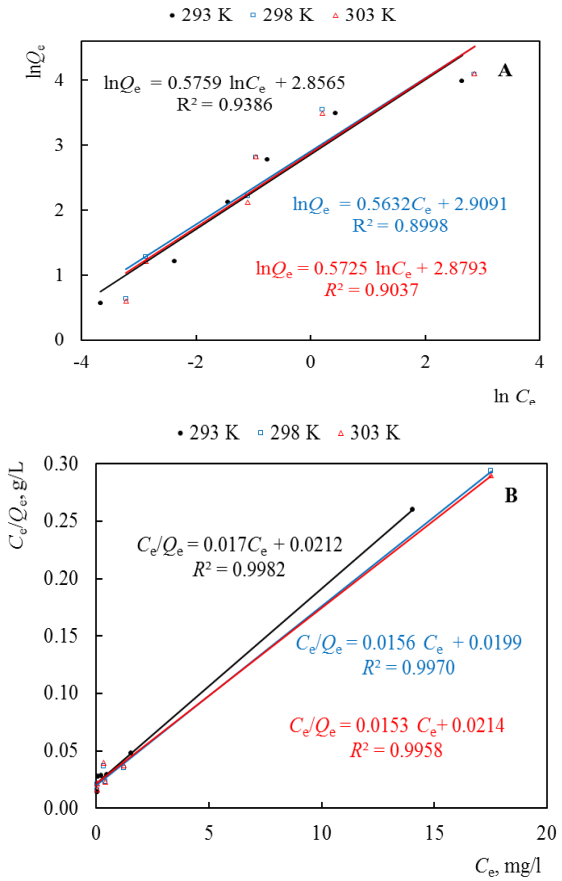

Fig. 3. Linear adsorption isotherms of *Freundlich* (A) and *Langmuir* (B) models for Cd(II) adsorption onto BC-VR at different temperatures

For the thermodynamic investigation of Cd(II) ion adsorption onto vine-rod biochar (BC-VR), experiments were performed within the concentration range of 5–200 mg/L under continuous maximum-speed shaking, at an adsorbent dose of 3 g/L, pH 3.4, and temperatures of 20, 25, and 30 °C. The obtained data were analyzed using all adsorption isotherm models described in the experimental section.

For a detailed characterization of the studied adsorption process, classical linearized isotherm models, such as those proposed by *Freundlich* and *Langmuir*, were employed. The graphical representations of these two isotherms are presented in Fig. 3.

The *Freundlich* equation fits at medium contaminant concentrations and energy heterogeneity at the adsorbent surface. It can be seen from Fig. 3A that there is no good linear correlation. The physicochemical parameters of the *Freundlich* isotherm are presented in Table 2. The *Langmuir* isotherm characterizes the process occurring on a homogeneous adsorbent surface with a uniform distribution of adsorption centers and no interaction between adsorbed molecules of the monolayer. By using the parameters from the *Langmuir* adsorption isotherm Q_{max} and K_L, the adsorption capacity and the suitability of the adsorbent under the tested conditions were evaluated by calculating the separation factor (R_L) [28].

Table 2. Error analysis and physicochemical parameters of linear isotherm models applied to Cd(II) adsorption onto vine-rod biochar at different temperatures

Isoth.	T, K	Parameters			R^2	χ^2	*MPSD*	*AIC*
		K_F ($L^{1/n}$ $mg^{1-1/n}$/g)	1/n					
Fr	293	17.40	1.74		0.939	15.4	37.2	47.3
	298	18.34	1.78		0.900	24.9	48.2	50.2
	303	17.80	1.75		0.904	23.6	46.9	79.7
L	T, K	K_L (L/mg)	Q_{max} (mg/g)	R_L	R^2	χ^2	*MPSD*	*AIC*
	293	0.80	58.77	6.50×10^{-3}	0.998	0.5	20.3	10.5
	298	0.78	63.98	6.54×10^{-3}	0.997	30.2	26.9	28.1
	303	0.72	65.29	6.25×10^{-3}	0.996	2.4	29.7	58.0
D-R	T, K	$K \times 10^8$ (mol^2/kJ^2)	Q_{DR} (mg/g)	E (kJ/mol)	R^2	χ^2	*MPSD*	*AIC*
	293	3.86	26.53	3.60	0.826	35.7	67.9	47.9
	298	4.42	32.45	3.36	0.883	2.4	77.3	48.0
	303	3.86	26.53	3.41	0.826	33.5	67.6	78.5
Tem	T, K	b_T (J/mol)	A_T (L/mg)		R^2	χ^2	*MPSD*	*AIC*
	293	273.5	20.83		0.939	5.11	215.7	36.3
	298	253.3	19.92		0.945	6.36	126.1	36.9
	303	255.5	18.93		0.943	11.53	169.2	67.2
Sc	T, K	K_{Sc} (L/mg)	ϑ_{Sc}^0 (mg/g)		R^2	χ^2	*MPSD*	*AIC*
	293	0.92	55.89		1.000	0.8	22.4	20.2
	298	0.80	65.57		0.737	31.4	28.4	27.9
	303	0.75	66.36		0.717	2.3	31.9	57.9
R-P	T, K	K_{RP} (L/g)	α_{RP} (L/mg)	β_{RP}	R^2	χ^2	*MPSD*	*AIC*
	293	94.63	3.81	0.595	0.935	6.73	9.8×10^2	71.2
	298	92.30	3.29	0.590	0.870	2.04	1.7×10^3	77.6
	303	2.0×10^6	1.1×10^5	0.428	0.840	23.56	5.4×10^1	1.2×10^3
Th	T, K	K_{Th} $(mg/L)^{Th}$	Q_{Th} (mg/g)	Th	R^2	χ^2	*MPSD*	*AIC*
	293	0.80	58.77	1.000	0.998	0.51	23.5	40.5
	298	0.79	64.97	0.996	0.997	0.30	31.5	57.9
	303	0.71	65.29	1.000	0.996	2.44	34.3	58.0

R-Pr	*T*, K	K_{RPr} (L/g)^P	k_{rpr} [(mg g^{-1}) /(mg L^{-1})]$^{1/P}$	*P*	R^2	χ^2	*MPSD*	*AIC*
	293	0.89	54.53	0.97	0.998	0.53	23.4	42.8
	298	0.68	71.51	1.04	0.997	0.51	31.3	57.0
	303	0.70	66.22	1.00	0.996	2.42	34.3	57.9
S	*T*, K	b_S (L/mg)	Q_m (mg/g)	1/*n*	R^2	$\chi 2$	*MPSD*	*AIC*
	293	0.72	60.67	0.992	0.992	1.09	26.0	46.8
	298	0.86	63.20	1.017	0.986	2.62	45.1	61.4
	303	0.77	64.67	1.002	0.984	2.34	42.4	57.7

In a similar manner, the experimental data were processed according to the two-parameter adsorption isotherms of *Dubinin–Radushkevich*, *Temkin*, and *Scatchard*, and the physicochemical parameters obtained for each isotherm are presented in Table 2.

The *Dubinin–Radushkevich* model supported physical adsorption based on the mean adsorption energy (*E*), which values are 3.36–3.60 kJ/mol (Table 2). Although the correlation coefficients are lower (R^2 = 0.826–0.883), the D–R model provides useful insights into the adsorption mechanism. The moderate variation of Q_{DR} with temperature (26.5–32.5 mg/g) is consistent with the observed temperature dependence. The *Temkin* constants revealed relatively high adsorption energy at the lowest temperature (b_T = 273.5 J/mol at 293 K), which decreases slightly with increasing temperature. This trend suggests stronger initial binding at low temperature, followed by a stabilization of adsorption sites at elevated temperatures. Although R^2 values (0.939–0.945) are acceptable, the large *MPSD* values (126–216) indicate a less precise description compared to the *Langmuir* model. The *Scatchard* model produced an excellent fit at 293 K (R^2 = 1.000), but the correlation decreased sharply at higher temperatures (R^2 = 0.717–0.737). This implies that the *Scatchard* equation may describe the adsorption process well under specific conditions (low temperature), but it is less reliable across the full temperature range. When a satisfactory agreement is obtained between the experimental data and the calculated values derived from the *Langmuir* isotherm equation, it is recommended to also apply alternative three-parameter isotherm models. These include the *Redlich–Peterson*, *Toth*, *Radke–Prausnitz*, and *Sips* isotherms. The application of such models provides higher accuracy in the determination of thermodynamic constants, which is particularly important for achieving a deeper understanding of the adsorption processes. For the analysis of the linear relationships characteristic of the respective isotherms, the Solver add-in of Microsoft Excel was employed to obtain maximum values of the coefficient of determination (R^2). At 293 K, the R–P model showed reasonable fitting (R^2 = 0.935) with β ≈ 0.6, reflecting intermediate behavior between *Langmuir* and *Freundlich* models. However, at higher temperatures, both the correlation and physical relevance of the constants deteriorated (e.g., extremely large values at 303 K), suggesting limited applicability of this model under the studied conditions. The *Toth* model yielded excellent agreement with experimental data (R^2 = 0.996–0.998). The values of the heterogeneity factor (Th ≈ 1) indicate that the surface behaves nearly homogeneously, consistent with the *Langmuir* assumption. The increasing Q_{Th} values with temperature confirm the enhanced adsorption capacity at higher temperatures. The three-parameter model R-Pr also showed very high correlation (R^2 = 0.996–0.998), with parameter *P* values close to unity, further supporting monolayer adsorption on a homogeneous surface. The results closely resemble those of the *Langmuir* and *Toth* models, reinforcing their suitability. The *Sips* model produced good correlations (R^2 = 0.984–0.992) with heterogeneity parameter 1/*n* close to unity, again suggesting that the adsorption system approaches *Langmuir*-type behavior. The maximum adsorption capacity (Q_m) increases slightly with temperature, in line with the other models.

Overall, the adsorption of Cd(II) onto BC-VR is best described by the *Langmuir* and *Sips* models, which exhibited the highest correlations (R^2 > 0.99), the lowest error values, and the most favorable *AIC* scores. Ultimately, the *Langmuir* isotherm emerges as the most appropriate model, as it is simpler (requiring fewer parameters than the *Sips* model) while consistently providing excellent results at all investigated temperatures. These findings confirm that the process follows monolayer adsorption on a relatively homogeneous surface with enhanced capacity at higher temperatures. To place the present results in context, the thermodynamic constants of Cd(II) adsorption obtained in this study were compared with literature data for other adsorbents (Table 3).

Table 3. Comparison of thermodynamic constants during adsorption of Cd(II) ions on different adsorbents

Adsorbents	Conditions	Q_{max}, mg/g	K_L, L/mg	Ref.
Pistachio hull waste	pH 5.5 (23±2°C)	14.90	0.0300	[29]
	pH 6.5 (23±2°C)	20.30	0.0600	
Biochars derived from grape vine shoots GVS-600	pH > 3	286.40	9.0590	[30]
Walnut shell	pH 6.0 (25°C)	7.29	0.0174	[31]
Oak bark biochar	pH 5 (25°C)	0.37	0.0377	[32]
Pine bark char		0.34	0.0002	
Oak bark biochar		5.40	0.0055	
Vine rod-derived biochar -Iran	pH 6.0 (40°C)	45.50	-	[33]
Phosphate modified grape branch biochar 0.2 PB	pH > 3 (25°C)	14.02	0.3320	[34]
Vine rod-derived biochar BC-VR	pH 3.4 (25°C)	64.27	0.8289	Present study

Table 3 summarizes the thermodynamic constants for various adsorbents, enabling comparison of the maximum adsorption capacity (Q_{max}) for Cd(II) removal from aqueous solutions. The data show that adsorption performance strongly depends on both the adsorbent type and experimental conditions. Among the reported materials, vine-rod biochar GVS-600 exhibits the highest adsorption capacity (Q_{max} = 286.4 mg/g), followed by the present study's biochar (BC-VR, Q_{max} = 64.3 mg/g) and vine-rod biochar from Iran (Q_{max} = 45.5 mg/g). In contrast, lower capacities were obtained for pistachio shells, phosphate-modified vine-rod biochar, walnut shells, and various wood-derived biochars. The K_L values confirm the superior affinity of GVS-600, while the BC-VR examined in this work also demonstrates competitive adsorption efficiency, highlighting its potential as a cost-effective material for Cd(II) removal from water.

CONCLUSIONS

Vine-rod biochar (BC-VR) proved to be a highly efficient and favorable adsorbent for Cd(II) removal from aqueous solutions. The process follows the *Langmuir* isotherm, confirming monolayer adsorption on a relatively homogeneous surface, with capacity increasing at higher temperatures. The predominantly aromatic structure with limited oxygen functionalities suggests that adsorption is governed mainly by π–π interactions, surface area, and van der Waals forces. Under optimized conditions (pH 3.4, dose 3 g/L), BC-VR demonstrates competitive adsorption capacity, highlighting its potential for practical water treatment applications.

REFERENCES

1. A. Dhanda, Ritambhara, S. Lamba, R. Prakash, in: *Cadmium Toxic. Water*, A. K. Jha, N. Kumar (eds.), 2024, p. 3.
2. M. Peana, A. Pelucelli, C. T. Chasapis, S. P. Perlepes, V. Bekiari, S. Medici, M. A. Zoroddu, *Biomolecules*, **13**, 1 (2023).
3. B. Du, J. Zhou, B. Lu, C. Zhang, D. Li, J. Zhou, S. Jiao, K. Zhao, H. Zhang, *Sci. Total Environ.*, **720**, 137585 (2020).
4. F. Pinot, S. E. Kreps, M. Bachelet, P. Hainaut, M. Bakonyi, B. S. Polla, *Rev. Environ. Health*, **15**, 299 (2000).
5. R. A. Bernhoft, *Sci. World J.*, 394652 (2013).
6. M. J. Canty, A. Scanlon, D. M. Collins, G. McGrath, T. A. Clegg, E. Lane, M. K. Sheridan, S. J. More, *Sci. Total Environ.*, **485–486**, 223 (2014).
7. E. A. Lane, M. J. Canty, S. J. More, *Res. Vet. Sci.*, **101**, 132 (2015).
8. J. Pan, J. A. Plant, N. Voulvoulis, C. J. Oates, C. Ihlenfeld, *Environ. Geochem. Health,* **32**, 1 (2010).
9. Council of Ministers, Cadmium Review 2003.
10. Y. Bin Yu, J. W. Lee, A. H. Jo, Y. J. Choi, C. Y. Choi, J. C. Kang, J. H. Kim, *Toxics*, **12**, 1 (2024).
11. G. Fatima, A. M. Raza, N. Hadi, N. Nigam, A. A. Mahdi, *Indian J. Clin. Biochem.*, **34**, 371 (2019).
12. Y. B. Gelaw, H. Dagne, B. Adane, G. Yirdaw, M. Moges, Z. Aneley, L. Kumlachew, A. Aschale, Y. A. Deml, E. Tegegne, T. A. Birhan, *Heliyon*, **10**, e40389 (2024).
13. K. Jomova, S. Y. Alomar, E. Nepovimova, K. Kuca, M. Valko, Heavy Metals : Toxicity and Human Health Effects , Springer, Berlin Heidelberg, 2025.
14. A. Cantoral, S. Collado-López, L. Betanzos-Robledo, H. Lamadrid-Figueroa, B. A. García-Martínez, C. Ríos, A. Díaz-Ruiz, R. M. Mariscal-Moreno, M. M. Téllez-Rojo, *Foods*, **13**, 3649 (2024).
15. R. Hamzenejad, E. Sepehr, A. Samadi, M. H. R. Sadaghiani, H. Khodaverdiloo, *J. Environ. Stud.*, **43**, 401 (2017).
16. a U. Itodo, F. W. Abdulrahman, L. G. Hassan, S. a Maigandi, H. U. Itodo, *New York Sci. J.*, **3**, 25 (2010).
17. P. S. Vassileva, L. P. Ivanova, A. K. Detcheva, *Bulg. Chem. Commun.*, **54**, 21 (2022).
18. B. Hazar, D. Şakar, *Bulg. Chem. Commun.*, **56**, 215 (2024).
19. Y. Wang, C. Wang, X. Huang, Q. Zhang, T. Wang, X. Guo, *Chemosphere*, **349**, 140736 (2024).

20. S. Bbumba, *Adv. Image Video Process.*, **12**, (2024).
21. H. Saad, F. A. Nour El-Dien, N. E. A. El-Gamel, A. S. Abo Dena, *RSC Adv.*, **14**, 1316 (2024).
22. K. H. Chu, M. A. Hashim, Y. T. da C. Santos, J. Debord, M. Harel, J. C. Bollinger, *Chem. Eng. Sci.*, **285**, 119573 (2024).
23. M. G. Davis, K. Yan, J. G. Murphy, *Biogeosciences*, **21**, 5381 (2024).
24. A. M. Carvajal-Bernal, F. Gomez-Granados, L. Giraldo, J. C. Moreno-Pirajan, *Eur. J. Chem.*, **8,** 112 (2017).
25. S. Svilović, D. Rušić, R. Stipišić, N. Kuzmanić, *Bulg. Chem. Commun.*, **52**, 189 (2020).
26. V. G. Georgieva, L. Gonsalvesh, M. P. Tavlieva, *J. Mol. Liq.*, **312**, 112788 (2020).
27. B. Smith, Infrared Spectral Interpretation, CRC Press, February 6, 2018.
28. M. Prelac, I. Palčić, D. Cvitan, D. Anđelini, M. Repajić, J. Ćurko, T. K. Kovačević, S. Goreta Ban, Z. Užila, D. Ban, N. Major, *Materials (Basel).*, **16**, 4716 (2023).
29. M. Hamidpour, N. Hosseini, V. Mozafari, M. Heshmati Rafsanjani, *Rev. Int. Contam. Ambient.*, **34**, 307 (2018).
30. H. Li, D. Yao, Q. Feng, H. Zeng, J. Liang, Z. Zhou, Y. Tian, N. Zhou, X. Lu, *Desalin. Water Treat.*, **118**, 195 (2018).
31. R. Najam, S. M. A. Andrabi, *Desalin. Water Treat.*, **57**, 27363 (2016).
32. D. Mohan, C. U. Pittman, M. Bricka, F. Smith, B. Yancey, J. Mohammad, P. H. Steele, M. F. Alexandre-Franco, V. Gómez-Serrano, H. Gong, *J. Colloid Interface Sci.*, **310**, 57 (2007).
33. R. Hamzenejad, E. Sepehr, A. Samadi, M. H. Rasouli Sadaghiani, H. Khodaverdiloo, *J. Environ. Stud.*, **43**, 401 (2017).
34. Y. Han, Y. Yin, H. Zhang, S. Sun, Z. Huang, Y. Deng, L. Bao, *J. Geosci. Environ. Prot.*, **12**, 59 (2024).

Bulgarian Chemical Communications, Volume 58, Special Issue A (pp. 44-48) 2026 DOI: 10.34049/bcc.58.A.SN-08

Air dose rate analysis and its relation with temperature and humidity

S. Nedkova, P. Atanasova*

Department of Materials Science, Burgas State University „Prof. Dr. Assen Zlatarov“, 1 Prof. Y. Yakimov Str., Burgas 8010, Bulgaria

Received: June 25, 2025; Revised: December 01, 2025

The research is based on gamma radiation background assessment of two different ecosystems for the period of seventeen consecutive months and its relation to air temperature and air humidity. The measurements of ambient dose equivalent rate (H*10), commonly referred to as “air dose rate” or gamma dose rate (GDR), at the eleven monitoring points in the two test fields –a river and a lake, located alongside the southern coastline of the Black Sea coast near Burgas, Bulgaria, were performed by a portable survey meter. At the same monitoring points air temperature and air humidity were measured. The research shows different correlations between the three variables at the lake and the river. For Karaagach river gamma air dose rate is negatively correlated with air temperature and positively correlated with air humidity while air temperature is positively correlated with air humidity. On the contrary, for Vaya lake gamma air dose rate is positively correlated with air temperature and positively correlated with air humidity, while air temperature is negatively correlated with air humidity. Gamma air dose rates are lower alongside the river banks, than alongside the lake because of the difference in water flow, depth, sediments development and anthropogenic impact.

Keywords: air dose rate, gamma background, ionizing radiation, Vaya lake, Karaagach river

INTRODUCTION

Gamma radiation is part of the environmental indicators, which form the area inhabited by the living organisms. Within the safe limits which usually describe a nature landscape distant from active ionizing radiation source, the gamma background could be also described as air dose rate building the so-called natural radiation background. Its name comes from the sources from which the natural radiation is emitted, which are mostly soil, rocks, cosmic radiation and elements naturally present in the environment. Terrestrial radiation comes from the radionuclides present in the earth's crust (primordial radionuclides), soil, rocks, water and air [1]. Primary radionuclides predominantly found in rock and soils are ^{238}U, ^{232}Th and ^{40}K. It is reported that contribution of radon is not significant for outdoor radiation [2], but for the present research, its presence defined by air temperature and air humidity is the main factor for the development of the gamma radiation levels. Excluding cosmic radiation from extraterrestrial sources, major radiation along the water objects’ bank comes from the nearby rocks at higher altitudes, river sediment and water whereas in plain areas the key radiation sources are soil, sediment and water [1].

The temperature and the humidity of the air are two of the air parameters, with most active influence on the physic-chemical processes in the environment. Their relation with the gamma radiation had been a subject of lots of measurements and analyses and it is a subject of the present research.

Gamma radiation and air temperature

Air temperature can cause fluctuations in gamma dose rate within the range of 0.018–0.0053 $\mu Sv.h^{-1}$ depending on the air temperature [3], but at the same time, higher temperatures might reduce radon levels, which could in turn decrease the dose rate [4]. The dose rate also tends to be lower in winter and higher in summer, which is attributed to changes in weather and soil conditions [5, 6].

Gamma radiation and air humidity

Relative humidity is usually positively correlated with gamma dose rate [3, 4], but could be also inversely correlated with air temperature, meaning that when the temperature rises, relative humidity typically decreases, and *vice versa* [3, 7]. Higher humidity levels are also associated with increased radon concentrations, which can contribute to higher dose rates [4].

The overall impact of meteorological parameters, including air temperature and air humidity, on natural radioactivity and dose rates is significant. These parameters can cause variations in the natural atmospheric radioactivity, which in turn affects the dose rates [4, 8].

* To whom all correspondence should be sent:
E-mail: *sabina_nedkova@abv.bg*

EXPERIMENTAL

The present study assesses the gamma radiation background values in two different ecosystems – a lake and a river for a period of seventeen consecutive months and seeks their relation with air humidity and air temperature values. The measurements of ambient dose equivalent rate (H*10) DER, commonly referred to as "air dose rate" were performed in two test fields – Lake Vaya and River Karaagach, located alongside the southern coastline of Black Sea coast. It is measured in μSv h^{-1}. A "Terra" dosimeter-radiometer MKS – 05 – a portable survey meter – Fig. 1, based on energy-compensated Geiger-Müller counter was used.

Fig. 1. "Terra" dosimeter-radiometer MKS – 05

It is designed to measure ambient dose equivalent and ambient dose equivalent rate of gamma radiation (or photon-ionizing radiation), with ±15 % accuracy in the gamma energy range from 0.05 MeV to 3 MeV –Fig. 1 [9]. It is designed for measurement of in the range of 0.001 to 9999 mSv. To measure the gamma/photon-ionizing radiation, the dosimeter was directed with its metrological mark "+" towards the examined area at the height of 1 m. The final values were obtained as an arithmetic mean of the five last measurements after the LCD of the survey meter stopped blinking. For the determination of gamma dose rate the monitoring area is determined roughly as a circle with radius of 1 meter and a center-the sampling point. Within the surveyed area around the sampling point, the radiological examination includes three points, for the operator to stop, to measure the background. The three locations (points) are placed approximately at the vertices of an equilateral triangle, with the center – the sampling point. The area thus formed is traversed at a speed of about 5-10 cm/s.

The gamma dose rate, the air temperature and air humidity were measured at the height of 1 m above the ground, at eleven monitoring points above land, lake and river banks within the two test fields. Six monitoring points were placed alongside the lake banks of the Vaya lake – Fig. 2a and five alongside Karaagach river – Fig. 2b.

Fig. 2a. Monitoring points alongside the banks of the Vaya lake

On the same monitoring points air temperature (specified in units of degrees Celsius (°C) and air humidity (specified in %RH). were measured. Air temperature and air humidity were measured with Humidity &Temperature meter. The air dose rate measurements were performed by the "Terra" dosimeter-radiometer MKS – 05.

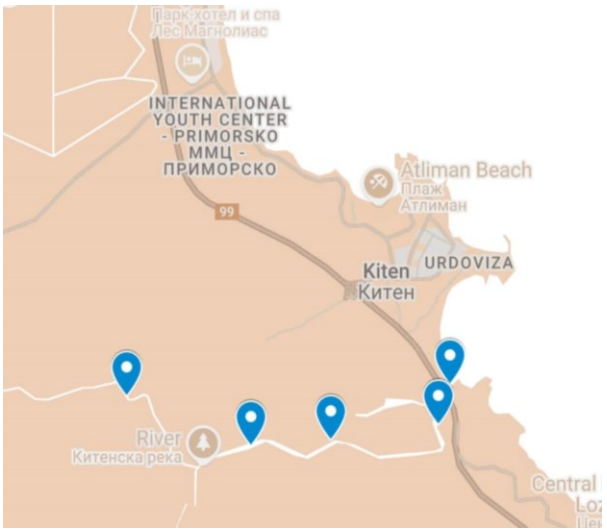

Fig. 2b. Monitoring points alongside Karaagach river

RESULTS AND DISCUSSION

Reliability of data

The reliability of the data gathered was analyzed and reported using Cronbach's α coefficient of an excellent value of 0.952, which indicates very high internal consistency among the measured items (gamma/air dose rate, air temperature and air humidity). Since some of the items have similar values (especially for gamma air dose rate), this value (α = 0.952) could also indicate that some items are very similar or overlapping in composition.

Mean values of gamma air dose rate

The mean values of gamma air dose rate of Karaagach river and Vaya lake are (MV Karaagach =0.1336, MV Vaya Lake=0.1538) – Fig. 3.

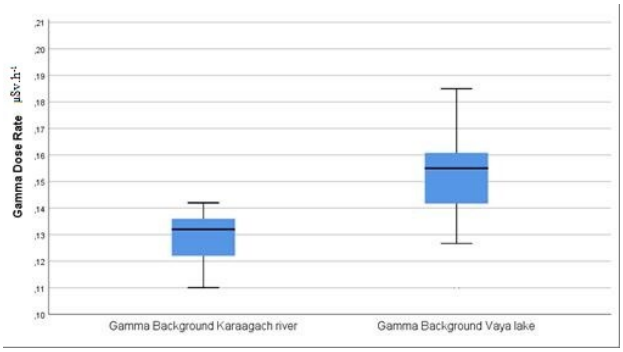

Fig. 3. Mean values of gamma air dose rate of Karaagach river and Vaya lake

It is seen that the average gamma dose rate alongside the river banks is by 15 % lower than that alongside the lake banks. Since we have only data on three environmental factors - gamma air dose rate, air humidity and air temperature, the possible explanation on that fact could be the radionuclide concentration at the monitoring points.

Vaya lake (also known as Burgas Lake), is the biggest natural lake in Bulgaria and the shallowest Black Sea costal lake. During the last decades Vaya lake has undergone significant changes due to different anthropogenic factors which disturb the water balance of the lake and lead to introduction of biogenic elements in the wetland with a negative effect on the chemical composition of the water with impacts on the flora and fauna of the aquatic ecosystem [10]. Its length is 9.6 km, its width is from 2.5 to 5 km, its area is 28 km^2, and its depth reaches 1.3 m. Vaya lake is located on the outskirts of the city of Burgas. It is subject to strong anthropogenic pressure due to its proximity to the densely populated city, large industrial facilities and complexes, as well as the unlimited and uncontrolled access of people outside the protected areas [11]. As an urban lake, Vaya lake's radionuclides may originate from atmospheric deposition, or anthropogenic sources. These radionuclides tend to settle in the still water, leading to higher concentrations near the lake bed and banks, which explains the higher mean values in gamma air dose rate.

Karaagach river, also known as Kitenska river, [12] is a 36 km long river in Burgas province in southeastern Bulgaria. Its maximum depth is 14 m and its basin size is 182 km^2. The depth, size, water flow and distance from direct anthropogenic sources makes Karaagach river different from Vaya lake. In that case, the lower gamma air dose rate could be a result of low radionuclide levels, more diluted due to the continuous river flow and the mobile nature of river sediments, which reduces their localized accumulation.

Correlation among items

The overall correlation between mean values of the items: (1.1) Gamma air dose rate Karaagach river, (1.2) Temperature Karaagach river, (1.3) Humidity Karaagach river, (2.1) Gamma air dose rate Vaya lake, (2.2) Temperature Vaya lake, (2.3) Humidity Vaya lake, assessed by Pearson correlation analysis (Table 1), shows that:

- *Eco system Karaagach River.* (1.1) Gamma air dose rate for Karaagach river is negatively correlated with (1.2) Temperature Karaagach and positively correlated with (1.3) Humidity Karaagach. (1.2) Temperature Karaagach is positively correlated with (1.3) Humidity Karaagach ($p<0.01$).
- *Eco system Vaya Lake.* (2.1) Gamma air dose rate Vaya lake is positively correlated with (2.2) Temperature Vaya lake and positively correlated with (2.3) Humidity Vaya lake, ($p<0.05$). (2.2) Temperature Vaya lake is negatively correlated with (2.3) Humidity Vaya lake.
- *Temperature and humidity.* The average air temperatures measured alongside the two water objects at the observed monitoring points are different. It could be seen from air temperatures' mean values, which are higher on the lake, than on the river (MV Vaya lake = 20.63°C and MV Karaagach river = 18.83 °C) – Fig. 4.

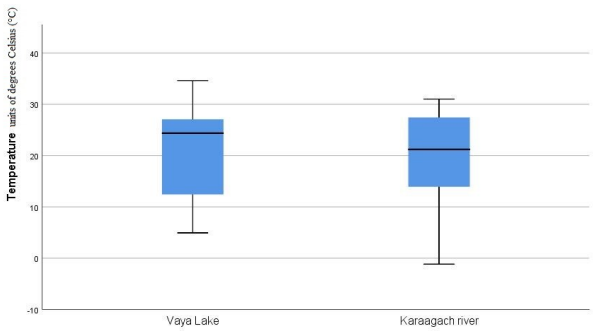

Fig. 4. Air temperature mean values alongside the lake and alongside the river

On the contrary, the difference in air humidity is reversed. According the mean values the air humidity values alongside the river are higher than the ones alongside the lake (MV Vaya lake = 51.33%RH and MV Karaagach river=54.17%RH) – Fig. 5.

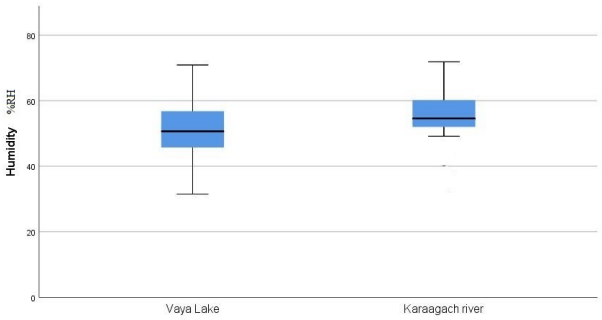

Fig. 5. Air humidity mean values alongside the river and the lake

That is seen by both the correlation analysis (Table 1) and the graphic depiction of the values in the observed months – Figs. 6a, 6b.

Table 1. Correlation amongst mean values of the items: (1.1) Air dose rate Karaagach river, (1.2) Temperature Karaagach, (1.3) Humidity Karaagach, (2.1) Air dose rate Vaya lake, (2.2) Temperature Vaya lake, (2.3) Humidity Vaya lake.

	1.1	1.2	1.3	2.1	2.2	2.3
1.1	1					
1.2.	–0.242	1				
1.3.	0.042	0.693**	1			
2.1.				1		
2.2.				0.019	1	
2.3.				0.484*	–0.039	1

*p<0.05, ** p<0.01

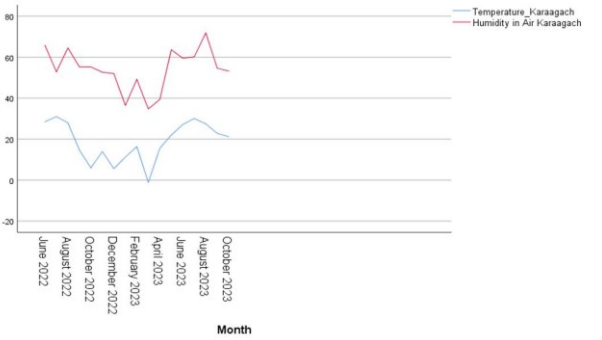

Fig. 6a. Temperature and air humidity values – Karaagach river for the period June 2022-October 2023 graphic view

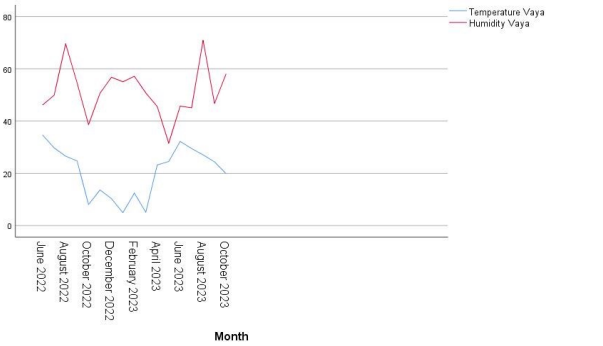

Fig. 6b. Temperature and air humidity values –Vaya lake for the period June 2022-October 2023 graphic view

We see that higher levels of humidity are related to lower gamma radiation values in Karaagach river. This could be explained by the absorption and attenuation of gamma rays by the water molecules in humid air. This attenuation results in lower measured gamma radiation levels. Near a river, when air temperature increases, the water temperature also often rises leading to increased evaporation. Higher evaporation adds moisture to the air, raising humidity levels. A lake, being smaller or more isolated, may experience different dynamics. During hot periods, the lake's water might quickly evaporate initially, increasing local humidity, but if the water level significantly drops, the surface area decreases, reducing ongoing evaporation.

Along the Karaagach river, as a larger water body, the continuous moisture source leads to a positive correlation between temperature and humidity. Along Vaya lake, the smaller or more isolated water body and moisture source leads to a negative correlation due to the higher air temperature and the rapid drying of air they cause.

CONCLUSIONS

The observed correlations between the items air dose rates and environmental factors (air temperature and air humidity) at different locations—river and lake—are influenced by a combination of physical and environmental factors, as well as by the sensitivity of the used dose rate meter.

The observed differences in gamma radiation dose rates alongside lake and river banks could be related with the different sediment accumulation patterns, water flow dynamics, anthropogenic impact, etc. Vaya lake's higher gamma dose rate might be due to the localized radionuclide concentrations alongside its banks because of sediment settling, leading to elevated gamma dose rates, whereas rivers' flowing waters of Karaagach river tend to disperse radionuclides, resulting in generally lower localized dose rates along its banks.

Higher levels of humidity are related to lower gamma radiation values in our research. This could be explained by the absorption and attenuation of gamma rays by the water molecules in humid air. This attenuation results in lower measured gamma radiation levels. Along the Karaagach river as a larger water body, the continuous moisture source leads to a positive correlation between temperature and humidity. Along Vaya lake, the smaller or more isolated water body and moisture source leads to a negative correlation due to the higher air temperature and the rapid drying of air, they cause.

***Acknowledgement**: The study was performed with the support of the project "Cross-border regions cooperate for BLUE GROWTH COLLABs", CB005.3.12.001, funded by the Interreg Program – IPA for cross-border cooperation Bulgaria – Turkey 2014-2020 (Interreg IPA Cross-border Cooperation Bulgaria – Turkey Program).*

REFERENCES

1. Sh. Prerna, K. Meher Prabodha, P. Mishra Kaushala, *Journal of Radiation Research and Applied Sciences*, **7**, 595 (2014).
2. N. Kavasi, J. Somlai, G. Szeiler, B. Szab I. Schafer, T. Kovacs, *Radiation Measurements*, **45**, 1068 e1071 (2010).
3. Y. Jung, Z. Shang-Guan, F. Zhao, M. Lin, X. Sha, D. Luo, Q. Chen, K. Peng, *Journal of Environmental Radioactivity*, **192**, 467 (2022).
4. R. Rabi, L. Oufni, *Radiation Physics and Chemistry* **139**, 40 (2017).
5. C. A. Baciu, *Journal of Radioanalytical and Nuclear Chemistry,* **268** (1), 3 (2006).
6. K. Kossert, S. Pommé, U. Stolzenberg, *Applied Radiation and Isotopes*, **210**, 18 (2024).
7. L. V. Allen Jr., R. McKenzie, A. Ron, E. S. Kastango, R. Kaestner, A. Rebelo, P. Burnside, G. Schultz, *International Journal of Pharmaceutical Compounding*, **14** (4), 284 (2010).
8. E. Simion, I. Mihalcea, F. Simion, C. Pacurar, *Revista de Chimie*, **63** (12), 1251 (2012).
9. Operating manual, MKS-05 "TERRA" dosimeter-radiometer (2020)
10. R. Dimitrova, E. Nenova, B. Uzunov, M. Shishiniova, M. Stoyneva, *Bulgarian Journal of Agricultural Science*, **20**, 165 (2014).
11. The birds in Bulgaria, website approached June 18th 2025, https://www.birdsinbulgaria.org/ovm.php?l=en&pageNum_Ovm_All=0&totalRows_Ovm_All=113&id=35
12. Scientific Information Center "Bulgarian Encyclopedia", 113 (2015).

Bulgarian Chemical Communications, Volume 58, Special Issue A (pp. 49-53) 2026 DOI: 10.34049/bcc.58.A.SN-09

Synthesis and physicochemical characterization of rhodium(III) hydrogenselenite

K. Todorova, V. Georgieva*, S. Genieva

Department of Chemistry, Burgas State University "Prof. Dr. Assen Zlatarov'', 1 Prof. Yakimov Str., 8010 Burgas, Bulgaria

Received: July 9, 2025; Accepted: November 09, 2025

The present study examines the hydrothermal approach for the synthesis of rhodium(III) hydrogenselenite, determining its structural features and potential functional properties. The precursors of the synthesis are rhodium trichloride trihydrate ($RhCl_3 \cdot 3H_2O$) and sodium hydrogenselenite ($NaHSeO_3$), in stoichiometric quantities, duration 100 hours and temperature 200°C. For good crystallinity of the product, additional hydrothermal treatment was performed in an optimal pH environment. Orange-brown crystalline phase with a probable chemical composition of rhodium hydrogenselenite ($Rh(HSeO_3)_3$) was obtained. Various physicochemical methods of analysis, including Fourier transform infrared spectroscopy (FTIR), X-ray diffraction (XRD), and ultraviolet-visible spectroscopy (UV-vis), were employed to elucidate the composition of the solid phases obtained.

Keywords: hydrothermal synthesis, rhodium oxoselenates, physicochemical analysis

INTRODUCTION

Platinum-group metals are distinguished by their exceptional catalytic properties, making them indispensable in various industrial and environmental applications [1–3]. These properties stem from their unique electronic configurations, particularly the partially filled d-orbitals, which enable the formation of diverse coordination environments and reaction pathways. The catalytic performance of these metals can be finely tuned by incorporating ligands with specific optical, magnetic, or biological functionalities, allowing precise control over reactivity, selectivity, and stability [4].

Among these, rhodium is particularly noteworthy for its versatility across multiple oxidation states (+I to +V), and its broad functional-group tolerance and high stability in aqueous environments [5–7]. Rhodium complexes, in particular, are widely employed in homogeneous catalysis for hydrogenation, hydroformylation, and hydrosilylation reactions [8–10]. These reactions are essential for the synthesis of fine chemicals and intermediates in the pharmaceutical and petrochemical industries [11, 12]. Beyond catalysis, rhodium-based compounds have garnered attention in medicinal and diagnostic research due to their ability to engage with specific biomolecular targets [13–15].

Recent studies have identified oxygen-containing selenium ions, such as selenite (SeO_3^{2-}) and selenate (SeO_4^{2-}), as effective and stable ligands that can enhance the structural adaptability and reactivity of metal complexes [16]. The combination of selenium-based ligands with rhodium creates opportunities to design novel coordination compounds with multifunctional properties relevant to catalysis, materials science, and therapeutics.

Rhodium oxoselenates, in particular, represent a relatively underexplored class of compounds that merge the complex coordination chemistry of rhodium with the diverse structural frameworks of selenium oxyanions. Their potential utility spans through heterogeneous catalysis, electrochemical systems, and functional materials with tunable electronic and magnetic properties. In higher oxidation states (+III to +V), rhodium forms structurally robust but synthetically challenging compounds that remain the subject of ongoing crystallographic and spectroscopic investigations [17–19].

Accordingly, the aim of the present study was to synthesize rhodium(III) hydrogenselenite and to perform comprehensive physicochemical characterization to evaluate its potential for future applications.

EXPERIMENTAL

Hydrothermal synthesis was conducted using rhodium trichloride ($RhCl_3$) and sodium hydrogenselenite ($NaHSeO_3$) in the following quantities: 1.06 g (5.05 mmol) $RhCl_3 \cdot 3H_2O$, 2.17 g (14.37 mmol) $NaHSeO_3$, and 20 ml (1111.11 mmol) H_2O. The synthesis was carried out at 200°C for 100 h in 50 ml stainless steel autoclaves with an internal Teflon coating. An orange-colored maternal solution containing a precipitate of deep orange color was

* To whom all correspondence should be sent:
E-mail: *velyana_topalska@btu.bg*

obtained. This precipitate was subsequently separated from the solution by decanting. After drying at 60°C, an orange-brown solid phase of $Rh(HSeO_3)_3$ was formed for a day (Fig. 1).

a

Fig. 1. Photograph of the product obtained in the system $RhCl_3 \times 3H_2O/NaHSeO_3$

Surface functional groups in the synthesized sample and output reagents were characterized using a Nicolet iS50 FT-IR spectrometer which detects characteristic absorption bands in the mid-infrared region (400–4000 cm^{-1}), corresponding to various valence and deformation vibrations of chemical bonds. Electronic transitions in the molecules were monitored using UV-vis spectroscopy. Spectra were recorded at room temperature with an Evolution 300 spectrophotometer operating in the wavelength range of 190 – 1000 nm. Spectralon was used as the reference standard. The phase composition of the samples was determined using a Bruker D8 Advance X-ray diffractometer with Cu K_α radiation (λ = 0.15406 nm) and a PW 2200 Bragg-Brentano θ/2θ goniometer. Diffraction patterns were collected over a 2θ range of 10–90°, with a step size of 0.033° and a counting time of 10.0 s per step. Phase identification was carried out using standard database patterns.

RESULTS AND DISCUSSION

The Fourier transform infrared spectra (FTIR) of the synthesized sample and of the output reactants in the reaction systems are presented in Fig. 2.

In the high-frequency region of the spectra (3600–3200 cm^{-1}), distinctive absorption bands are observed, corresponding to the stretching vibrations of O–H bonds in the studied compounds or in associated crystallization water. In the medium-frequency region of FTIR spectra (1630–1610 cm^{-1}), absorption peaks corresponding to deformation vibrations of O–H bonds were recorded. In the low-frequency region (1000–400 cm^{-1}), identified peaks were associated with the stretching vibrations of Se–O bonds in the SeO_3^{2-} ion and in the SeO_2 molecule [20–23].

In the FTIR spectrum of $NaHSeO_3$ (Fig. 2, spectrum 1), characteristic absorption bands are observed at 3451 cm^{-1} and 2429 cm^{-1}, corresponding to the symmetric stretching vibrations (ν_s) of H–O bonds. Bending vibrations (δ) of H–O bonds were detected at 1636 cm^{-1} and 1234 cm^{-1}. Bands at 890 cm^{-1}, 845 cm^{-1} and 823 cm^{-1} were attributed to symmetric stretching vibrations (ν_s) of the SeO_2 unit, while the band at 788 cm^{-1} corresponds to the asymmetric stretching vibration (ν_{as}) of Se–O. Additional bands at 614 cm^{-1}, 599 cm^{-1} and 429 cm^{-1} were assigned to O–Se–O bending (valence) vibrations [24–26].

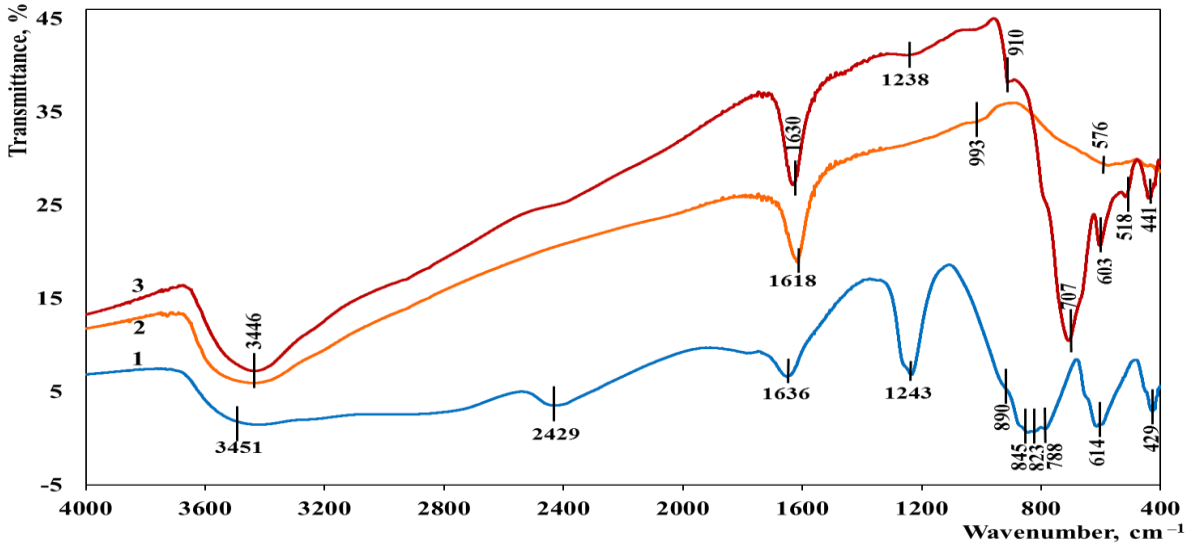

Fig. 2. FTIR spectra of: 1 – $NaHSeO_3$, 2 –$RhCl_3 \times 3H_2O$, 3 – $Rh(HSeO_3)_3$

$RhCl_3 \cdot 3H_2O$ (Fig. 2, spectrum 2) exhibits absorption bands at 3446 cm^{-1}, 1618 cm^{-1}, and 543 cm^{-1}, corresponding to the stretching and bending vibrations of O–H bonds from crystallization water. Additional bands attributed to the stretching and deformation vibrations of Rh–Cl bonds are observed below 400 cm^{-1} [27].

The FTIR spectrum of the synthesized compound $Rh(HSeO_3)_3$ (Fig. 2, spectrum 3) displays absorption bands corresponding to the stretching and bending vibrations of O–H bonds, observed at 3446 cm^{-1} and 1630 cm^{-1}, indicating the presence of crystallization water. Additional bands appear at 910 cm^{-1}, 707 cm^{-1}, 603 cm^{-1}, 518 cm^{-1} and 441 cm^{-1}. Several of these are shifted relative to the characteristic bands of $NaHSeO_3$, and were attributed to symmetric SeO_2 stretching (ν_s), asymmetric Se–O stretching (ν_{as}), and O–Se–O stretching vibrations (especially at 603 cm^{-1}). The bands at 518 cm^{-1} and 441 cm^{-1} were attributed to symmetric Se–OH stretching and bending vibrations, respectively, providing evidence for the presence of the hydrogenselenite ($HSeO_3^-$) ion [26].

UV–vis spectroscopy was employed to confirm the composition of the synthesized solid phase. The UV–vis spectra of the studied reaction system are shown in Fig. 3.

The UV–vis spectrum of $NaHSeO_3$ (Fig. 3) shows a high-energy absorption band with a maximum at 228 nm, corresponding to transitions at the highest energy level. In addition, a broad absorption band centered at 499 nm is observed. This band was attributed to a sodium-induced intraligand $\pi \rightarrow \pi^*$ transition, likely influenced by the filled p-electron configuration of the Na^+ ion [28]. The spectrum of the parent compound $RhCl_3 \times 3H_2O$ (Fig. 3) is characterized by a less intense band at 242 nm and a broad absorption band with a maximum at 549 nm.

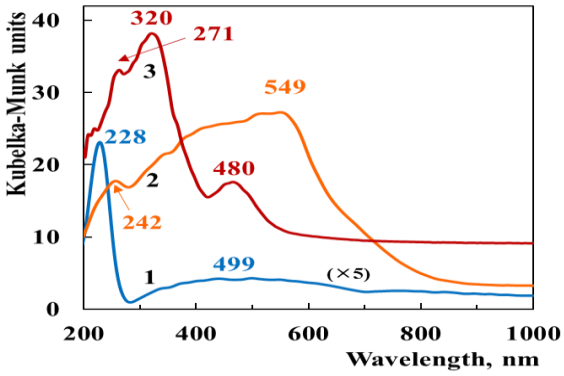

Fig. 3. UV-vis spectra of: 1 – $NaHSeO_3$, 2 – $RhCl_3 \times 3H_2O$, 3 – $Rh(HSeO_3)_3$

These features are consistent with ligand-to-metal charge transfer (LMCT) and d–d transitions typical of rhodium(III) complexes in octahedral coordination environments [29]. The UV–vis spectrum of the synthesized $Rh(HSeO_3)_3$ complex (Fig. 3) reveals three distinct and intense absorption bands at 271 nm, 320 nm, and 480 nm. The band at 320 nm corresponds to the highest energy transition in this compound. These absorption features are consistent with electronic transitions reported in other selenium- and rhodium-containing compounds [30], and are also comparable to transitions observed in certain organometallic rhodium complexes [31, 32]. The presence of strong absorption in both the UV and visible regions suggests that $Rh(HSeO_3)_3$ may have promising applications in photocatalysis and light-driven redox processes. Its electronic absorption profile, particularly the band at 480 nm in the visible range, indicates potential utility as a visible-light-responsive material. Such characteristics are desirable for the development of catalytic systems, light-activated sensors, or functional materials in optoelectronic devices [33, 34]. The compound's responsiveness to both UV and visible light also points to possible roles in environmental remediation technologies, such as photodegradation of organic pollutants or solar-driven water splitting.

In the X-ray diffraction (XRD) pattern of $NaHSeO_3$ (Fig. 4), intense diffraction peaks were recorded at 2θ values of 17.7°, 25.7°, 26.8°, 27.6°, 29.4°, 30.4°, 30.9°, 32.4°, 33.8°, 34.9°, 35.8°, 41.3°, 46.3°, and 54.4°, in agreement with the reference pattern ICSD 00-032-1088.

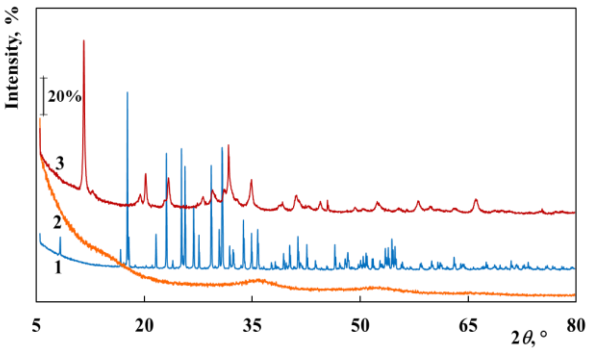

Fig. 4. X-ray diffraction pattern of: 1 – $NaHSeO_3$, 2 – $RhCl_3 \times 3H_2O$, 3 – $Rh(HSeO_3)_3$

The reference compound $RhCl_3 \times 3H_2O$ displayed an amorphous profile, with no distinct diffraction peaks detected (Fig. 2, 2). According to Zhou *et al.* [35], its main characteristic peaks are located at 9.49°, 36.75°, 52.75°, and 65.94°, further supporting the amorphous nature of the sample analyzed here. In contrast, the XRD pattern of the synthesized

$Rh(HSeO_3)_3$ compound (Fig. 4) exhibits well-defined reflections at 2θ values of 11.6°, 20.1°, 23.5°, 31.6°, and 34.9°. However, no corresponding phase was found in the ICSD database, suggesting the formation of a previously unreported crystalline phase. Ongoing efforts are focused on identifying an isostructural analogue to support the qualitative characterization of this new compound. Preliminary crystallographic analysis indicates that the compound crystallizes in the orthorhombic Pmmm space group, with unit cell parameters a = 15.149(3) Å, b = 13.694(2) Å, and c = 4.4028(1) Å. Further crystallization attempts, conducted at 200 °C in 0.2 M NaOH solution over a two-week period, did not alter the diffraction pattern, and no single crystals suitable for structure determination were obtained.

CONCLUSIONS

In this study, a new rhodium hydrogenselenite compound, $Rh(HSeO_3)_3$, was synthesized for the first time through a reaction between $RhCl_3{\times}3H_2O$ and $NaHSeO_3$ under mild hydrothermal conditions. The structure and composition of the product were investigated using FTIR, UV–vis spectroscopy, and X-ray powder diffraction (XRD).

FTIR spectroscopy confirmed the presence of hydrogenselenite ligands and crystallization water in the structure, as indicated by characteristic O–H and Se–OH vibrational bands. The UV–vis spectral profile of the compound revealed three distinct absorption bands at 271, 320, and 480 nm, corresponding to electronic transitions associated with both selenium and rhodium centers. The absorption in the visible region suggests that $Rh(HSeO_3)_3$ may be a suitable candidate for applications in photocatalysis, solar energy conversion, and photoresponsive materials.

XRD analysis of the synthesized material demonstrated a crystalline phase with clearly defined diffraction peaks not matching any known compound in the ICSD database, confirming the formation of a new phase. Preliminary crystallographic analysis suggests an orthorhombic crystal system with Pmmm symmetry and unit cell parameters a = 15.149(3) Å, b = 13.694(2) Å, and c = 4.4028(1) Å. Although prolonged crystallization under alkaline conditions at 200 °C did not yield single crystals suitable for full structural determination, the reproducibility of the diffraction pattern confirms the phase stability.

The successful synthesis and initial characterization of $Rh(HSeO_3)_3$ provide a basis for further structural and functional investigation. The compound's light absorption properties and the redox-active nature of both rhodium and selenium open avenues for its use in environmental remediation, catalytic hydrogenation, and sensor development. Future work will focus on optimizing crystallization conditions to enable single-crystal X-ray diffraction studies and exploring the compound's catalytic behavior under photochemical and electrochemical conditions.

REFERENCES

1. K. Nose, T. H. Okabe, in: Treatise Process Metall., Elsevier, UK, 2014, p. 1071.
2. A. E. Hughes, N. Haque, S. A. Northey, S. Giddey, *Resources*, **10**, 1 (2021).
3. H. Tang, Z. Peng, R. Tian, L. Ye, J. Zhang, M. Rao, G. Li, *J. Environ. Chem. Eng.*, **11**, 110237 (2023).
4. S. Swaminathan, P. Jerome, R. J. Deepak, R. Karvembu, T. H. Oh, *Coord. Chem. Rev.*, **503**, 215620 (2024).
5. Z. Wu, K. L. Hull, *Chem. Sci.*, **7**, 969 (2016).
6. J. Hansen, H. M. L. Davies, *Coord. Chem. Rev.*, **252**, 545 (2008).
7. S. Kim, S. Han, J. Park, S. Sharma, N. K. Mishra, H. Oh, J. H. Kwak, I. S. Kim, *Chem. Commun.*, **53**, 3006 (2017).
8. W. Gil, A. M. Trzeciak, *Coord. Chem. Rev.*, **255**, 473 (2011).
9. J. P. Morales-Cerón, P. Lara, J. López-Serrano, L. L. Santos, V. Salazar, E. Álvarez, A. Suárez, *Organometallics*, **36**, 2460 (2017).
10. S. Medici, M. Peana, A. Pelucelli, M. A. Zoroddu, *Molecules*, **26**, 2553 (2021).
11. Y. Wei, B. Rao, X. Cong, X. Zeng, *J. Am. Chem. Soc.*, **137**, 9250 (2015).
12. P. Govender, S. Ngubane, B. Therrien, G. S. Smith, *J. Organomet. Chem.*, **848**, 281 (2017).
13. J. Bianga, N. Kopplin, J. Hülsmann, D. Vogt, T. Seidensticker, *Adv. Synth. Catal.*, **362**, 4415 (2020).
14. M. C. Simpson, D. J. Cole-Hamilton, *Coord. Chem. Rev.*, **155**, 163 (1996).
15. P. Peng, B. U. Xianhui, N. Zheng, *Acc. Chem. Res.*, 38, 293 (2005).
16. M. S. Wickleder, C. Logemann, in: Handbook of Chalcogen Chemistry: New Perspectives in Sulfur, Selenium and Tellurium, F. Devillanova, W.-W. Du Mont (eds.), Royal Society of Chemistry, Cambridge, UK, 2013, p. 307.
17. D. L. Ma, M. Wang, Z. Mao, C. Yang, C. T. Ng, C. H. Leung, *Dalt. Trans.*, **45**, 2762 (2016).
18. M. Sohrabi, M. Saeedi, B. Larijani, M. Mahdavi, *Eur. J. Med. Chem.*, **216**, 113308 (2021).
19. S. J. Thompson, M. R. Brennan, S. Y. Lee, G. Dong, *Chem. Soc. Rev.*, **47**, 929 (2018).
20. V. P. Verma, *Thermochim. Acta*, **327**, 63 (1999).
21. D. M. Calderón, U. Morales, C. Velásquez, V. H. Lara, L. Salgado, *Catal. Letters*, **132**, 268 (2009).
22. A. D. Allen, T. Theophanides, *Can. J. Chem.*, **42**, 1 (1964).
23. O. Janson, W. Schnelle, M. Schmidt, Y. Prots, S. L. Drechsler, S. K. Filatov, H. Rosner, *New J. Phys.*, **11**, (2009).

24. J. Stangret, T. Gampe, *J. Phys. Chem. A*, **106**, 5393 (2002).
25. L. Eklund, I. Persson, *Dalt. Trans.*, **43**, 6315 (2014).
26. J. Kretzschmar, N. Jordan, E. Brendler, S. Tsushima, C. Franzen, H. Foerstendorf, M. Stockmann, K. Heim, V. Brendler, *Dalt. Trans.*, **44**, 10508 (2015).
27. K. V. Yusenko, A. S. Sukhikh, W. Kraus, S. A. Gromilov, *Mol. 2020,* **25***,* 768 (2020).
28. S. Sutradhar, S. Basak, D. Das, B. Nath Ghosh, *Polyhedron*, **236**, 116344 (2023).
29. D. B. Vasilchenko, S. N. Berdyugin, S. V. Korenev, S. O'Kennedy, W. J. Gerber, *Inorg. Chem.*, **56**, 10724 (2017).
30. A. P. Ginsberg, W. E. Lindsell, C. R. Sprinkle, K. W. West, R. L. Cohen, *Inorg. Chem.*, **21**, 3666 (1982).
31. W. L. Su, Y. Cheng Yu, M. Ching Tseng, S. P. Wang, W. L. Huang, *J. Chem. Soc. Dalt. Trans.*, 3440 (2006).
32. T. Vadivel, M. Dhamodaran, S. Kulathooran, S. Kavitha, K. Amirthaganesan, S. Chandrasekaran, N. Ilayaraja, S. Senguttuvan, *Carbohydr. Res.*, **487**, 107878 (2020).
33. X. Cheng, D. Li, B. Yang, Y. Lin, L. Gong, *Chinese J. Org. Chem.*, **42**, 3335 (2022).
34. F. Camara, T. Gavaggio, B. Dautreppe, J. Chauvin, J. Pécaut, D. Aldakov, M.-N. Collomb, J. Fortage, *Molecules*, **27**, 6614 (2022).
35. W. Zhou, J. Yi, J. Lin, S. Fang, X. Peng, *Res. Chem. Intermed.*, **43**, 3651 (2017).
36. R. E. Morris, W. T. A. Harrison, G. D. Stucky, A. K. Cheetham, *J. Solid State Chem.*, **94**, 227 (1991).

Bulgarian Chemical Communications, Volume 58, Special Issue A (pp. 54-58) 2026 DOI: 10.34049/bcc58.A.SN-10

Kinetic study of the pyrolysis of chitosan-zeolite composite

K. Zafirova[1], D. Zvezdova[2*]

[1]*Medical University "Prof. Dr. Paraskev Stoyanov", Faculty of Pharmacy, Varna, Bulgaria*
[2]*Burgas State University "Prof. Dr, Assen Zlatarov", Faculty of Public Health and Health Care, Burgas, Bulgaria*

Received: September 04, 2025; Revised: December 01, 2025

Decomposition thermal analysis of chitosan-zeolite composite was carried out. The decomposition of the complex solid phase was studied using non-isothermal thermogravimetry. A complex optimization criterion for most accurate decomposition was developed. The data obtained on the basis of the complex method and complex criteria showed that most relevant is the separation of the complex process into three sub-processes. The advantage of the direct complex thermogravimetry method compared to other methods was shown. The results of the decomposition identification were analyzed.

Keywords: Chitosan–zeolite composite, pyrolysis, kinetics

INTRODUCTION

The first applications of chitosan (CS) have been in food and nutrition, material science, pharmacology, cosmetology, medicine, agriculture, and water treatment [1-4]. Chitosan is a polysaccharide corresponding to linear copolymers of 2-amino-2-deoxy-D-glucan and 2-acetamido-2-deoxy-D-glucan linked by a β-(1-4), which can be found in the exoskeletons of crustaceans and insects and in the cell walls of fungi and microorganisms [5]. Its main derivative, chitosan, obtained by deacetylation of CS, consists of the randomly distributed β-(1-4)-linked D-glucosamine (deacetylated unit) and N-acetyl-D-glucosamine (acetylated unit). CS contains a low amount of 2-amino-2-deoxyglucose and hence it is less soluble in acidic solvents, whereas CS contains a smaller amount of N-acetyl-2-amino-2-deoxy-D-glucose and is therefore soluble in acidic solvents [6-8]. The deacetylation process consists of the removal of the acetyl groups from the CS molecular chain, leaving behind a complete amino group (NH_2). The properties of CS are closely linked to the chemical reactivity of these amino groups, for example, their protonation in acidic medium leads to antifungal or antimicrobial activities, since cations can bend to the anionic sites in proteins.

CSZ (chitosan-zeolite) is the most studied composite of chitosan [9, 10]. It has been shown that the nanocomposite has improved properties, such as mechanical strength, gas barrier, and thermal stability, compared to pure CS [11]. This was related to the excellent dispersion of the nanoclay and its strong interaction with the CS matrix.

Whatever the method used, these polymers have a certain limitation in many engineering applications due to their low mechanical properties, moisture resistance, and thermal stability. These limitations are overcome by the recent development of a new class of materials, named biocomposite/ bionanocomposite materials, in which these biopolymers have been used as a matrix [12]. Unlike other nanofillers, biopolymer/clay biocomposites have been widely studied and applied in several research fields, because clays are available, cheap, and their intercalation chemistry is well-known [13, 14]. Thermal behavior can be studied by using certain physicochemical techniques, including DSC (differential scanning calorimetry), TGA (thermogravimetric analysis), DTG (differential thermal analysis), DMA (dynamic mechanical analysis), and other thermal analysis methods. Thermogravimetric analysis (TGA/DTA) has been widely used by many authors to study the kinetics of thermal degradation under isothermal and dynamic conditions, both in air and in nitrogen.

In most cases, the data can be used to determine the degradation mechanism and kinetic triplet evaluation (*E*a: activation energy, A: preexponential factor, conversion function). This value has been linked to the presence of intermolecular and intramolecular hydrogen bonds in the CS structure and to the diffusion phenomenon.

The literature lacks scientific studies addressing the pyrolysis kinetics of chitosan–zeolite composite materials. Consequently, the present research focuses on determining the kinetic parameters governing the thermal degradation of these structural composites.

* To whom all correspondence should be sent:
E-mail: *zvezdova@abv.bg*

METHODOLOGY

The thermogravimetric experiments were performed on the STA 449 F3 Jupiter complex thermal analysis apparatus (Netzsch - Germany). Experimental data were obtained for the temperature range of 293.15-1073.15 K at four heating rate settings β = 4.0, 6.0, 9.0 and 12.0 deg min^{-1}. The sample masses were about 5 mg. The purging was carried out with artificial air at a rate of 20 ml min^{-1}. Data from 1000 points were collected for each experiment at intervals of 0.1 s. Each point included time data from the beginning of the experiment, TG, DTG and DSC data. The experimental data were filtered with a two-way filter.

The quality of decomposition, for all experiments collectively and for each individual experiment, was evaluated using the relative error:

$$\gamma = \frac{A^{\text{calc}} - A^{\text{exp}}}{A^{\text{exp}}_{\text{max}} - A^{\text{exp}}_{\text{min}}} 100, \% \qquad (1)$$

where A represents the degree of conversion α, the rate of conversion with respect to time dα/dt or with respect to temperature dα/dT.

The results of the non-isothermal analysis of a chitosan sample for β=12 deg min^{-1} are shown in Fig. 1. The thermogravimetric (TG) analysis indicates that the process consists of three main stages of mass loss.

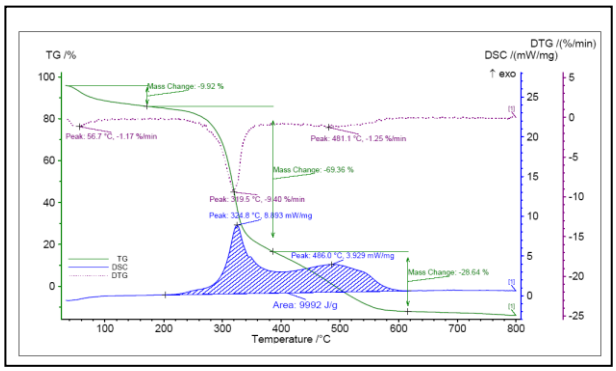

Fig. 1. TG, DTG and DSC curves of CSZ composite obtained at β=12 deg min^{-1}

Chitosan (CS) was extracted from Black Sea crab shells through standard chemical treatment involving demineralization with hydrochloric acid, deproteinization with sodium hydroxide, and deacetylation in concentrated alkali solution. Before the preparation of nanocomposites, the CS matrix was dissolved in a 1% (v/v) solution of acetic acid, and the filler (Z) was swollen in H_2O under magnetic stirring for 30 min.

For the experimental TG data of chitosan derived from Black Sea crabs, a pseudo-isoconversional analysis was performed using both differential and integral approaches, revealing that the former one exhibits higher sensitivity. Optimal parameters for Distributed Activation Energy Model (DAEM) identification were obtained through the comprehensive approach for the conversion range of $0.1 \leq \alpha \leq 0.9$. For each of the identified and parameterized subprocesses, thermal parameters—including the changes in entropy (ΔS), enthalpy (ΔH), Gibbs free energy (ΔG), and others—were calculated and evaluated. Owing to the good adequacy of the results, this approach was applied in our investigations of products and processes involving chitosan [15].

TG and DSC studies were conducted in the temperature range of 293.15-1073.15 K. For all membranes, three main peaks of mass loss were observed, the first peak (328.85 K) resulting from water loss. This stage is endothermic and occurs from the start of heating up to 393.15 K, with a mass loss of 9.92%, consisting mainly of water physically adsorbed on the surface of the material. This process was not of interest in the present study. The second (653.15 K) and the third (788.15 K) peak correspond to sample degradation. In general, intermolecular and intramolecular hydrogen bonding can contribute to increasing the thermal stability of the membrane. In the second main stage, degradation processes of CSZ take place, with a mass loss of 68.36%, ending at approximately 653.15 K. It is attributed to further deacetylation, cleavage of glycosidic bonds, and the subsequent oxidation of the residues. In the third stage, the mass of the sample begins to change at a slower rate and ends at approximately 1124.15 K with a mass loss of 28.64%. This peak indicates the occurrence of oxidation processes and corresponds to the CS decomposition reactions and the formation of volatile compounds formed by oxidation of carbon residues.

DSC analysis shows that the homogeneous nature of CS and zeolite yields relatively pronounced endothermic peaks. An increase in the endothermic peak is observed upon the introduction of zeolite. This result indicates that CSZ membranes are more stable at high temperatures in comparison to those from crab CS.

The holographs of the α–T and v_α–T lines (where v_α ≡ dα/dτ) after filtering the TG data are shown in Fig. 2. The figure does not display the stage of evaporation of adsorbed water nor the probable oxidation process above 1123.15 K, as these are beyond the scope of the present study. The uniform shift of the dependencies between the degree of conversion α and temperature T, and between the conversion rate v_α and T with increasing heating rate β are clear indicators of data's validity. The nature

of the curves suggests that the complex process consists of two or more subprocesses.

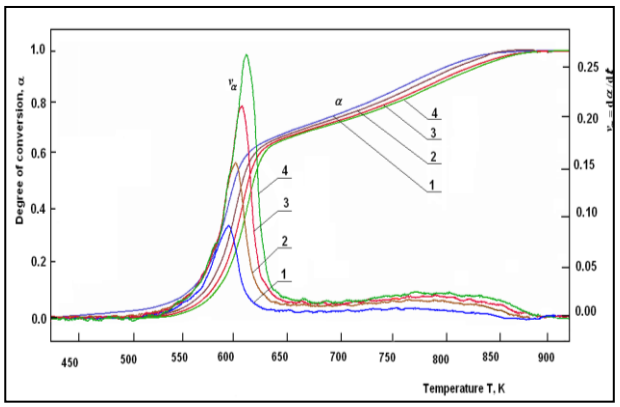

Fig. 2. Change in the degree of conversion and the rate of conversion with temperature (1, 2, 3, 4 correspond to heating rates β = 4, 6, 8, and 12 °C/min, respectively).

Similar conclusions can be drawn from the graphs in Fig. 1.

Identification and parameterization were performed using appropriate software [16]. The process was carried out with TG data from the range $0.0000 \le \alpha \le 1.0000$ and included 970 evenly spaced points along the α–T curves [16]. The instantaneous heating rates were taken into account.

New formulas were used for calculating the Arrhenius criterion [16]. A complex criterion was applied to evaluate the quality of the decomposition analysis, which is a function of the standard deviations of the conversion degree α and its rate with respect to time or temperature. Kinetic analysis was conducted with different numbers of subprocesses (Sp). The results of the kinetic analysis are presented in Table 1.

Table 1 shows that the most adequate results are obtained for decomposition involving three subprocesses, described by the kinetic models F1(α) [A1(α)], D5(α), Ap(α) with differential f(α) and integral g(α) forms, respectively:

$$f_{A_1}(\alpha) = (1-\alpha)\cdot \qquad g_{A_1}(\alpha) = -\ln(1-\alpha);$$
$$f_{D_5}(\alpha) = (3/2)(1-\alpha)^{4/3}\left[(1-\alpha)^{-1/3}-1\right]^{-1},$$
$$g_{D_5}(\alpha) = \left[(1-\alpha)^{-1/3}-1\right]^2; \qquad (2)$$
$$f_{Ap}(\alpha) = P(1-\alpha)[-\ln(1-\alpha)]^p$$
$$g_{Ap}(\alpha) = \frac{[-\ln(1-\alpha)]^p}{P(1-p)}; \qquad P = \left|\frac{1}{p-1}\right|$$

Table 1. Results from identification by a complex method for thermal degradation of CSZ

Result \ Process	Sub-process 1	Sub-process 2	Sub-process 3
Type of model	D5	Ap	A1
Activation energy, E_a (kJ/mol)	176321.4	70072.73	312112.7
Preexponential factor A (1/min)	6.0713E +10	389750.3	9.0454E +26
Exponent	-	0.453603	-
Weight coefficient	0.328998	0.375598	0.295404

Global best complex criteria	0.00018
R^2 (α)	0.99901
R^2 dα/dt	0.9915
Standard deviation - α	0.011204
Standard deviation - dα/dt	0.008175

From the experimental TG data, the activation energies E and the pre-exponential factor A were calculated for various evenly distributed conversion degrees from 0.1 to 0.9. The formulas from the FWO method were used:

$$\frac{d\alpha}{dt} = A(\alpha)f(\alpha)\exp\left(\frac{E(\alpha)}{RT}\right) \qquad (3)$$

The activation energy (Ea) can be obtained from the plot of log β against $1/T$ for a fixed degree of conversion, since the slope of such line is given by -0.4567 Ea/R. The preexponential factor, A can be obtained from the equation:

$$A = \frac{-\beta E_0}{RT_{max}^2 f'(\alpha_{max})}\exp\left(\frac{E_0}{RT_{max}}\right) \qquad (4)$$

The graphical dependencies for the calculations by the FWO method are shown in Fig. 3. For both products, the obtained results exhibit a high correlation coefficient.

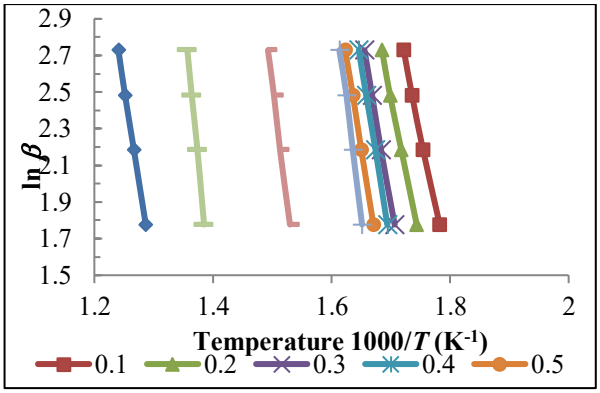

Fig. 3. Plots of ln β *vs.* 1000/T for the thermal degradation of CSZ composite at different conversion rates α (FWO method).

Table 2. Kinetic parameters obtained for CS and CSZ using FWO methods

	CSZ			CS		
α	E_a (KJ/mol)	A (1/min)	R	E_a (KJ/mol)	A (1/min)	R
0.1	386.66	7.43×10^{25}	0.9972	284.31	7.43×10^{25}	0.9982
0.2	349.34	1.51×10^{26}	0.9987	294.07	1.518×10^{26}	0.9991
0.3	362.99	7.65×10^{29}	0.9982	341.33	7.664×10^{29}	0.9993
0.4	421.79	2.10×10^{31}	0.9952	359.99	2.191×10^{31}	0.9997
0.5	385.75	5.43×10^{31}	0.9967	369.55	5.43×10^{31}	0.9997
0.6	331.14	1.20×10^{35}	0.9952	407.49	1.20×10^{35}	0.9963
0.7	315.30	1.44×10^{35}	0.9969	420.96	1.44×10^{35}	0.9988
0.8	323.31	1.37×10^{23}	0.9970	325.49	1.37×10^{23}	0.9989
0.9	326.95	2.59×10^{24}	0.9982	374.48	2.59×10^{24}	0.9997

The existence of multisteps in the thermal degradation curves of nanocomposites indicates: (1) the thermal stability of CS in the nanocomposites depends on the interactions of CS with Z [17-21], and (2) the thermal degradation of CS in the nanocomposites follows a complex reaction path (Table 2).

The activation energy *E*a of the chitosan-zeolite composite increases up to a conversion degree of α = 0.7 after which it remains relatively constant. A similar trend is observed for the pre-exponential factor A.

CONCLUSIONS

Differential thermogravimetric and thermal analysis (TGA/DTA) experiments were carried out to compare the thermal stability of the samples studied, and to determine the kinetic parameters involved in their degradation process, such as the activation energy (*E*a) of degradation, the frequency factor (*A*), and the degradation mechanism, known as *the kinetics triplet*.

The studies performed and the results obtained give us sufficient information about the thermal properties of CSZ composite and its stability. Its properties such as hydrophilicity, biocompatibility, biodegradability, antibacteriality, non-toxicity and adsorptivity make it an excellent material in the preparation of medical products. The kinetic properties determined during its thermal decomposition can be used in the development of technologies for its processing. The studies carried out can be used in the preparation of bandage materials with defined properties.

It was established that this kinetics model could be used for a quantitative description of the non-isothermal decomposition process of samples, which corresponds to a random scission mechanism.

REFERENCES

1. S. Olivera, H. B. Muralidhara, K. Venkatesh, V. K. Guna, K. Gopalakrishna, K. Yogesh, Kumar, *Carbohydr. Polym.*, **153**, 600 (2016). DOI: 10.1016/j.carbpol.2016.08.017
2. M. Vakili, M. Rafatullah, B. Salamatinia, A. Z. Abdullah, M. H. Ibrahim, K. B. Tan, Z. Gholami, P. Amouzgar, *Carbohydr. Polym.*, **113**, 115 (2014). DOI: https://doi.org/10.1016/j.carbpol.2014.07.007
3. H. Moussout, H. Ahlafi, M. Aazza, C. El Akili, *Int. J. Biol. Macromol*., **108**, 1063 (2018). DOI: https://doi.org/10.1016/j.ijbiomac.2017.11.018
4. H. Moussout, H. Ahlafi, M. Aazza, O. Zegaoui, C. El Akili, *Water Sci. Technol*., **73 (**9), 1199 (2016). DOI: 10.2166/wst.2016.075
5. H. Moussout, H. Ahlafi, M. Aazza, C. Sekkate, *Cellulose*, **25**, 5593 (2018). DOI:10.1007/s10570-018-1999-5
6. A. Anitha, S. Sowmya, P. T.S. Kumar, S. Deepthi, K. P. Chennazhi, H. Ehrlich, H. Ehrlich, M. Tsurkan, R. Jayakumar, *Prog. Polym. Sci.,* **39**, 1644 (2014). DOI: https://doi.org/10.1016/j.progpolymsci.2014.02.008
7. E. Khor, L. Y. Lim, *Biomaterials*, **24**, 2339 (2003). DOI: https://doi.org/10.1016/S0142-9612(03)00026-7
8. V. K. Thakur, S. I. Voicu, *Carbohydr. Polym.*, **146**, 148 (2016). DOI: 10.1016/j.carbpol.2016.03.030

9. P. Gogoi, A., Thakur, R. R. Devi, B. Das, T. K. Maji, *J. Environ. Chem. Eng*., **4**, 4248 (2016). DOI:10.1016/j.jece.2016.09.027
10. S. Noori, M. Kokabi, Z.M. Hassan, *Procedia Mater. Sci*., **11**, 152 (2015) DOI:10.1016/j.mspro.2015.11.023
11. H. Moussout, H. Ahlafi, M. Aazza, A. Amechrouq, *Thermochim. Acta*, **668**, 169 (2018). DOI: https://doi.org/10.1016/j.tca.2018.08.023
12. A. Ali, S. Ahmed, *Int. J. Biol. Macromol*., **109**, 273 (2018). DOI: https://doi.org/10.1016/j.ijbiomac.2017.12.078
13. E. M. S. Azzam, G. Eshaq, A. M. Rabie, A. A. Bakr, A. A. Abd-Elaal, A. E. El Metwally, S. M. Tawfik, *Int. J. Biol. Macromol*., **89**, 507 (2016). DOI: 10.1016/j.ijbiomac.2016.05.004
14. D. T. Zvezdova, N. M. Nedelchev, *Science & Technologies, Technical studies,* **II** (4), 15-(2012)
15. D. T. Zvezdova, *J. Therm. Anal. Calorim*., **149** (14), 7355 (2024). DOI:10.1007/s10973-024-13338-7
16. T. Ozawa, *Bull. Chem. Soc. Jpn*., **38**, 1881 (1965). DOI:10.1007/s10973-012-2882-5
17. I. Corazzari, R. Nistico, F. Turci, M. G. Faga, F. Franzoso, S. Tabasso, G. Magnacca, *Polym. Degrad. Stab*., **112**, 1 (2015). DOI:10.1016/j.polymdegradstab.2014.12.006
18. C.-Y. Ou, C. H. Zhang, S. D. Li, L. Yang, J.-J. Dong, X. L. Mo, M. Zeng, *Carbohydr. Polym.*, **82**, 1284 (2010). DOI: https://doi.org/10.1016/j.carbpol.2010.07.010
19. M. R. Ricciardi, V. Antonucci, M. Giordano, M. Zarrelli, *J. Fire Sci*., **30**, 318 (2012). DOI:10.1177/0734904112439293
20. S. Sinha Ray, *Env. Friendly Polym. Nanocomp*., 295 (2013). DOI:10.1533/9780857097828.2.295

Bulgarian Chemical Communications, Volume 58, Special Issue A (pp. 59-64) 2026 DOI: 10.34049/bcc.58.A.SN-11

Comparative study of the textural properties of chitosan, zeolite and their composite membrane

K. Zafirova[1], L. Gonsalvesh[2], D. Zvezdova[3*]

[1]*Medical University "Prof. Dr. Paraskev Stoyanov", Faculty of Pharmacy, Varna, Bulgaria*
[2]*Burgas State University "Prof. Dr. Assen Zlatarov", Faculty of Natural Sciences, Burgas, Bulgaria*
[3]*Burgas State University "Prof. Dr. Assen Zlatarov", Faculty of Public Health and Health Care, Burgas, Bulgaria*

Received: September 04, 2025; Revised: November 11, 2025

A comparative analysis was conducted to evaluate the textural properties of chitosan, zeolite and their composite membrane based on nitrogen adsorption data. Zeolite exhibited the highest specific surface area (25 m^2/g) and total pore volume (0.0964 cm^3/g), while chitosan showed limited porosity with predominantly mesoporous structure. The composite membrane demonstrated intermediate characteristics (5 m^2/g, 0.0238 cm^3/g), reflecting a successful structural integration that enhances its functional performance relative to the individual components.

Keywords: Chitosan–zeolite composite membrane, Porosity, FTIR, SEM

INTRODUCTION

Chitosan (CS), a polycationic biopolymer and waste product from seafood processing industry, is the second most abundant natural polysaccharide after cellulose. Some of the most noted properties of CS are biocompatibility, biodegradability, non-toxicity, adsorption properties, etc. In medical field, chitosan films have been tested as curative wound dressing and as scaffolds for tissue and bone engineering [1]. However, CS has low mechanical properties and is soluble in acidic media, which limits its application as an adsorbent at low pH [2]. In order to overcome these limitations, physical and chemical modification needs to be carried out on chitosan by its immobilization on a low-cost material such as zeolite. The combination of zeolite with a polymer backbone was found to lead to improved strength and heat resistance [3].

Studies have been conducted on the textural characteristics, characterization methods, and specific surface area values of porous materials derived from various sources for obtaining chitosan and its composite structures [4-8].

Over the last decades, biopolymer–zeolite hybrid materials which are known to combine physical and chemical properties of both inorganic and organic materials have gained increasing attention in the areas of science and technology of biopolymer-based advanced materials [9-13]. Infection by pathogenic microorganisms remains a major challenge in wound treatment. Natural polymers such as chitosan exhibit broad-spectrum antibacterial activity making them suitable for wound dressings. However, their low mechanical strength and water-retention capacity limit practical use. Zeolites, microporous aluminosilicates with ion-exchange capacity and antimicrobial potential, have been proposed as reinforcing agents to improve the performance of biopolymer-based materials. This material appears as a promising support due to its mechanical strength and chemical stability, low cost, and availability [9].

CSZ composites have been used in medical fields [14, 15]. It is well known that a surface interaction between CS and Z induces changes in microstructure morphology and surface chemistry, which are fundamental in adsorption processing, and for drug delivery process. Their combination with chitosan represents a promising strategy to enhance material properties through complementary interactions. This study presents a comparative analysis of the porous structure of chitosan, zeolite and a chitosan–zeolite composite membrane, aiming to evaluate the influence of composition on textural parameters.

EXPERIMENTAL

Chitosan (CS) was extracted from Black Sea shrimp shells through standard chemical treatment involving demineralization with hydrochloric acid, deproteinization with sodium hydroxide, and deacetylation in concentrated alkali solution. Natural zeolite (Z), identified as clinoptilolite, was used as received.

The procedure involves the preliminary preparation of a chitosan–zeolite (CSZ) membrane by combining a 1% chitosan solution (prepared by

* To whom all correspondence should be sent:
E-mail: *zvezdova@abv.bg*

dissolving 1 g of chitosan in 100 mL of 1% acetic acid at 52°C under continuous magnetic stirring for 24 h) with a 0.5% aqueous zeolite (clinoptilolite) suspension. The resulting chitosan–zeolite mixture was subsequently poured into Petri dishes and dried at 60°C to obtain uniform membranes.

Porous structure characterization was carried out using nitrogen adsorption isotherms at 77 K on a Surfer apparatus (Thermo Scientific). Specific surface area was calculated *via* the BET method (ISO 9277:2010). Total pore volume was obtained from the desorption branch at P_i/P_0 = 0.95, while micropore volume was evaluated using the Dubinin-Radushkevich equation. Pore size distribution was determined by applying NLDFT using the n2si77K_cyl kernel (ISO 15901-3:2007).

RESULTS AND DISCUSSION

Scanning electron microscopy (SEM) studies were carried out on the surfaces of chitosan (CS) and chitosan/zeolite nanocomposite films (CSZ). For the SEM analyses, in order to ensure sample conductivity, the specimens were gold-coated using a standard metallization procedure. The surface morphology of the CSZ films, as well as the mechanophysical structure of the studied materials, is presented in Figures 1 and 2.

The rough, uneven surface of the CSZ film may be due to loosely bound zeolite particles that were not fully and evenly dispersed within the formed nanocomposite film, owing to their poor solubility in water. The samples were examined using a scanning electron microscope (SEM) equipped with an X-ray microanalyzer (XMA). Digital micrographs in secondary electron mode were taken during the observations. The results of the surface examinations are presented in Figs. 1–5.

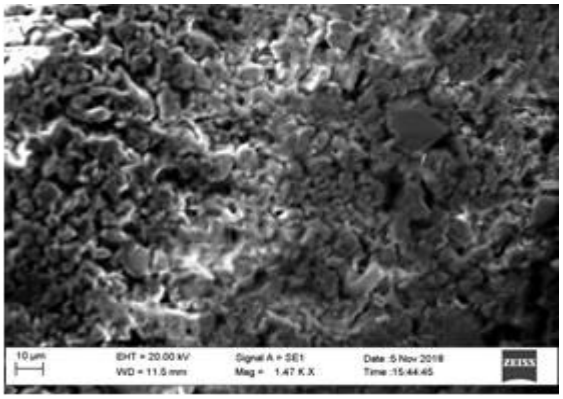

Fig. 1. Surface of a chitosan/ zeolite nanocomposite biofilm (×1470)

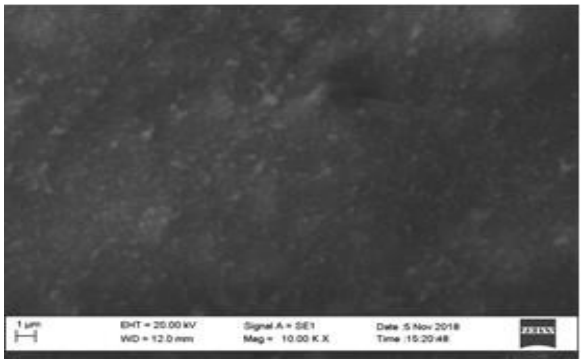

Fig. 2. Surface of a pure chitosan biofilm (×10,000)

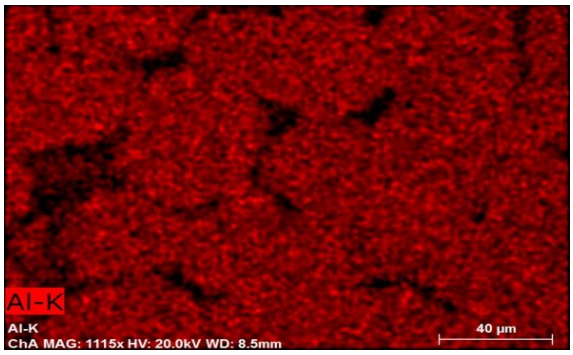

Fig. 3. Distribution of aluminum over the area, XMA, characteristic X-ray radiation – Al Kα

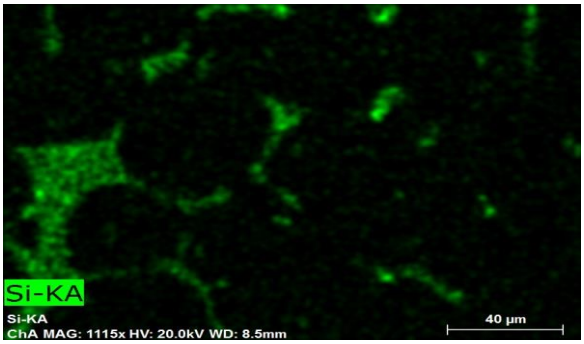

Fig. 4. Distribution of silicon over the area, XMA, characteristic X-ray radiation – Si Kα

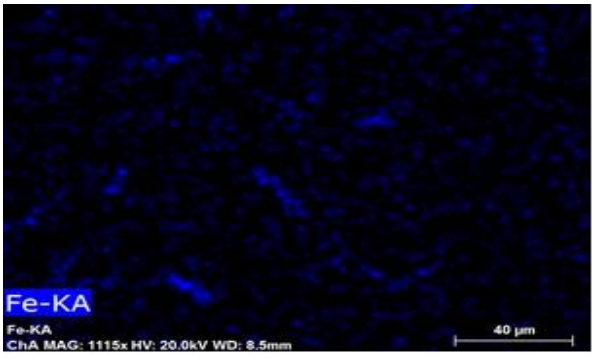

Fig. 5. Distribution of iron over the area, XMA, characteristic X-ray radiation – Fe Kα

In the samples of the chitosan/zeolite nanocomposite biofilm and the pure chitosan biofilm, two distinct types of surface structures can be observed. Terminologically, this classification defines two main types of mechanophysical structures: with distinct mechanophysical porosity (polyreticular non-gel porous type – Fig. 1) and without distinct mechanophysical porosity (gel type – Fig. 2). The figures show that, even at a magnification of 1470×, the chitosan/zeolite nanocomposite biofilm exhibits a mechanophysical porous structure (Fig. 1), whereas the second type, even at a magnification of ×10,000 displays a uniform, smooth, nonporous gel-type structure (Fig. 2).

From Fig. 1, a variation can be observed in the size of the elements forming the individual sections of the structure of the chitosan/zeolite nanocomposite biofilm. Fig. 3 shows an area located between the two types of surfaces. The surface morphology of the gel sample (Fig. 2) corresponds to the second type of structure (gel type). This structure is more uniform, without a distinct porous relief. For the chitosan/zeolite nanocomposite biofilm sample, the chemical composition was examined using an X-ray microanalyzer (XMA) on a cross-sectional cut of the sample. The results regarding the distribution of the elements Al, Si, and Fe are presented in Table 1 and in Figs. 3–5.

Analyses were performed using area scanning, from which the average composition of the sample was obtained, as well as point analyses for several zones. The results, with relatively good approximation, correspond to the presented area distribution.

Table 1. Chemical composition of Al, Si, and Fe in chitosan/zeolite nanocomposite biofilm

Element	Average composition, %	Zone 1, %	Zone 2, %
Al	97.18	85.02	83.59
Si	22.60	21.82	21.41
Fe	3.14	3.16	3.01

FTIR spectra of zeolite (Z) films and chitosan-zeolite nanocomposite (CSZ) films are shown in Figure 6. The spectrum of CS exhibits a broad peak at 3431.81 cm^{-1}, reflecting vibrational modes characteristic of NH and OH groups, at 2921 cm^{-1} (C–H symmetric stretching), at 1378.7 cm^{-1}, at 1654.9 cm^{-1} (amide II and C=O groups), at 1420 cm^{-1} (H–H vibrations), at 1152.6 cm^{-1} (C–O–C vibration), and at 1081.4 cm^{-1} (C–OH).

As shown in Figure 6(a), the FTIR spectrum of Z exhibits a peak at 1636.4 cm^{-1}, attributed to Si–O–Si bonding. Additionally, characteristic absorption peaks are observed at 1636 cm^{-1} (H–O–H), 794.5 cm^{-1} (Al–Al–OH bending vibration), and 467 cm^{-1} (Si–O). The spectrum of the CSZ nanocomposite film [Figure 6(b)] shows a characteristic band at 3431.8 cm^{-1}, which is due to hydrogen bonding formation between the functional groups of CS (O–H and N–H groups) and Z (O–H groups). The peak observed in the CS spectrum at 1654.9 cm^{-1} shifts to 1644.1 cm^{-1} in the CSZ spectrum [Figure 6(a)], corresponding to the deformation vibration of the amino groups of chitosan.

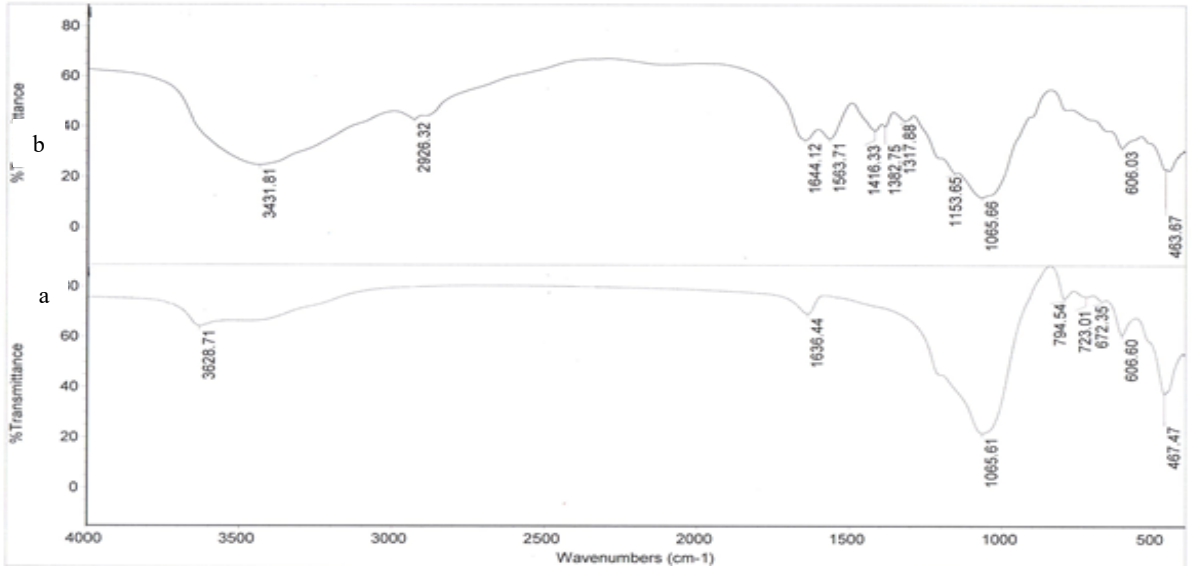

Fig. 6. FTIR spectra of zeolite (a) and chitosan-zeolite composite (b).

Porous structure of biomaterials may significantly vary depending on the used precursor and processing technology. Inasmuch as porous structure of a certain material determines its beneficial specific application, the proper porous texture evaluation and characterization is important. Porous characteristics of the bio-chars under consideration can be deduced from the N_2 adsorption isotherms presented on Figs. 7, 9, 11. Pore size distributions of zeolite, chitosan and chitosan-zeolite composite are shown in Figs. 8, 10, 12.

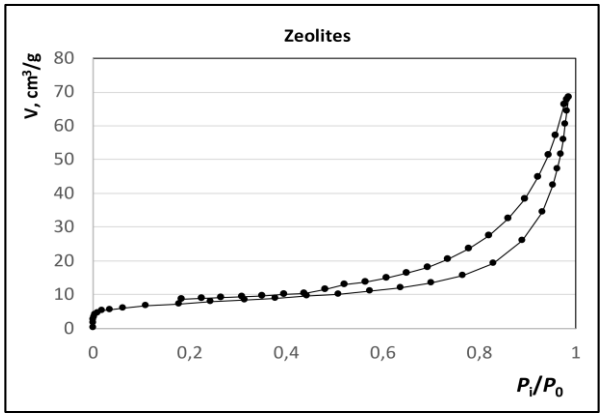

Fig. 7. N_2 adsorption isotherms of zeolite.

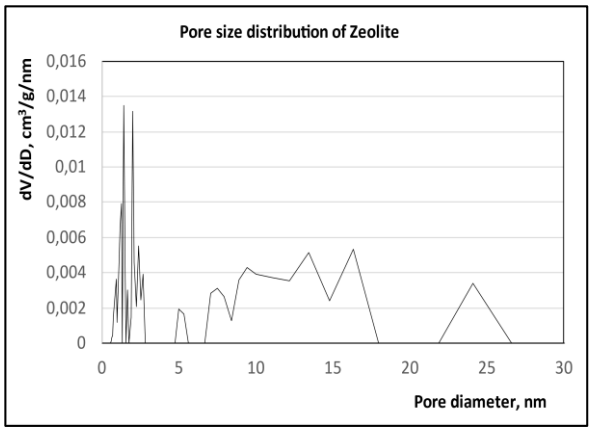

Fig. 8. Pore size distribution of zeolite.

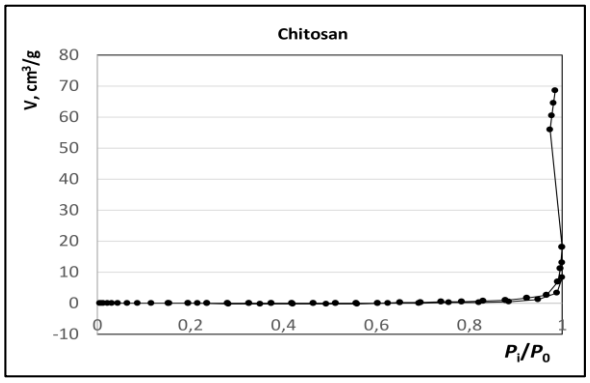

Fig 9. N_2 adsorption isotherms of chitosan.

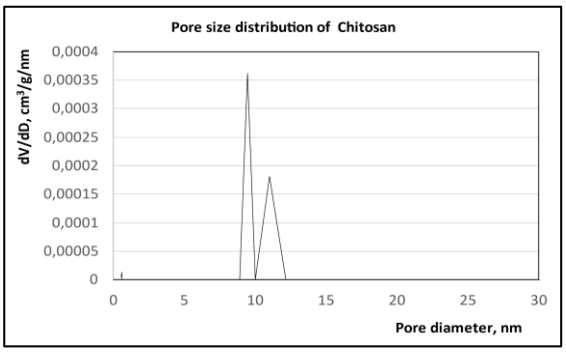

Fig. 10. Pore size distribution of chitosan.

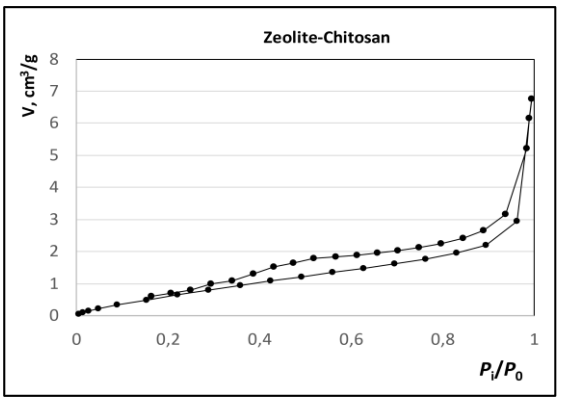

Fig 11. N_2 adsorption isotherms of zeolite - chitosan.

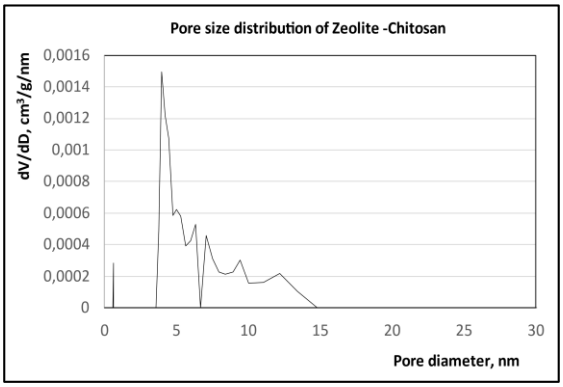

Fig. 12. Pore size distribution of zeolite - chitosan.

It should be mentioned that thermal destruction at proper experimental conditions of the samples leads to the production of materials that are highly dispersed with a well-developed system of pores and capillaries. Typically, the structure of a newly obtained pyrolytic product, i. e. char, retains the structure of the parental material as the formed pores are being oriented in a preferred direction corresponding to that of the precursor. This phenomenon is called *pseudomorphism*. It is the reason to observe the aforementioned peculiarities of the investigated chars.

Table 2. Textural analysis of chitosan, zeolite and chitosan–zeolite composite

Sample	CS	Z	CSZ
$V_{0.98}$ (cm^3 g^{-1})	0.0046	0.0964	0.0238
S_{BET} (m^2 g^{-1})	2	25	5
C	11.7	824.5	15.94
$V_{DR,\ micro}$ (cm^3 g^{-1})	0.0002	0.0103	0.0013
V_{meso}* (cm^3 g^{-1})	0.0044	0.0861	0.0225
$V_{DR,\ micro}$ (%)	4	11	5
V_{mezo} (%)	96	89	95
L_0 (nm)	9.44	1.41	2.82
	11.03	2.00	3.16
		1.26	4.73
		2.37	7.50
		13.41	9.44
		24.11	12.16

The textural analysis (Table 2) confirms that pristine zeolite possesses a highly developed porous structure, typical for clinoptilolite-rich materials. Its narrow micropores and broader mesopores contribute to its large surface area and make it suitable for sorption-based applications. In contrast, the pure chitosan sample demonstrated a significantly lower surface area and total pore volume, consistent with its polymeric, non-porous nature. Nonetheless, its pore volume was almost entirely mesoporous, suggesting a limited but accessible network, likely formed during membrane preparation and drying. The CSZ composite exhibits a moderate increase in both surface area and pore volume compared to pure chitosan. The presence of zeolite in the polymer matrix not only contributes to the formation of additional mesopores but also prevents structural collapse during drying. The resulting material benefits from the stabilizing effect of zeolite while retaining the flexibility of the biopolymer. The pore size distribution of CSZ reveals several mesopore populations, with dominant diameters in the range of 2.8–12.2 nm, confirming its hybrid nature.

The table presents the textural characteristics of the three samples — CS, Z, and CSZ. All materials exhibit relatively low values of specific surface area and total pore volume, indicating a limited development of the porous structure. Among them, sample Z shows the highest values of SBET (25 m^2/g) and V0.98 (0.0964 cm^3/g), suggesting a partially developed mesoporosity. Sample CS displays the lowest values of the porosity parameters, while the composite CSZ occupies an intermediate position, combining features of both precursor materials. The pore size distribution reveals that mesopores dominate in all samples, accounting for a substantial proportion (89–96%), whereas the fraction of micropores remains low. The average pore sizes (L_0) confirm this trend: sample Z exhibits smaller pores (1.4–3.7 nm), while CS and CSZ show larger pore dimensions in a wider range.

The conducted experiments clarify the nature and types of mechanophysical structures in the formation of pure chitosan and chitosan/zeolite composite biofilms, aiming to create a structure suitable for the incorporation of antibiotics on their surfaces. It was found that pure chitosan biofilms do not possess true physical porosity and belong to the so-called gel structural type, whereas chitosan/zeolite nanocomposite biofilms exhibit a textured morphology with developed physical porosity and, accordingly, a specific surface on which a relatively larger amount of drugs could potentially be implanted. Chemical composition analyses were performed using an X-ray microanalyzer (XMA), which revealed the presence of Al, Si, and Fe in the structure of the chitosan/zeolite nanocomposite biofilms. This feature enables the creation of a structure with genuine mechanophysical porosity and a well-developed specific surface, which is clearly advantageous for the implantation of antibiotics onto the internal surface of this type of drug carrier.

CONCLUSIONS

Because of their functional properties, chitosan/zeolite composites frequently exhibit remarkably improved mechanical strength; higher thermal stability, and relatively a good surface area [16-19]. Although the materials exhibit a limited development of surface area, they display varying degrees of porosity, with sample Z showing a relatively more pronounced porous structure. The composite sample CSZ combines the properties of CS and Z, which may provide a basis for balanced performance in applications that depend not so much on surface area as on chemical composition and the nature of active surface sites.

In addition to these characteristics, CSZ composites show the remarkable advantage of exhibiting biodegradability and biocompatibility associated with the biopolymer and thus can be an effective adsorbent due to its functional properties to remove pollutants.

Although the overall surface area of the composite does not reach that of the zeolite, the observed enhancement compared to chitosan alone demonstrates the synergistic interaction between the

two components. This structural modification may be advantageous in applications where moderate porosity, biocompatibility and mechanical reinforcement are required.

REFERENCES

1. V. E. Santo, M. E. Gomes, J. F. Mano, R. L. Reis, *J. Tissue Eng. Regen. Med*., **6**, (S3), s47 (2012) DOI: https://doi.org/10.1002/term.1519.
2. E. Vunain, A. Mishra, B. Mamba, *Int. J. Biol. Macromol.*, **86**, 570 (2016) DOI: https://doi.org/10.1016/j.ijbiomac.2016.02.005.
3. T. Anirudhan, S. Rijith, *J. Environ. Radioact*., **106**, 8 (2012) DOI: https://doi.org/10.1016/j.jenvrad.2011.10.013.
4. P. Grzybek, Ł. Jakubski, G. Dudek, *International Journal of Molecular Sciences,* **23**, 17 (2022) DOI: https://doi.org/10.3390/ijms23179932.
5. S. Kumar, R. Bera, N. Das, J. Koh, *Carbohydrate Polymers*, 232 (2020) DOI: https://doi.org/10.1016/j.carbpol.2019.115808.
6. M. Batista, M. L. Pinto, F. Antunes, J. Pires, S. Carvalho, *Materials*, **14,** 21, 6701 (2021) DOI: https://doi.org/10.3390/ma14216701.
7. L. Qiao, L. Zhao, C. Liang, K. Du, *J. Mater. Chem. B*, **7**, 5510 (2019).
8. T. M. Budnyak, I. V. Pylypchuk, V. A. Tertykh, E. S. Yanovska, D. Kolodynska Budnyak, *Nanoscale Research Letters*, **10** (87), 1 (2015) DOI: 10.1186/s11671-014-0722-1, 2014, DOI:10.1186/s11671-014-0722-1.
9. C. Bothiraja, U. Thorat, A. Pawar, K. Shaikh, *Mater. Technol*., **29**, (sup3), part B2, B120 (2014) DOI: https://doi.org/10.1179/1753555714Y.0000000174.
10. C. Viseras, C. Aguzzi, P. Cerezo, M. Bedmar, *Mater. Sci. Technol.*, **24** (9), 1020 (2008) DOI: https://doi.org/10.1179/174328408X341708.
11. F. Chivrac, E. Pollet, M. Schmutz, L. Avérous, *Carbohydr. Polym*., **80** (1), 145 (2010) DOI: https://doi.org/10.1016/j.carbpol.2009.11.004.
12. L. Alves, E. Ferraz, J. Gamelas, *Adv. Colloid Interf. Sci*., **272**, 101994 (2019), DOI: https://doi.org/10.1016/j.cis.2019.101994.
13. M. R. Abukhadra, A. Adlii, B. M. Bakry, *Int. J. Biol. Macromol*., **126**, 402 (2019) DOI: https://doi.org/10.1016/j.ijbiomac.2018.12.225
14. S. S. Ray, M. Okamoto, *Prog. Polym. Sci*., **28** (11), 1539 (2003), DOI: https://doi.org/
15. M. L. P. Dalida, A. F. V. Mariano, C. M. Futalan, C.-C. Kan, W.-C. Tsai, M.-W. Wan, *Desalination*, **275** (1–3), 154 (2011) DOI: https://doi.org/10.1016/j.desal.2011.02.051.
16. W.-C. Tsai, S. Ibarra-Buscano, C.-C. Kan, C.M. Futalan, M. L. P. Dalida, M.-W. Wan, *Desalin. Water Treat.*, **57** (21), 9799 (2016) DOI: https://doi.org/10.1080/19443994.2015.1035676.
17. W. S. Wan Ngah, N. F. M. Ariff, A. Hashim, M. A. K. M. Hanafiah, *Clean–Soil, Air, Water*, **38** (4), 394 (2010) DOI: https://doi.org/10.1002/clen.200900251.
18. K.-H. Liu, T.-Y. Liu, S.-Y. Chen, D.-M. Liu, *Acta Biomater*., **4**, 1038 (2008) DOI: https://doi.org/10.1016/j.actbio.2008.01.012.
19. S. Hua, H. Yang, W. Wang, A. Wang, *Appl. Clay Sci*., **50** (1), 112 (2010) DOI: https://doi.org/10.1016/j.clay.2010.07.012.

BULGARIAN CHEMICAL COMMUNICATIONS

Instructions about Preparation of Manuscripts

General remarks: Manuscripts are submitted in English by e-mail or by mail (in duplicate). The text must be typed double-spaced, on A4 format paper using Times New Roman font size 12, normal character spacing. The manuscript should not exceed 15 pages (about 3500 words), including photographs, tables, drawings, formulae, etc. Authors are requested to use margins of 3 cm on all sides. For mail submission hard copies, made by a clearly legible duplication process, are requested. Manuscripts should be subdivided into labelled sections, e.g. **Introduction, Experimental, Results and Discussion**, *etc*.

The title page comprises headline, author's names and affiliations, abstract and key words.

Attention is drawn to the following:

a) **The title** of the manuscript should reflect concisely the purpose and findings of the work. Abbreviations, symbols, chemical formulas, refer-ences and footnotes should be avoided. If indis-pensable, abbreviations and formulas should be given in parentheses immediately after the respective full form.

b) **The author**'s first and middle name initials, and family name in full should be given, followed by the address (or addresses) of the contributing laboratory (laboratories). **The affiliation** of the author(s) should be listed in detail (no abbreviations!). The author to whom correspondence and/or inquiries should be sent should be indicated by asterisk (*).

The abstract should be self-explanatory and intelligible without any references to the text and containing not more than 250 words. It should be followed by key words (not more than six).

References should be numbered sequentially in the order, in which they are cited in the text. The numbers in the text should be enclosed in brackets [2], [5, 6], [9–12], etc., set on the text line. Refer-ences, typed with double spacing, are to be listed in numerical order on a separate sheet. All references are to be given in Latin letters. The names of the authors are given without inversion. Titles of journals must be abbreviated according to Chemical Abstracts and given in italics, the volume is typed in bold, the initial page is given and the year in parentheses. Attention is drawn to the following conventions:

a) The names of all authors of a certain publications should be given. The use of "*et al*." in the list of references is not acceptable.

b) Only the initials of the first and middle names should be given.

In the manuscripts, the reference to author(s) of cited works should be made without giving initials, e.g. "Bush and Smith [7] pioneered...". If the refer-ence carries the names of three or more authors it should be quoted as "Bush *et al*. [7]", if Bush is the first author, or as "Bush and co-workers [7]", if Bush is the senior author.

Footnotes should be reduced to a minimum. Each footnote should be typed double-spaced at the bottom of the page, on which its subject is first mentioned.

Tables are numbered with Arabic numerals on the left-hand top. Each table should be referred to in the text. Column headings should be as short as possible but they must define units unambiguously. The units are to be separated from the preceding symbols by a comma or brackets.

Note: The following format should be used when figures, equations, *etc*. are referred to the text (followed by the respective numbers): Fig., Eqns., Table, Scheme.

Schemes and figures. Each manuscript (hard copy) should contain or be accompanied by the respective illustrative material as well as by the respective figure captions in a separate file (sheet). As far as presentation of units is concerned, SI units are to be used. However, some non-SI units are also acceptable, such as °C, ml, l, etc.

The author(s) name(s), the title of the manuscript, the number of drawings, photographs, diagrams, etc., should be written in black pencil on the back of the illustrative material (hard copies) in accordance with the list enclosed. Avoid using more than 6 (12 for reviews, respectively) figures in the manuscript. Since most of the illustrative materials are to be presented as 8-cm wide pictures, attention should be paid that all axis titles, numerals, legend(s) and texts are legible.

The authors are asked to submit **the final text** (after the manuscript has been accepted for publication) in electronic form either by e-mail or mail on a 3.5'' diskette (CD) using a PC Word-processor. The main text, list of references, tables and figure captions should be saved in separate files (as *.rtf or *.doc) with clearly identifiable file names. It is essential that the name and version of the word-processing program and the format of the text files is clearly indicated. It is recommended that the pictures are presented in *.tif, *.jpg, *.cdr or *.bmp format, the equations are written using "Equation Editor" and chemical reaction schemes are written using ISIS Draw or ChemDraw programme.

The authors are required to submit the final text with a list of three individuals and their e-mail addresses that can be considered by the Editors as potential reviewers. Please, note that the reviewers should be outside the authors' own institution or organization. The Editorial Board of the journal is not obliged to accept these proposals.

EXAMPLES FOR PRESENTATION OF REFERENCES

REFERENCES

1. D. S. Newsome, *Catal. Rev.–Sci. Eng*., **21**, 275 (1980).
2. C.-H. Lin, C.-Y. Hsu, *J. Chem. Soc. Chem. Commun*., 1479 (1992).
3. R. G. Parr, W. Yang, Density Functional Theory of Atoms and Molecules, Oxford Univ. Press, New York, 1989.
4. V. Ponec, G. C. Bond, Catalysis by Metals and Alloys (Stud. Surf. Sci. Catal., vol. 95), Elsevier, Amsterdam, 1995.
5. G. Kadinov, S. Todorova, A. Palazov, in: New Frontiers in Catalysis (Proc. 10th Int. Congr. Catal., Budapest, 1992), L. Guczi, F. Solymosi, P. Tetenyi (eds.), Akademiai Kiado, Budapest, 1993, Part C, p. 2817.
6. G. L. C. Maire, F. Garin, in: Catalysis. Science and Technology, J. R. Anderson, M. Boudart (eds), vol. 6, Springer-Verlag, Berlin, 1984, p. 161.
7. D. Pocknell, *GB Patent* 2 207 355 (1949).
8. G. Angelov, PhD Thesis, UCTM, Sofia, 2001.
9. JCPDS International Center for Diffraction Data, Power Diffraction File, Swarthmore, PA, 1991.
10. CA **127**, 184 762q (1998).
11. P. Hou, H. Wise, *J. Catal.*, in press.
12. M. Sinev, private communication.
13. http://www.chemweb.com/alchem/articles/1051611477211.html.

Texts with references which do not match these requirements will not be considered for publication!!!

International Conference "Science-Industry-Society Nexus for Sustainable Regions", organized by the Burgas State University "Prof. Dr. Assen Zlatarov"and the Thracian University-Odrin, Turkey, June 12 - 14, 2025, Burgas, Bulgaria

CONTENTS